



universität
wien

MASTERARBEIT

Titel der Masterarbeit

THE CHEMO-DYNAMICAL EVOLUTION OF DWARF-GALAXY DISCS

Verfasser

Matthias Kühtreiber, Bakk. rer. nat.

angestrebter akademischer Grad

Master of Science (MSc)

Wien, 2015

Studienkennzahl lt. Studienblatt: A 066 861

Studienrichtung lt. Studienblatt: Astronomie

Betreuer: Univ.-Prof. Dipl.-Phys. Dr. Gerhard Hensler

Contents

1	Introduction	7
1.1	Dwarf Galaxies	7
1.1.1	Definitions	7
1.1.2	Transition Processes	8
1.1.3	Why are Dwarf Galaxies Interesting?	8
1.2	Galaxy Simulations	9
1.2.1	Eulerian Grid vs. Smoothed Particle Hydrodynamics	9
1.2.2	Dwarf Galaxy Simulations - Present Status	10
1.2.3	Single-Phase Gas Description	12
1.2.4	Multi-Phase Gas Description	13
1.2.5	Outline	13
2	Smoothed Particle Hydrodynamics	15
2.1	Theory	16
2.2	Hydrodynamics	19
3	Gadget-2	23
3.1	Collisionless Dynamics and Gravity	23
3.2	Tree Algorithm	24
3.3	Neighbour Search	26
3.4	The Tree Particle Mesh Method	26
3.5	Hydrodynamics	27
3.6	Time Integration	28
4	Extentions of Gadget-2	31
4.1	Cooling	31
4.1.1	Theory	31
4.1.2	Implementation	32
4.2	Star Formation	35

4.2.1	Theory	35
4.2.2	Stochastic Star-Formation Recipe	36
4.2.3	Star Formation based on Köppen, Theis, Hensler (1995)	38
4.2.4	Implementation	39
4.3	Feedback Processes	41
4.3.1	Stellar Wind and UV-Radiation	41
4.3.2	Type II Supernovae	42
4.3.3	Planetary Nebulae	42
4.3.4	Type Ia Supernovae	43
4.3.5	Implementation	43
5	Code Tests	47
5.1	Cooling Test	47
5.2	Feedback Test	49
6	Simulations	55
6.1	Initial Conditions	55
6.2	Accuracy Parameters	57
7	Results: Reference Simulations	61
7.1	Mass Evolution	61
7.2	Density and Temperature Distribution	63
7.3	Total Energy and Angular Momentum	68
7.4	Galaxy Shape	68
7.5	Star-Formation Rates	75
7.6	Chemical Evolution	84
8	Effects of the Cooling Shut-Off Time τ_{CSO}	89
8.1	Star Formation	89
8.2	Chemical Evolution	91
9	Effects of the Gravitational Softening ϵ	95
9.1	Star Formation	95
9.2	Chemical Evolution	98
10	Effects of the Supernova Energy E_{SN}	103
10.1	Star Formation	103
10.2	Chemical Evolution	104

11 Comparisons With the Multi-Phase Model	109
11.1 The Multiphase Description	109
11.2 Initial Set Up	110
11.3 Star Formation	111
11.4 Chemical Evolution	114
12 Brief Summary	119
Acknowledgements	123
Abstract English	124
Abstract Deutsch	127
Bibliography	129
List of Figures	140
List of Tables	141
Curriculum Vitæ	142

Chapter 1

Introduction

1.1 Dwarf Galaxies

1.1.1 Definitions

There are many different possibilities to define dwarf galaxies. Earlier definitions mostly focus on the size and the surface brightness (Hodge, 1971). A widely accepted definition was given by G. Tammann, namely all galaxies fainter than $M_B \geq -16$ mag or $M_V \geq -17$ mag and more spatially extended than globular clusters are dwarf galaxies (Tammann, 1994). Most of the galaxies in the local universe and nearby clusters can be classified as a member of this group of galaxies and they can be divided into different morphological types. The largest fraction are early-type dwarf galaxies, which consist of dwarf spheroidals (dSph) and dwarf ellipticals (dEs). They contain only marginally amounts of gas and usually show very little star formation. dSphs are faint ($M_V \gtrsim -14$ mag) and their total mass lies in the range of $M_{tot} \sim 10^7 M_\odot$, with negligible gas content and they can be found mostly near massive galaxies (Grebel, 2001). dEs are fainter than $M_V \geq -17$ mag and have total masses of $M_{tot} \sim 10^9 M_\odot$ with $M_{HI} \sim 10^8 M_\odot$. They often have relatively bright cores and are elliptical or spherical in shape.

Late-type dwarf galaxies are Dwarf irregulars (dIrrs), which typically have high gas contents of approximately $M_{HI} \sim 10^9 M_\odot$ and total masses of $M_{tot} \sim 10^{10} M_\odot$. Their appearance is often scattered but there are also galaxies showing smooth discs or spiral features, with similar brightness and mass, like dIrrs and small diameters, usually with $r < 5$ kpc. This type was discovered by J. M. Schombert and is referred to as dwarf spirals (dSs) (Schombert et al., 1995).

1.1.2 Transition Processes

It is assumed that, due to different physical processes, galaxies can change their morphology. In galaxy clusters, early-type galaxies are more frequently observed near the cluster center, whereas the outer regions show a larger number of late-type galaxies. One can therefore assume, that the infall of a galaxy into the cluster can lead to an evolutionary transition process, possibly caused by ram pressure stripping, where a galaxy can lose large fractions of its gas content (Gunn and Gott, 1972). Other processes would be "galaxy harassment", where smaller disc galaxies experience frequent fly-bys with high velocities, transforming them to dEs (Moore et al., 1996) and "tidal stirring", where gas gets removed from a satellite galaxy near a massive galaxy due to the strong tidal field (Mayer et al., 2001; Hensler, 2011).

1.1.3 Why are Dwarf Galaxies Interesting?

Dwarf galaxies offer a great opportunity to study internal processes in such systems, because they have lower mass and therefore flat potential wells, compared to massive spiral galaxies. This leads to more sensitive reactions of the galaxy on variations in the density and temperature distributions, the star formation rate (SFR), internal kinematics and so on. Therefore, astrophysicists can learn much more about these, somewhat inconspicuous objects. Another very interesting aspect about dwarf galaxies is, that they are assumed to be the building blocks of larger, more massive galaxies, according to the standard Λ CDM model. Because of these circumstances, dwarf galaxies are the ideal objects to test our understanding of the different physical processes interacting on galactic scales and numerical simulations play a crucial role and offer us the possibility to carry out different experimental set ups, which can be compared to each other and to observations. Observations of the cosmic microwave background (CMB) have revealed extremely low anisotropies, whereas the present day universe shows strong inhomogeneities, at least on scales of galaxy clusters. This means, that the density distribution in the universe must have experienced evolutionary processes. After the inflation phase, the density fluctuations cause dark matter to clump together, forming virialized haloes, which are the foundation for later galaxies. Baryonic matter can fall into these potential wells and accumulate. An over-dense region will expand slower compared to the overall universe, because of self gravity. The growth of such density fluctuations will steadily produce even bigger structures. This "hierarchical clustering" is believed to be the main driving force of forming galaxies and clusters. In this framework, dwarf galaxies play a very important

role, not only because of their high numbers, but also because of this cosmological relevance, in which dwarf galaxies are viewed as the building blocks for bigger systems.

1.2 Galaxy Simulations

A galaxy is a tremendously complex system of interacting gas, stars and dark matter. In principle, a lot of simplifications have to be made in order to perform numerical simulations of galaxies, because of limited calculation power, but the overall properties of galactic systems should be reproduced. There are many different ways to approach this issue, the most common is to use a numerical grid to treat gas via the Euler equations, but there are also alternatives like for instance smoothed particle hydrodynamics (SPH).

1.2.1 Eulerian Grid vs. Smoothed Particle Hydrodynamics

There are many different types of grid methods, like for instance lagrangian grids, where the cells follow the paths of fluid elements. The motion of these nodes relative to each other can result in compression or expansion of the mesh, but the mass within the cells remains constant. No mass would be exchanged in this case, which has the advantage, that like in SPH, no adaptive mesh refinement is necessary. The most common grid method, however is to use an Eulerian grid, where the mesh is fixed in space. The simulated fluid moves within the grid and the flux of mass, energy and momentum are simulated in order to describe the physical properties of the fluid. This method has proven to be very successful for simulations of galaxies, but besides a lot of advantages, an Eulerian grid also carries some inherent problems. The most important are:

1. It is problematic to investigate how field variables evolve over time at a fixed point in the fluid, because the movement of the material cannot be tracked easily with a stationary grid. One can only have the time evolution of field variables at fixed points in space.
2. Irregular and complicated geometries of the fluid can be problematic, because special techniques for increasing the numerical resolution in certain areas are necessary, like for instance adaptive mesh refinement (AMR), which are usually very expensive.
3. The grid must cover the whole domain of the simulation volume, where the simulated fluid could possibly flow (Liu and Liu, 2003).

The SPH method is more and more used in computational physics, especially for astrophysical simulations with great success in reproducing observations (Lucy, 1977; Katz, 1992; Springel, 2005; Stinson et al., 2006; Springel, 2010, 2014; Liu et al., 2015). Because of some advantages, we used SPH for our studies of dwarf galaxies in this thesis. The SPH method will be introduced and discussed in the following chapter.

1.2.2 Dwarf Galaxy Simulations - Present Status

One of the first studies of simulations of dwarf galaxies is carried out by Dekel and Silk (1986). These authors already realize the importance of Supernovae (SN) feedback and resulting galactic winds on the behaviour of a dwarf galaxy model. Semi-analytical models are used by Yoshii and Arimoto (1987) to investigate the properties of dwarf galaxies and globular clusters, where special emphasis is put on the modelling of SN-driven winds. The dynamical response of the latter is also taken into account in their models and they are able to reproduce observations of the structure and metallicity of elliptical galaxies, dEs and globular clusters. The results of Yoshii and Arimoto (1987) suggest, that the spheroidal systems are a one-parameter family of their initial mass. This work is further developed in Nagashima and Yoshii (2004), where a Monte Carlo technique is used for the merger tree leading to the formation of dwarf galaxies. Also different star-formation recipes are tested in their studies. This model is later combined with N-body simulations in Nagashima et al. (2005), where merging histories of dark halos are taken directly from particle simulations, instead of using a Monte Carlo approach. Cooling, feedback, star formation, population synthesis, and extinction by dust and HI clouds are all taken into account, successfully reproducing many observations. Burkert and Ruiz-Lapuente (1997) also use semi analytical models to test the effects of feedback from type Ia SNe on dwarf galaxy simulations. They find that, based on the adopted feedback scheme, for dSphs with a gas mass below $10^8 M_{\odot}$ the type Ia SNe originated from the first generation of stars can quench star formation and delay a second epoch of SF by many Gyr. In Mac Low and Ferrara (1999) analytical and numerical studies of the effects of repeated SN explosions in dwarf galaxies on the interstellar medium are carried out. This is done for different galaxy masses and different SN rates and it is found that systems with gas masses $\leq 10^6 M_{\odot}$ are not able to blow away their interstellar gas. Ferrara and Tolstoy (2000), use detailed semi-analytical models of dwarf irregular galaxies to investigate the effects of stellar feedback and dark matter. Their results suggest that dwarfs with too small total masses can easily

be blown away if $M_{tot} \lesssim 5 \times 10^6 M_{\odot}$ and mass loss due to outflows is found for galaxies up to $\sim 10^9 M_{\odot}$. They also discuss that the metallicity is strongly correlated with the dark matter content and for dIrrs a minimum oxygen abundance of $12+\log(\text{O}/\text{H}) \sim 7.2$ is reported. This value is in good agreement with the oxygen content of IZw18, the most metal-poor galaxy known. N-body and SPH simulations are used by Chiosi and Carraro (2002) to investigate the formation and evolution of elliptical galaxies, but also including dSphs and dEs in order to interpret the fundamental plane and other relations. They use homogeneous gas clouds embedded in dark matter halos as initial conditions, where star formation starts after a merging period. One-dimensional chemo-dynamical models of dEs are carried out by Hensler et al. (2004), where it is interestingly found that radial oscillations, caused by heating and cooling of the ISM in such systems have a strong influence on their evolution and can reinforce the effects of starbursts. Simulations of dSphs are also carried out by Stinson et al. (2007), where similar initial conditions were used like in Chiosi and Carraro (2002) and their N-body and SPH-code is based on Stinson et al. (2006). In this case however, additional rotation is added to the gas component. A burst-like behaviour of the system is reported, similar to what is found by Chiosi and Carraro (2002). In Recchi et al. (2007), chemo-dynamical simulations of dSph-sized dwarf galaxies without dark matter are compared with simulations containing dark matter. Unexpectedly, the models without deep potential wells can survive in most cases and they show consistent results compared to models with high dark matter content. Other simulations are carried out considering interstellar clouds in gas-rich dwarf galaxies by Recchi and Hensler (2007). It is found that they only survive a few tens of Myr, but can help to delay large scale outflows from the galaxies by mass loading in some cases. Another very interesting study of isolated dwarf galaxies is carried out by Valcke et al. (2008), where N-body and SPH simulations are used with the initial conditions of homogeneous gas clouds collapsing in dark matter potentials. For their dwarf galaxy models, the star formation rates also show burst-like behaviour and, at least for their low mass models, strong gas outflows. In Mashchenko et al. (2008), cosmological simulations are performed including dwarf galaxies, where special emphasis is put on gravitational heating of dark matter, caused by gas flows. It is pointed out that simulations often predict a divergent dark matter density distribution in the center, but from observations, a relatively constant distribution is expected, which is often referred to as the famous "cusp-core" problem. The authors suggest that this heating process can transform a cusped dark matter halo in one with a central core and also strong gas outflows are reported, which are in agreement with observations of dwarf galax-

ies with comparable physical properties. Detailed studies on galactic winds and their effect on the chemo-dynamical evolution of dwarf galaxies are carried out by Recchi et al. (2009), which are also enhanced and discussed in following publications reviewed below. Sawala et al. (2010) use cosmological initial conditions, to simulate the formation of dwarf galaxies and are able to produce objects with similar properties like dSph in the local group. In Schroyen et al. (2011), a large set of simulations of isolated dwarf galaxies, with rotating and non-rotating initial conditions are carried out in order to investigate why rotating dIrrs and dEs show flat vertical metallicity profiles, and round, non-rotating dEs exhibit negative gradients. Besides the famous "fountain mechanism", they discuss a possible alternative "centrifugal barrier mechanism" and conclude that rotation is one of the most fundamental parameters in galaxy evolution. In a more recently study, Recchi and Hensler (2013) use chemo-dynamical simulations of dwarf galaxy systems with different gas distributions, masses, and gas fractions in order to discuss mass and metal loss due to galactic winds. They found out that the gas distribution can make big differences up to an order of magnitude for the fraction of lost metals. Schroyen et al. (2013) investigate the survivability of metallicity gradients in isolated dwarf galaxies and they also compare the effects of a low and a high density star formation threshold value of 0.1 and 100 cm^{-3} respectively. Their results suggest that the gradients are very robust, as long as there are no external influences and can very well reproduce observational measurements. An outstanding review of chemo-dynamical simulations of dwarf galaxies is published by Recchi (2014), who also investigates the formation of galactic winds and their effects on galactic systems. An important study for this master thesis is Liu et al. (2015) and the PhD thesis of Lei Liu (Liu, 2013), who investigates the chemo-dynamical evolution of isolated dwarf galaxies with the novel GPU-accelerated N-body/SPH code "cd-SPH". They use the sticky particle multi-phase gas description by Theis and Hensler (1993) and can reproduce the typical decoupled abundance ratios for the hot/warm and the cold, as well as the stellar component. A relatively extensive summary of dwarf-galaxy evolution can be found in Papaderos et al. (2012), which is still the latest published book on this topic.

1.2.3 Single-Phase Gas Description

There are different ways of treating gas in such SPH simulations. In the single-phase approach, gas particles cool below 10^4 K, leading to collapses until star-formation criteria are fulfilled enabling star-formation in these over-density regions. The stellar particles inject energy, mass and heavy elements back into

the ISM, which self regulates further star formation. In some cases the feedback energy is not only used to increase the internal energy of gas particles, but also convert a part of it directly into kinetic energy (Springel and Hernquist, 2003). In most cases, gas cools too quickly, because of the high temperatures and gas densities near type II SNe, leading to the often discussed over cooling problem (Gerritsen and Icke, 1997; Kawata and Hanami, 1998; Springel et al., 2001; Stinson et al., 2006). To reduce this effect, cooling is turned off for a specific amount of time, for those gas particles, because otherwise a large fraction of internal energy would be radiated away within a typical timestep.

1.2.4 Multi-Phase Gas Description

On the other hand, great efforts have been made to find ways of treating the gas component as a multi-phase, overcoming the problems mentioned above (Semelin and Combes, 2002), where for instance gas particles carry a specific fraction of cold clouds (Springel and Hernquist, 2003; Murante et al., 2010; Scannapieco et al., 2006). Another possibility is to use cold cloud particles, which are treated like N-body particles and therefore the cold and hot/warm components are decoupled from each other (Theis et al., 1992; Theis and Hensler, 1993; Hensler and Rieschick, 2002; Hensler et al., 2004). Considering this "sticky" particle method, which is described in more detail in section 11.1, the cold clouds do not undergo a full hydrodynamical calculation, but are treated as N-body particles. These particles can coagulate, when they collide and fragment when they form stars. Further, they can evaporate to the hot/warm component and can exchange energy and momentum with the hot/warm phase due to drag forces. Also feedback is treated separately, the effect from SNe only influences the hot/warm component and the effect from stellar wind and planetary nebulae the cold clouds.

1.2.5 Outline

This Thesis is structured as follows: In chapter 2, a short introduction to the basic ideas and formalism of the SPH method is presented. Chapter 3 is an overview of the publicly available version of *Gadget-2*, which was used for further modifications and extensions, described in chapter 4. The implemented functions for cooling and feedback are tested in chapter 5, specifications of the simulated dwarf galaxy are demonstrated in chapter 6. The following four chapters present results of the simulation runs, for different simulation parameters including a comparisons with the multi-phase code used in Liu (2013); Liu et al. (2015). In chapter 12, the results are summarized and discussed.

Chapter 2

Smoothed Particle Hydrodynamics

Hydrodynamical problems which are commonly encountered in a large variety of theoretical astrophysical considerations, are normally in the form of partial differential equations (PDE) of field variables. In most cases, analytical solutions of such sets of PDEs are impossible. Therefore numerical methods are essential in order to find solutions. An alternative to the classical Eulerian grid-based approach is Smoothed Particle Hydrodynamics (SPH), which was first introduced by Gingold and Monaghan (1977).

The basic idea of SPH is to discretize the problem domain into a number of SPH-particles. Using the particle approximation method, the physical properties of a particle are depending also on the properties of the neighbouring particles, which are smoothed by a so-called kernel function. This is achieved by approximating the integral representation by summations over the needed values of the neighbouring particles, which is done in a specific area, the so-called "support domain", around a particle in question, represented by the smoothing length h . Compared to grid-based numerical methods, SPH shows some advantages, like e.g. the inherent resolution adaptivity in regions of higher density, where more SPH-particles are located. This is very convenient because in this case, there is no need for adaptive mesh refinement algorithms. It shows to be especially useful in astrophysical applications, because often a huge variety of densities is encountered (Springel, 2010). Another advantage is, that SPH-particles are not only interpolation points, but they also carry physical properties of the fluid, and are therefore used as fluid elements at the same time. In the following section, the theoretical formalism, based on the Lagrangian method of this interesting and

still somewhat novel method, will be briefly derived.

2.1 Theory

The basis of the integral representation of a function $f(\vec{r})$ is the following identity.

$$f(\vec{r}) = \int_{\Omega} f(\vec{r}') \delta(\vec{r} - \vec{r}') d\vec{r}' \quad (2.1)$$

where \vec{r} is the position vector and Ω the volume which contains \vec{r} . $\delta(\vec{r} - \vec{r}')$ is the Dirac delta function, which is defined as

$$\delta(\vec{r} - \vec{r}') = \begin{cases} 1 & \vec{r} = \vec{r}' \\ 0 & \vec{r} \neq \vec{r}' \end{cases} \quad (2.2)$$

$\delta(\vec{r} - \vec{r}')$ can be replaced by a kernel function $W(\vec{r} - \vec{r}', h)$. This is often referred to as the “kernel approximation”.

$$f(\vec{r}) = \int_{\Omega} f(\vec{r}') W(\vec{r} - \vec{r}', h) d\vec{r}' \quad (2.3)$$

The kernel function must satisfy three conditions. The first one is the “normalisation condition” 2.4, which means that the integral of the kernel function produces unity, just like the Dirac delta function.

$$\int_{\Omega} W(\vec{r} - \vec{r}', h) d\vec{r}' = 1 \quad (2.4)$$

There is another parallel between $\delta(\vec{r} - \vec{r}')$ and $W(\vec{r} - \vec{r}', h)$, namely the fact that for the smoothing length h approaching 0, the kernel function is identical to the Dirac delta function. This is the second condition a smoothing function must fulfil (“Delta function property”).

$$\lim_{h \rightarrow 0} W(\vec{r} - \vec{r}', h) = \delta(\vec{r} - \vec{r}') \quad (2.5)$$

The third one is the so-called "compact condition" (eq. 2.6), which makes sure that the kernel function is 0 outside of the support domain. The support domain is the spherical region formed by the smoothing length around an SPH-particle. In most literature, the kernel function is defined that it reaches 0 at a radius of $2h$, but since Gadget-2 is used for this thesis, the author wishes to use the same definition for the support domain like Volker Springel, therefore the used kernel function is 0 for $\vec{r} > h$ (see equation 2.7).

$$W(\vec{r} - \vec{r}', h) = 0 \text{ if } |\vec{r} - \vec{r}'| > h \quad (2.6)$$

It is very practical to use such a kernel function with a finite support domain, because otherwise every particle would have to interact with all other particles in the whole simulation, resulting in unnecessarily high computational effort, considering that for high distances the contribution from other particles would decline very rapidly. In early SPH literature sometimes a Gaussian function was used, today the cubic spline function (eq. 2.7) is the standard choice. It is illustrated in figure 2.1.

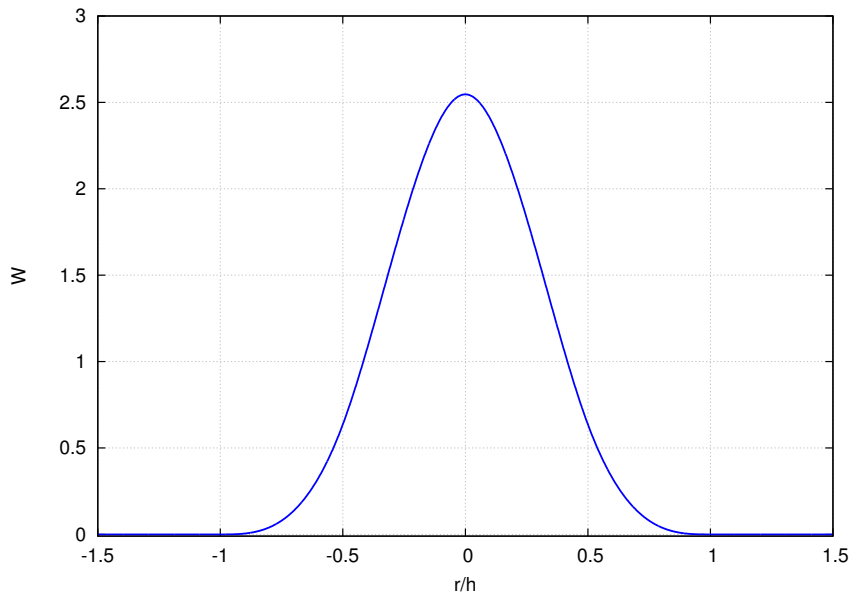


Figure 2.1: Cubic Spline function.

$$W(r_{ij}, h) = \frac{8}{\pi h^3} \begin{cases} 1 - 6\left(\frac{r}{h}\right)^2 + 6\left(\frac{r}{h}\right)^3 & 0 \leq \frac{r}{h} \leq \frac{1}{2} \\ 2\left(1 - \frac{r}{h}\right)^3 & \frac{1}{2} \leq \frac{r}{h} \leq 1 \\ 0 & \frac{r}{h} > 1 \end{cases} \quad (2.7)$$

In the previous equation, r_{ij} was used as a simplified notation for $r_i - r_j$, and $r = |r_{ij}|$. Let us now consider a distribution of N particles, with positions \vec{r}_i , mass m_i and density ρ_i . Assuming a field F , known at these points, one gets from eq. 2.1 the smoothed interpolated version of this field by approximating the integral to a sum.

$$F_s(\vec{r}) = \int F(\vec{r}') W(\vec{r} - \vec{r}', h) d\vec{r}' \quad \rightarrow$$

$$F_s(\vec{r}) \simeq \sum_j \frac{m_j}{\rho_j} F(\vec{r}_j) W(\vec{r} - \vec{r}_j, h) \quad (2.8)$$

In this case, $d\vec{r}'$ is approximated as the finite volume element $\frac{m_j}{\rho_j}$. If we insert the density for field $F_s(\vec{r})$, we can see that ρ can be eliminated and therefore only depends on the positions and masses of the particles.

$$\rho_i = \sum_j \frac{m_j}{\rho_j} \rho_j W(r_{ij}, h) = \sum_j m_j W(r_{ij}, h) \quad (2.9)$$

This last equation (2.9) is very important, because it describes exactly how the density is estimated in an SPH simulation. This is in most cases one of the first calculation steps. The density can now be used together with eq. 2.8 to calculate other physical properties $F_s(\vec{r})$, not only at the positions of the particles, but also in every point between them, if needed.

We also need to define the value of the smoothing length h . As already mentioned, the adaptability of h is one of the advantages of SPH, therefore $h = h(\vec{r}, t)$ will continuously change. The number of neighbouring particles N_{ngb} which are located inside the smoothing region is kept constant (or approximately constant) by changing h . N_{ngb} is therefore an important parameter in SPH simulations and should be larger than 32 for three-dimensional simulations (Springel, 2010). It

turns out to be a good choice, to have the mass in the kernel volume fixed to a constant value, especially if particles have a large variety in their masses. This method is for instance adopted in Gadget-2, but it is possible for the user to determine a specific number of neighbouring particles and how much it is allowed to vary, in order to be as close to condition eq. (2.10) as possible.

$$\rho_i h_i^3 = \text{const.} \quad (2.10)$$

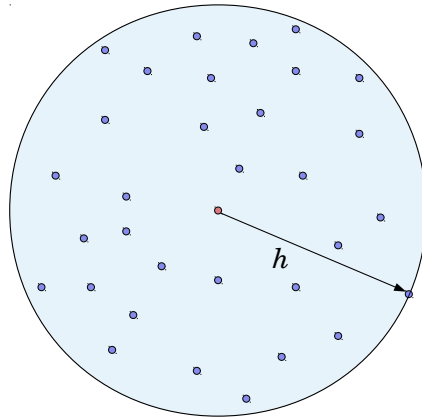


Figure 2.2: Illustration of the smoothing length h . Blue points mark neighbouring particles. The target particle is red. The light blue area shows the support domain for the central particle.

2.2 Hydrodynamics

In order to calculate the equation of motion for SPH particles, we can use the Lagrangian form of the Eulerian equations as a starting point. In this case we have a comoving coordinate system which allows us to calculate local properties in the fluid. If the function of interest is for instance $f(x, y, z, t)$, we would normally calculate the rate of change of this quantity at a fixed point in an absolute coordinate system (as the fluid moves past) with $\partial f / \partial t$. But here we are interested in the rate of change of a particular fluid element moving with the collective motion. We are therefore focusing on single SPH-particles. This derivative is often marked by a capital D .

$$\frac{Df}{Dt} = \frac{d}{dt} f(x(t), y(t), z(t), t) \quad (2.11)$$

Here, $dx/dt = v_x$, $dy/dt = v_y$, $dz/dt = v_z$ are the components of the local velocity vector \vec{v} . Using the chain rule, one gets

$$\frac{Df}{Dt} = \frac{\partial f}{\partial x} \frac{dx}{dt} + \frac{\partial f}{\partial y} \frac{dy}{dt} + \frac{\partial f}{\partial z} \frac{dz}{dt} + \frac{\partial f}{\partial t} \quad (2.12)$$

$$\frac{Df}{Dt} = \frac{\partial f}{\partial x} v_x + \frac{\partial f}{\partial y} v_y + \frac{\partial f}{\partial z} v_z + \frac{\partial f}{\partial t} \quad (2.13)$$

$$\frac{Df}{Dt} = \frac{\partial f}{\partial t} + (\vec{v} \cdot \vec{\nabla})f \quad (2.14)$$

This last equation (2.14) is called “convective derivative” and is used for the comoving form of the Euler equations.

$$\frac{D\rho}{Dt} + \rho \vec{\nabla} \cdot \vec{v} = 0 \quad (2.15)$$

$$\frac{D\vec{v}}{Dt} + \frac{\vec{\nabla}P}{\rho} = 0 \quad (2.16)$$

$$\frac{Du}{Dt} + \frac{P}{\rho} \vec{\nabla} \cdot \vec{v} = 0 \quad (2.17)$$

In eq. 2.17, u is the specific internal energy (internal energy per unit mass), and P describes the the gas pressure. The Euler equations, which express conservation of mass, momentum and energy, can be obtained, for an inviscid ideal gas, from the Lagrangian (Eckart, 1960)

$$L = \int \rho \left(\frac{\vec{v}^2}{2} - u \right) dV. \quad (2.18)$$

By discretizing the Lagrangian, it is possible to derive the SPH equations of motion using the variational principal of classical mechanics. This is the alternative to using the continuum equation directly.

$$L_{SPH} = \sum_i \left(\frac{m_i \vec{v}_i^2}{2} - m_i u_i \right) \quad (2.19)$$

It is important to note here, that the assumption has been made that the specific internal energy of a gas particle can be represented by an entropic function A_i , denoting the specific thermodynamic entropy of particle i (Springel, 2010). This function is also used in Gadget-2, as we will see in the next chapter. The pressure

of particle i is then given as

$$P_i = A_i \rho_i^\gamma = (\gamma - 1) \rho_i u_i \quad (2.20)$$

where γ is the adiabatic index. The specific internal energy can be calculated from eq. 2.20 as

$$u_i(\rho_i) = A_i \frac{\rho_i^{\gamma-1}}{\gamma - 1}. \quad (2.21)$$

If ρh^3 is kept constant, as discussed above (eq. 2.10), the density can be calculated directly from the positions of the according neighbouring particles, and the smoothing length.

$$\rho_i = \rho_i(\vec{r}_1, \vec{r}_2, \dots, \vec{r}_{N_{SPH}}, h_i) \quad (2.22)$$

This last equation also implicitly expresses the fact that for the smoothing length $h_i = h_i(\vec{r}_1, \vec{r}_2, \dots, \vec{r}_{N_{SPH}})$ only the positions of the particles are needed. The equation of motion (eq. 2.24) can be obtained from the Lagrange equation

$$\frac{d}{dt} \frac{\partial L}{\partial \vec{r}_i} - \frac{\partial L}{\partial \vec{r}_i} = 0. \quad (2.23)$$

The full derivation can be found for instance in Springel (2010), but to present this here in detail would go beyond the boundaries of this thesis.

$$\frac{d\vec{v}_i}{dt} = - \sum_{j=1}^{N_{SPH}} m_j \left[f_i \frac{P_i}{\rho_i^2} \nabla_i W(|\vec{r}_i - \vec{r}_j|, h_i) + f_j \frac{P_j}{\rho_j^2} \nabla_i W(|\vec{r}_i - \vec{r}_j|, h_j) \right] \quad (2.24)$$

with

$$f_i = \left[1 + \frac{h_i}{3\rho_i} \frac{\partial \rho_i}{\partial h_i} \right]^{-1} \quad (2.25)$$

Chapter 3

Gadget-2

In this chapter the public version of Gadget-2 and its most important features are presented. The modifications and extensions, which had been applied are addressed in the following chapter.

Gadget-2 is an N-body/SPH code completely written in C and parallelized with the standard MPI communication interface by Volker Springel. The publicly available version was released in 2005 and is still broadly used today. It offers an optional particle-mesh scheme for the hierarchical tree algorithm. Gadget-2 can be used for a large variety of different astrophysical problems, because it contains numerous options of already included simulation settings for special behaviour, like for instance periodic boundary conditions and it can be used either fully cosmological or non-cosmological.

3.1 Collisionless Dynamics and Gravity

Dark matter and star particles behave like collision-less fluids in the code and therefore fulfil the collision-less Boltzmann equation

$$\frac{df}{dt} \equiv \frac{\partial f}{\partial t} + \vec{v} \frac{\partial f}{\partial \vec{x}} - \frac{\partial \Phi}{\partial \vec{r}} \frac{\partial f}{\partial \vec{v}} = 0 \quad (3.1)$$

The potential Φ is the solution of Poisson's equation

$$\vec{\nabla}^2 \Phi(\vec{r}, t) = 4\pi G \int f(\vec{r}, \vec{v}, t) d\vec{v}, \quad (3.2)$$

where $f(\vec{r}, \vec{v}, t)$ is the single-particle phase-space density function. This complicated system of differential equations can much more easily be solved using the N-body approach. It should be noted here, that a gravitational softening is introduced into the potential, to prevent close encounters between particles. At

small separations the gravitational force would get very strong leading to large-angle scattering. For many N-body particles, direct summation of all gravitational forces would lead to a computational time consuming algorithm of the order of $\mathcal{O}(N^2)$, where N is the number of particles. Gadget-2 however, offers the possibility to make use of a Tree algorithm, which lowers the computational cost to order $\mathcal{O}(N \log(N))$ (Barnes and Hut, 1986). This method will be briefly presented in the following section.

3.2 Tree Algorithm

The basic idea of a tree algorithm is to let the target particle interact with individual groups of distant particles, instead of computing gravitational forces for each and every one of them. In the classical Barnes & Hut tree (Barnes and Hut, 1986), the total simulation volume is enclosed by a cubical box, called "the root node". This volume is divided into eight smaller nodes, each with half of the side length. It is checked for each of the smaller boxes, whether they contain more than one particle or not. If they contain multiple particles it is further subdivided into eight daughter cells, and so on. If each node contains only one or no particle, the tree is fully constructed. To calculate forces, this tree must be "walked". It means that at first the root node is considered and then the algorithm goes hierarchically down to smaller nodes. After each step it is decided if the multipole expansion of the node would provide a calculated force with sufficient accuracy, or not. If this is not the case, the node has to be "opened", which means going to the next lower hierarchical level. This procedure is illustrated in figure 3.1.

A gravitational tree algorithm can be characterized by 3 different parameters

1. the Type of grouping,
2. the order of the multipole expansion,
3. the opening criterion.

Considering the first point, the oct-tree used in Gadget-2 has been chosen because of its comparatively good memory consumption. Another advantage is the clean geometry of its structure. All nodes are cubical and it can be used therefore as a very effective searching tool. This is especially important for quickly finding neighbouring SPH particles and it also helps to keep the magnitudes of higher-order multipoles small, because problems due to large aspect ratios of the nodes are prevented. Nevertheless, in Gadget-2 the authors decided to use a monopole expansion, because of the extremely memory efficient tree construction, which is

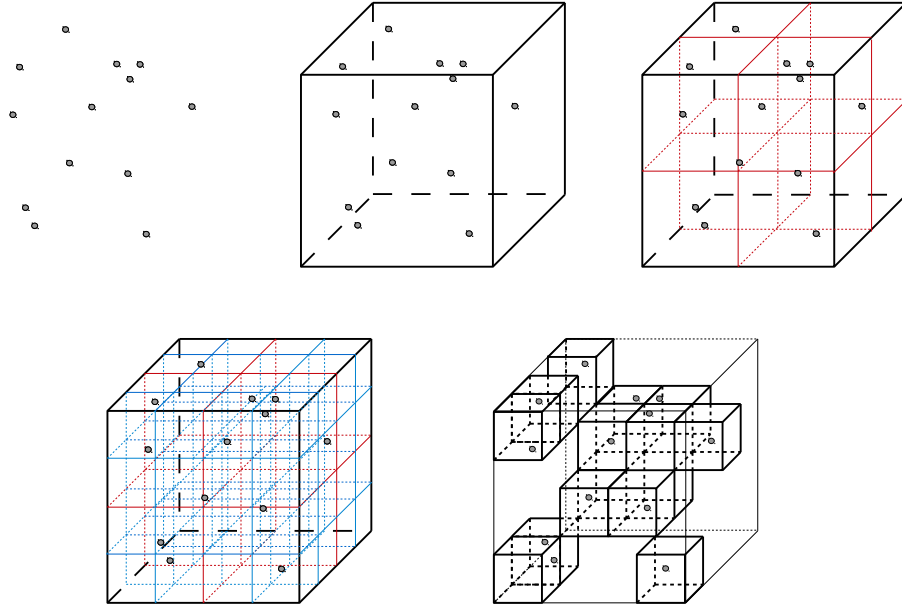


Figure 3.1: Schematic illustration of the tree construction. From left to right: The simulation volume gets enclosed by one single cubic "root node". It is then split into eight smaller nodes, and so on, until every node is populated by only one particle or no particle. Nodes which do not have any particles can be deleted.

carried out dynamically, considering different timestep sizes. The opening criterion for monopole moments used in Gadget-2, calculates the relative force error for each interaction between a particle and a node

$$\frac{GM}{r^2} \left(\frac{l}{r}\right)^2 \leq \alpha |\vec{a}|, \quad (3.3)$$

with $|\vec{a}|$ being the length of the acceleration vector from the last timestep. α is a tolerance parameter, which should be set carefully (see section 6.1). l indicates the side length of the cubic node and M is the total mass it contains. r is the distance between the node and the particle for which the force is calculated. In eq. 3.3, the left hand side is a rough estimate of the error introduced due to the monopole expansion (truncation error), which is then compared with the expected total magnitude of the force. Therefore, this criterion tries to hold the estimated error of the force calculation for every interaction between a particle and a tree node constant, within some tolerance boundary. In some cases it might happen,

that a particle is located in a node and still satisfies this cell acceptance criterion. For such small distances the calculated error could get out of bounds. To prevent this from happening, a second opening criterion is used, in which it is examined whether the distance between the geometric center of the node and the particle's position is larger than 0.6 times the side length of the node, or not.

$$|\vec{r}_k - \vec{c}_k| \leq 0.6l \quad k \in \{1, 2, 3\} \quad (3.4)$$

where \vec{c}_k is the position of the geometric center of a node and \vec{r}_k the location of the particle in that node.(Springel, 2005).

3.3 Neighbour Search

The oct tree algorithm can also be used as a powerful neighbour search tool. To find the nearest particles, in Gadget-2 the tree is walked, while after every hierarchical level the search region is compared with the tree node. If there is a geometric overlap between the two regions, the daughter cells of the tree node are considered, otherwise this path of the tree is not followed further down. This flexible approach is one of the causes for the very good performance of this code.

3.4 The Tree Particle Mesh Method

A normal tree method is very efficient for highly clustered systems, but if the particles are almost homogeneously distributed, it is better to use a fixed mesh. The force resolution is then limited by the mesh cell size. If the size however is too small, the simulation would be too computational expensive. More complicated algorithms, like adaptive mesh refinement for instance would be needed. Another way is to combine the gravity tree with the particle mesh (Xu, 1995). In Gadget-2 it is possible to use such a "hybrid method", instead of using a pure gravity tree algorithm. The basic idea here is to split the gravitational forces into a long range and a short range part. This is done by considering the potential in Fourier space. The different modes Φ_k are split as follows:

$$\Phi_k = \Phi_k^{long} + \Phi_k^{short}, \quad (3.5)$$

with

$$\Phi_k^{long} = \Phi_k e^{-k^2 r_s^2} \quad (3.6)$$

and

$$\Phi_k^{short} = \Phi_k \left[1 - e^{-\vec{k}^2 r_s^2} \right], \quad (3.7)$$

where r_s is the spacial scale of the "force-split". The short range part of the force is calculated by transforming equation 3.7 back into real space. For a single point mass m in a periodic box with side length L , one gets for $r_s \ll L$:

$$\Phi^{short}(\vec{x}) = -\frac{Gm}{r} \operatorname{erfc} \left(\frac{r}{2r_s} \right), \quad (3.8)$$

with $r = \min(|\vec{x} - \vec{r} - \vec{n}L|)$ being the smallest distance of all images of this particle to the point \vec{x} . \vec{n} is an arbitrary integer triplet of the point mass at \vec{r} relative to the point \vec{x} (Springel, 2014, 2005). erfc is the so-called complementary error function defined as:

$$\operatorname{erfc}(x) = 1 - \operatorname{erf}(x) = \frac{2}{\sqrt{\pi}} \int_x^\infty e^{-t^2} dt. \quad (3.9)$$

3.5 Hydrodynamics

The basic hydrodynamic equations, including the equation of motion in SPH, which are adopted in Gadget-2, already have been presented in section 2.2. Here a few additional notes are necessary. If one assumes that shocks and external heating sources are not present, the entropy A_i of each particle would be conserved. However in astrophysical simulations, discontinuities will commonly happen and these shocks need to be damped by an artificial viscosity.

$$\left. \frac{dv_i}{dt} \right|_{\text{visc}} = - \sum_{j=1}^N m_j \Pi_{ij} \vec{v}_{ij} \cdot \vec{\nabla}_i \bar{W}_{ij} \quad (3.10)$$

This viscous force transforms kinetic energy of SPH particles into heat. The rate of change of entropy due to artificial viscosity is

$$\left. \frac{dA_i}{dt} \right|_{\text{visc}} = \frac{1}{2} \frac{\gamma - 1}{\rho_i^{\gamma-1}} \sum_{j=1}^N m_j \Pi_{ij} \vec{v}_{ij} \cdot \vec{\nabla}_i \bar{W}_{ij}, \quad (3.11)$$

or expressed for the internal energy

$$\left. \frac{du_i}{dt} \right|_{\text{visc}} = \frac{1}{2} \sum_{j=1}^N m_j \Pi_{ij} \vec{v}_{ij} \cdot \vec{\nabla}_i \bar{W}_{ij}, \quad (3.12)$$

where \overline{W}_{ij} is the arithmetic average of the kernel function for both particles

$$\overline{W}_{ij} = \frac{1}{2} [W_{ij}(h_i) + W_{ij}(h_j)] \quad (3.13)$$

and Π_{ij} is in Gadget-2, based on Monaghan (1997),

$$\Pi_{ij} = -\frac{\alpha (c_i + c_j - 3w_{ij})w_{ij}}{2 \rho_{ij}}. \quad (3.14)$$

Here $w_{ij} = \vec{v}_{ij} \cdot \vec{r}_{ij} / |\vec{r}_{ij}|$ is the relative velocity projected on the vector of the separation between particle i and j . If the particles approach each other $\vec{v}_{ij} \cdot \vec{r}_{ij} < 0$, otherwise w_{ij} is set to zero (Springel, 2005). c_i and c_j are the sound speed for particle i and j accordingly and $\rho_{ij} = (\rho_i + \rho_j)/2$. An additional viscosity limiter is used in Gadget-2 to damp spurious transport of angular momentum in shear flows. For this purpose, the viscous tensor is multiplied by $(f_i + f_j)/2$, with

$$f_i = \frac{|\vec{\nabla} \times \vec{v}|_i}{|\vec{\nabla} \cdot \vec{v}|_i + |\vec{\nabla} \times \vec{v}|_i} \quad (3.15)$$

which gives the relative amount of shear, measured around particle i . This is done after evaluating SPH estimates for divergence and curl in file "*density.c*", which is very handy, because the divergence for particle i can later directly be used as a divergence criterion for star formation routines.

3.6 Time Integration

For the time evolution in Gadget-2, the so-called kick-drift-kick (KDK) leapfrog integrator is used. This time integration scheme is second order accurate and completely time-symmetric. This means that theoretically the initial conditions could be reproduced by integrating backwards in time (Springel, 2014). The KDK integrator calculates alternately position and velocities for each "active" particle. Gadget-2 uses individual timesteps, because not all particles need to have the same accuracy in time. Therefore, some particles will get fewer "kicks" than others. There are also global timesteps, which synchronize all particles after a while.

The time-step criterion used for N-body particles in Gadget-2 is

$$\Delta t_{grav} = \min \left[\Delta t_{max}, \left(\frac{2\eta\epsilon}{|\vec{a}|} \right)^{1/2} \right], \quad (3.16)$$

where Δt_{max} is the maximum allowed timestep, η is an accuracy parameter (see

section 6.2), ϵ is the gravitational softening and \vec{a} the acceleration vector of the particle. For SPH particles, the Courant condition is additionally taken into account, leading to a timestep criterion of the form

$$\min [\Delta t_{grav}, \Delta t_{i,hyd}] \quad (3.17)$$

with the hydrodynamic timestep for particle i given as

$$\Delta t_{i,hyd} = \frac{C_{courant} h_i}{\max_j (c_i + c_j - 3w_{ij})}. \quad (3.18)$$

In this last equation, c_i and c_j are the sound speed for particles i and j , h indicates the smoothing length and $C_{courant}$ is the so-called Courant factor, which is an important accuracy parameter and must be set carefully in the parameter file. \max_j means, that the maximum of $c_i + c_j - 3w_{ij}$ is taken, considering all j neighbouring particles of particle i .

The operators in this scheme update position \vec{x} , velocity \vec{v} , pressure P and entropy S stored in the particle arrays as follows:

$$K' \left(\frac{\Delta t}{2} \right) : \begin{cases} \vec{x}^n \mapsto \vec{x}^n \\ \vec{v}^n \mapsto \vec{v}^{n+\frac{1}{2}} = \vec{v}^n + \vec{a}^n \frac{\Delta t}{2} \\ P^n \mapsto P^n \\ S^n \mapsto S^{n+\frac{1}{2}} = S^n + \dot{S}^n \frac{\Delta t}{2} \end{cases} \quad (3.19)$$

$$D(\Delta t) : \begin{cases} \vec{x}^n \mapsto \vec{x}^{n+1} = \vec{x}^n + \vec{v}^{n+\frac{1}{2}} \Delta t \\ \vec{v}^{n+\frac{1}{2}} \mapsto \vec{v}^{n+\frac{1}{2}} \\ P^n \mapsto P^{n+1} = \left(S^{n+\frac{1}{2}} + \dot{S}^n \frac{\Delta t}{2} \right) \rho^{(n)} \gamma \\ S^{n+\frac{1}{2}} \mapsto S^{n+\frac{1}{2}} \end{cases} \quad (3.20)$$

$$K'' \left(\frac{\Delta t}{2} \right) : \begin{cases} \vec{x}^{n+1} \mapsto \vec{x}^{n+1} \\ \vec{v}^{n+\frac{1}{2}} \mapsto \vec{v}^{n+1} = \vec{v}^{n+\frac{1}{2}} + \vec{a}^{n+1} \frac{\Delta t}{2} \\ P^{n+1} \mapsto P^{n+1} \\ S^{n+\frac{1}{2}} \mapsto S^{n+1} = S^{n+\frac{1}{2}} + \dot{S}^{n+1} \frac{\Delta t}{2} \end{cases} \quad (3.21)$$

The time evolution operator $U(\Delta t)$ can be approximated, according to the idea of

operator splitting, as $\tilde{U} = K' \left(\frac{\Delta t}{2} \right) D(\Delta t) K'' \left(\frac{\Delta t}{2} \right)$ (Springel, 2005; Briggs, 2012). One could also split the drift operator instead of the kick operator (drift-kick-drift). Interestingly, it turns out that, in some cases, the leapfrog scheme has a much better performance compared to other commonly used integration techniques like Runge-Kutta for instance. Volker Springel shows this for the Kepler Problem, where the long term evolution of the system is obviously much better using the leapfrog-algorithm because of its very good energy conservation (Springel, 2005).

Chapter 4

Extensions of Gadget-2

This chapter is organized in 3 sections, approaching the most important astrophysical processes implemented in Gadget-2 within this project so far. These are

1. Cooling
2. Star Formation
3. Feedback

Each part will include a brief introduction of the theory and a description of the way it is implemented in the code.

4.1 Cooling

4.1.1 Theory

Cooling of gas is one of the most fundamental physical processes for structure formation and the evolution of galaxies and star formation. Due to the temperature decline, the density of the interstellar medium will automatically rise, and is therefore the main cause for star formation. For a hot medium ($T > 10^6$ K) cooling is mostly dominated by thermal bremsstrahlung. It is often called free-free emission, because free electrons are scattered by ions without being captured and therefore remain free. The resulting decelerations lead to the emission of radiation and hence reduce the energy of the medium. For temperatures $10^6 > T > 10^4$ K, where the medium is not fully ionized, line transitions are the dominant cooling mechanism. For low temperatures ($T < 10^4$ K) more complex physical processes are involved considering cooling, like for instance the higher number of available energy levels in molecules, but also collisional ionization and recombination.

Atoms can get ionized by collisions with free electrons, leading to a decline of the kinetic energy of the gas. If electrons recombine with ionized atoms, energy gets radiated away due to the release of photons. This also happens if during the collision not enough kinetic energy is provided for ionization, but only for pushing the electron to a higher energy level (collisional excitation), from which it will decline after a short time releasing energy.

4.1.2 Implementation

For simulations of dwarf galaxies, a metal-dependent cooling function is needed, which spans over temperatures between 100 K up to 10^8 K. The cooling rates from Boehringer and Hensler (1989) for gas with temperatures above 10^4 K were used and from Dalgarno and McCray (1972) for temperatures below 10^4 K. Additionally molecular cooling from H_2 and HD is taken into account using calculations of Hollenbach and McKee (1979) as well as Lipovka et al. (2005). The resulting cooling function is used as a lookup table, from which the code interpolates between different temperature values and metallicities. It was originally prepared by Mykola Petrov and also used in Liu et al. (2015). The complete cooling function is shown in figure 4.1. It was calculated for five different metallicities ranging from 2×10^{-5} ($10^{-3} Z_\odot$) to 4×10^{-2} . As discussed by Boehringer and Hensler (1989) it is interesting to note the marginal dependency on metallicity for the hot medium below $Z = 1/100 Z_\odot$ (magenta dotted line in fig. 4.1). The increase of the cooling rate for metal poor gas around 10^3 to 10^4 K is caused by the contribution from HD and H_2 . HD is hydrogen deuteride which is believed to play an important role for cooling after the recombination phase in the primordial medium (Lipovka et al., 2005) and can therefore also be considered for the formation of early epoch, isolated dwarf galaxies. The number fraction with respect to atomic hydrogen was assumed to be 10^{-8} and for H_2 10^{-5} . The cooling rate for $T < 10^4$ K therefore consists of the following parts:

$$\mathcal{L}_{H,T < 10^4} = n_e n_H f_i \Lambda_{e^-} + n_H^2 \Lambda_{Atom} + n_{tot}^2 \Lambda_{H_2} + \Lambda_{HD} \quad (4.1)$$

where n_e and n_H are the number densities for electrons and hydrogen atoms respectively and $n_{tot} = n_H + 2n_{H_2}$ with n_{H_2} being the number density for H_2 . f_i stands for the ionisation fraction of the medium, which is not exactly calculated in the code and therefore treated as a free parameter. Above 10^4 K, hydrogen is assumed to be fully ionized and therefore $f_i = 1$, but for $T < 10^4$ K it is set to a value of 10^{-4} , which was also assumed in Liu et al. (2015). $\Lambda_{e^-}, \Lambda_{Atom}, \Lambda_{H_2}$

and Λ_{HD} are the cooling rates for free-free emission, collisions with H-atoms, and molecules respectively, in units of $\text{erg cm}^3/\text{s}$. Figure 4.1 presents the cooling rate in units of $\text{erg}/\text{cm}^3/\text{s}$, because the number densities are normalized to $n_e n_H = 1 \text{ cm}^{-6}$, $n_H^2 = 1 \text{ cm}^{-6}$ and $n_{tot}^2 = 1 \text{ cm}^{-6}$.

For temperatures above 10^4 K, only the first term from equation 4.1 needs to be taken into account due to the dominance of free-free emission:

$$\mathcal{L}_{T>10^4} = n_e n_H f_i \Lambda_{e^-} \quad (4.2)$$

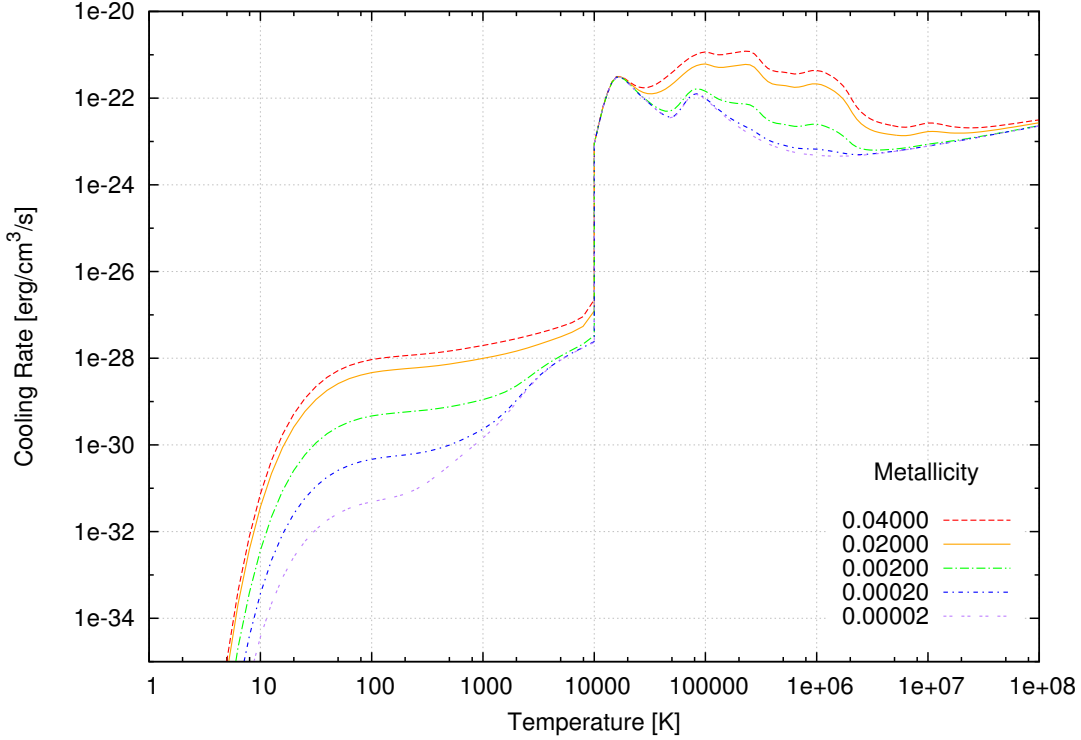


Figure 4.1: Cooling rates for different Temperatures and different metallicities Z , where 0.02 corresponds to solar metallicity. The ionization fraction was assumed to be 10^{-4} for temperatures below 10^4 K and 1 for temperatures above 10^4 K. The number densities for electrons n_e , for hydrogen n_H and $n_{tot} = n_H + 2n_{H_2}$ are normalized to 1.

The change of the internal energy due to cooling is calculated as:

$$\frac{du}{dt} = -\frac{n_H^2 \Lambda(T, Z)}{\rho} \quad (4.3)$$

To reduce the so-called overcooling problem (Stinson et al., 2006), a way of calcu-

lating the internal energy for the end of the current time step implicitly is used, as described in Springel et al. (2001). At first the adiabatic rate of change of the specific internal energy must be evaluated, which is actually done in Gadget-2 automatically, at least for the entropy. From the rate of change of the specific entropy, which is saved for each particle, the specific internal energy can easily be derived using

$$u_{ad} = \frac{A(s)}{\gamma - 1} \rho^{\gamma-1} \quad (4.4)$$

Where $A(s)$ is the entropy function and γ the adiabatic index of the ideal gas. Once this is done, the internal energy for particle i at the end of the time step $u_i^{(n+1)}$ can be numerically calculated.

$$u_i^{(n+1)} = u_i^{(n)} + \dot{u}_{ad} dt - \frac{n_H^2 \Lambda(u_i^{(n+1)}, Z)}{\rho_i^{(n)}} dt \quad (4.5)$$

Note that for the cooling rate in the previous equation is depending on the specific internal energy at the end of the time step. A root finding method must be used for this task, like for instance the bisection method, where equation 4.5 is solved for $u_i^{(n+1)}$ until an accuracy parameter (10^{-6} in this case) is reached. It shows that this happens within just about 30 iterations in most of the cases. The resulting rate of change of the specific internal energy is then evaluated as

$$\dot{u}_i = \frac{u_i^{(n+1)} - u_i^{(n)}}{dt} \quad (4.6)$$

This must be calculated back into the rate of change of the specific entropy \dot{A} . As mentioned in Springel et al. (2001) it is a good idea to prevent the predicted energies from overshooting by letting a particle at most lose half of its internal energy during a given time step, otherwise in some cases, when the cooling time gets too short, negative energies or other catastrophic behaviour could occur. Additionally, cooling gets shut off for a specific amount of time, if the gas particle in question is located near a star particle with ongoing feedback from type II supernovae. This will be discussed in detail in section 4.3.

4.2 Star Formation

4.2.1 Theory

Star particles in SPH-simulations usually do not represent single stars, but whole single stellar populations (SSP). Considering the resolutions in the presented simulations, it would be futile to resolve single individual stars. The mass of a SSP should be at least $1000 M_{\odot}$. It is well known from observations, that stars typically form in clusters consisting of many individuals and one can assumed, that the age of those stars is approximately the same for all members, but their masses are quite evenly distributed. The number of stars dN in such a population, within a specific mass range $[m, m + dm]$ is given by the initial mass function (IMF). A classical IMF formulation is that of Salpeter (1955).

$$dN = \xi(m)dm = km^{-\alpha}, \quad (4.7)$$

where k is a normalization factor. In this context, the initial mass function plays an important role for feedback processes. The tables which were used are taken from Liu (2013) and were calculated using the Kroupa IMF (Kroupa et al., 1993).

$$\xi(m) = \begin{cases} 0.035m^{-1.3} & \text{if } 0.08 \leq m < 0.5, \\ 0.019m^{-2.2} & \text{if } 0.5 \leq m < 1.0, \\ 0.019m^{-2.7} & \text{if } 1.0 \leq m < 100 \end{cases}$$

The mass limits are fixed at values of $0.08 M_{\odot}$ and $100 M_{\odot}$. The SSPs behave like normal N-body particles in the simulation. Additionally, also a smoothing length is applied to them in order to distribute feedback mass, metals and energy over the neighbour particles in a weighted manner, using the kernel function. The star formation rate (SFR) is defined as the amount of gas mass which gets turned into star mass per time unit. It was already introduced as a power law by Schmidt (1959) in the form

$$\Sigma_{SFR} = A\Sigma_{gas}^N \quad (4.8)$$

where A is simply a constant of proportionality, N the value of the power, which is found to be between 1 and 2 and Σ_{gas} the surface gas density. The well known Kennicutt-Schmidt Law from Kennicutt (1998a) is commonly used as a standard relation, but only for gas discs in pressure equilibrium. Starburst dwarf galaxies

for instance do not fit the Kennicutt-Schmidt law (Kuehtreiber, 2010).

$$\Sigma_{SFR} = (2.5 \pm 0.7) \times 10^{-4} \left(\frac{\Sigma_{gas}}{1 \text{M}_{\odot} \text{pc}^{-2}} \right)^{1.4 \pm 0.15} \text{M}_{\odot} \text{yr}^{-1} \text{kpc}^{-2} \quad (4.9)$$

To simulate star formation, tunable efficiency parameters are introduced so that the overall SFR in galaxies is close to this relation. In the presented, heavily modified Gadget-2 version, star formation was implemented in two different ways, which are described in detail in the following subsections. First, the standard star formation recipe based on Katz (1992) and Stinson et al. (2006) was used and secondly a self regulated, temperature-dependent star-formation recipe from Koeppen et al. (1995), where there is almost no need for free parameters anymore.

4.2.2 Stochastic Star-Formation Recipe

This star-formation algorithm is an advanced version of the original one, developed by Katz (1992) and is often referred to as the standard star-formation recipe for SPH simulations. The basic idea here is, to check for all gas particles in the whole simulation if a set of star-formation criteria are fulfilled. The subset of those particles, which are actually eligible to form stars undergo further calculations, from which it is decided probabilistically whether they spawn star particles or not. The criteria adopted for this simulation are the following:

1. Is the density of the gas particle higher than $n_{\text{thresh}} = 12.2 \text{ cm}^{-3}$?
2. Is the temperature of the gas particle below $T_{\text{thresh}} = 15000 \text{ K}$?
3. Is the particle part of a converging flow?

The density criterion which was used in Stinson et al. (2006), was actually 0.1 cm^{-3} . Due to better resolution, it is possible in this case to use a threshold of 12.2 cm^{-3} which corresponds to a mass density of $2.65 \times 10^{-23} \text{ g cm}^{-3}$ using a mean molecular weight of $\mu = 1.3$. This is the highest density which is reachable using only gravity for the SPH parameters set in the reference simulations for this project.

$$\rho_{\text{thresh}} = \frac{N_{\text{ngb}} m}{\epsilon^3}, \quad (4.10)$$

where N_{ngb} is the number of neighbouring particles (32 for this case), m is the mass of gas particles, which is $1.96 \times 10^9 \text{ M}_{\odot}$ in the present model and ϵ is the

gravitational softening length of 0.2 kpc. The temperature threshold of 1.5×10^4 K was directly adopted from Stinson et al. (2006) as well as the convergence criterion $\text{div } \vec{v} < 0$, which implies that the gas particles are approaching each other. This divergence of the velocity field can be calculated using the following equation:

$$\nabla \cdot \vec{v} = \frac{1}{\rho_i} \sum_{j=1}^N m_j (\vec{v}_j - \vec{v}_i) \cdot \nabla_i W(|r_{ij}|, h_i) \quad (4.11)$$

Katz (1992) takes the SFR to be proportional to $\rho_{gas}^{3/2}$, where ρ_{gas} is the local gas density. The change of the stellar density ρ_\star is the negative change of the gas density ρ_{gas} and is assumed to be

$$\frac{d\rho_\star}{dt} = -\frac{d\rho_{gas}}{dt} = \frac{c_\star \rho_{gas}}{t_{gas}} \quad (4.12)$$

or

$$\frac{d \ln \rho_{gas}}{dt} = -\frac{c_\star}{t_{gas}} \quad (4.13)$$

where c_\star is a free, tunable, SFR parameter and t_{gas} is the time it takes the gas to collapse. In Katz (1992) $\max(\tau_{dyn}, \tau_{cool})$ was used for temperatures above 3×10^4 K, where τ_{dyn} is the dynamical time scale

$$\tau_{dyn} = \frac{1}{\sqrt{4\pi G \rho_{gas}}} \quad (4.14)$$

and τ_{cool} is the cooling time, which can be evaluated by

$$\tau_{cool} = u \left(\frac{du}{dt} \right)^{-1} \quad (4.15)$$

where u is the internal energy of a gas particle. If one absorbs τ_{dyn} (eq. 4.14) into t_{gas} in eq. 4.12, it is clear why the SFR is proportional to $\rho_{gas}^{3/2}$ here. For temperatures below 3×10^4 K, t_{gas} was always taken to be τ_{dyn} . Because of the temperature threshold which ensures that star forming regions must be below 1.5×10^4 K, Stinson does not use the cooling time for equation 4.12. As mentioned before, star formation is in this case simulated stochastically using the following probability function.

$$p = \frac{m_{gas}}{m_\star} \left(1 - e^{-c_\star \frac{\Delta t}{\tau_{dyn}}} \right) \quad (4.16)$$

Here m_{gas} refers to the mass of the gas particle and m_{\star} to the mass of the star particle, which probably gets spawned. A random number r which is drawn between 0 and 1 finally decides whether the star particle is really created, if $r < p$, or not. In Stinson et al. (2006) the mass of star particles are a constant fraction of the original gas particle mass, which means that m_{\star} always stays the same

$$m_{\star} = \frac{m_{gas,orig}}{N_{gen}} = \text{const.} \quad (4.17)$$

where N_{gen} is the number of stellar "generations" a gas particle is allowed to form. N_{gen} can be adjusted in the code to change the mass resolution of star particles. Normally, a value of 20 is applied for the presented simulations. By the way, this is different to Katz (1992), because he uses a fixed fraction of the (current) mass of the gas particle, leading to a big variance of star particle masses. A star formation efficiency parameter ϵ^{\star} was defined in Stinson et al. (2006) as

$$\epsilon^{\star} = \frac{m_{\star}}{m_{gas}} \quad (4.18)$$

which would replace m_{gas}/m_{\star} with $\epsilon^{\star-1}$ in 4.16. ϵ^{\star} does not appear in the probability function of Katz (1992) because it can be absorbed into the definition of c_{\star} . Therefore, if one wishes to compare the parameter c_{\star} between Stinson and Katz, Stinson's c_{\star} should be multiplied by ϵ^{\star} .

4.2.3 Star Formation based on Köppen, Theis, Hensler (1995)

The star-formation recipe of Koeppen et al. (1995) is somewhat easier to implement, which will be described briefly. There are a few differences to the ideas of Katz and Stinson. In this case, the stars are not formed stochastically via a probability function, but the physical properties of gas particles are used to guess the fraction of gas, which should be active, star-forming regions. There are not really star-formation criteria, but the mass of the potentially spawned star particles gets evaluated via the so-called stellar birth function $\psi(\rho, T)$ 4.19. If this mass lies between a minimum mass boundary $m_{min} = 10^3 M_{\odot}$ and a maximum mass boundary $m_{max} = 10^6 M_{\odot}$ the particle gets spawned. This calculation is done for every gas particle once in a fixed time interval τ_{form} , which is chosen to be 10 Myr.

$$\psi(\rho, T) = C_2 \rho^2 e^{-\frac{T}{T_s}} \quad (4.19)$$

Here, $C_2 = 2.575 \times 10^8 \text{ cm}^3/(\text{g s})$ and $T_s = 1000 \text{ K}$. C_2 was adopted from Koepen et al. (1995), where a prescription of Larson (1969) is used, in which this factor is calculated from the theoretical collision rate (assuming an isotropic Maxwellian velocity distribution and inelastic collisions) of gas clouds with radii corresponding to the specific cloud density and temperature for the Jeans length. Eq. 4.19 is based on an analytical, self-regulated approach for collision-excited cooling. $f(T) = e^{-\frac{T}{T_s}}$ is an efficiency factor depending on gas temperature. The mass of the stellar particles is then evaluated by

$$m_{\star} = \psi(\rho, T)Vt_{\text{form}}, \quad V = \frac{4\pi}{3}h^3 \quad (4.20)$$

where a formation time t_{form} of 10 Myr is used.

4.2.4 Implementation

It is important to note that the spawned star particles inherit the velocities and positions of their parent gas particles. This does not create problems, because strong gravitational interactions are prevented by gravitational softening and the positions will automatically change soon because of the different numerical treatments of SPH- and N-body particles. In the programming language C, this can be done quite easily by first copying the complete array of particle i to the newly created particle $i + N_{\star, \text{new}}$. Here $N_{\star, \text{new}}$ is the number of star particles which are created during the current time step, on a specific processor. Then the type of the particle gets changed from "gas" (Type 0) to "star" (Type 4) and all other properties which are not identical to the ones of the gas particle must be changed too, e.g. the mass, which already had been calculated. One must not forget to also update the mass of the gas particle accordingly.

$$m_{\text{gas}, \text{new}} = m_{\text{gas}, \text{old}} - m_{\star} \quad (4.21)$$

To ensure that the spawned star particle has the same metallicity like the gas particle from which it originates, and also the gas particle's metallicity does not change, the masses for the 11 elements k , which are traced in the code (see section 4.3.5), also need to be updated

$$m_{\star, k} = \frac{m_{\text{gas}, k}}{m_{\text{gas}}} m_{\star} \quad (4.22)$$

$$m_{\text{gas}, k, \text{new}} = m_{\text{gas}, k, \text{old}} - m_{\star, k} \quad (4.23)$$

If the mass of the stellar particle is much bigger or equal to the new mass of the gas particle, it can simply be transformed completely into a star, by just changing its type. Only some special properties need to be set in this case, like for instance the time of its formation, which is necessary to calculate later how old the population is. This is needed to evaluate the amount of feedback from this star particle, as we will see in the next section. In the stochastic recipe one must be especially careful in case of the complete particle transformation. As mentioned above, the masses of the star particles are all the same at the time of their creation. They will only lose a specific fraction of mass due to feedback processes to surrounding gas particles. These gas particles, however, will get a higher mass, which is therefore not an integer fraction of the constant stellar mass of newly spawned particles anymore (see eq. 4.17). Because of that, the gas particles would not be able to vanish completely after producing N_{gen} SSPs and we would have gas particles with probably less than $100 M_{\odot}$. In this case, the IMF could not be filled anymore leading to unrealistic stellar populations. Additionally, particles with too little mass are also bad for resolution purposes and for the code performance. This problem can be prevented by including a tolerance for the mass of the last SSP which a gas particle is allowed to form, so that the N_{gen} -th spawned star particle can have a little bit more mass than the ones before.

4.3 Feedback Processes

Feedback is one of the main ingredients for simulation of galaxies, because from different processes a huge amount of energy is pushed back into the interstellar medium leading to self-regulated star formation. Without feedback the available gas mass in the system would be consumed very quickly. Additionally mass and newly produced elements from stars are also recycled. In the presented models, 11 different chemical elements are traced: H, He, C, N, O, Ne, Mg, Si, S, Ca, Fe and there are four different feedback processes taken into account, namely

1. stellar winds and UV-radiation
2. type II supernovae
3. type Ia supernovae
4. planetary nebulae

These mechanisms are implemented as lookup tables, from which the code reads out values for different times and metallicities and interpolates between them, similar to what was done in order to treat cooling. These tables were originally calculated by Berczik and Petrov (2003) and also used in (Liu et al., 2015). The theoretical approach shall be briefly discussed in this section.

4.3.1 Stellar Wind and UV-Radiation

Stars with masses higher than $8 M_{\odot}$ heat the surrounding ISM by stellar winds and Lyman continuum radiation. The emitted radiation per star can be approximated depending on stellar mass (Hensler, 1987; Theis et al., 1992)

$$L_{Ly} \approx 1 \times 10^{40} \left(\frac{m_{\text{star}}}{M_{\odot}} \right)^6 \text{ photons s}^{-1} \quad (4.24)$$

It is believed that only a small fraction η_{Ly} of the photon energy is converted into kinetic energy (Freyer et al., 2003, 2006). η_{Ly} was assumed to be 10^{-3} . The stellar wind component of the energy feedback for high-mass stars was calculated by Hensler (1987), who used the metal-dependent mass-loss rate which was approximated from models of Kudritzki et al. (1987). This is described in more detail also in Theis et al. (1992) and these two different processes are added together (Liu, 2013).

4.3.2 Type II Supernovae

The high mass stars will end their life after only a few 10^6 years as SNII. This number of events can be calculated by taking into account the number of stars in the mass interval $8 M_{\odot} \leq m_{star} \leq 100 M_{\odot}$ from the IMF and the stellar lifetime t_{\star} described in Raiteri et al. (1996). As an approximation of the lifetime for stars with masses between 0.6 and $120 M_{\odot}$ and metallicities of 10^{-4} up to 0.05

$$\log t_{\star} = a_0(Z) + a_1(Z) \log M + a_2(Z)(\log M)^2 \quad (4.25)$$

is used, where t_{\star} is in units of years and M in M_{\odot} . The coefficients a_0 , a_1 and a_2 are given as

$$a_0(Z) = 10.13 + 0.07547 \log Z - 0.008084(\log Z)^2,$$

$$a_1(Z) = -4.424 - 0.7939 \log Z - 0.1187(\log Z)^2,$$

and

$$a_2(Z) = 1.262 + 0.3385 \log Z + 0.05417(\log Z)^2$$

The number of exploding type II supernovae are derived from the prepared tables in intervals of 1 Myr and multiplied by an energy factor E_{SNII} of 10^{51} erg. Additionally a supernova efficiency factor SN_{eff} of 0.1 is included, as can be seen in eq. 4.26.

4.3.3 Planetary Nebulae

Let us now consider intermediate stars ($0.8 M_{\odot} \leq m_{star} \leq 8 M_{\odot}$). Those stars will evolve to asymptotic giant branch stars (AGB) and lose most of their mass due to strong stellar winds ejecting their outer envelopes. In most cases a white dwarf remnant is produced accompanied by the formation of a planetary nebula. The energy released by them is assumed to be 10^{47} erg which is much lower than for SNe, but they occur in larger quantity. Additionally, during the loss of the star's envelopes, lots of material enriched with heavy elements, mostly N and C, is reinjected into the interstellar medium, making PNe not negligible for chemodynamical simulations.

4.3.4 Type Ia Supernovae

Those intermediate stars which are in a binary system can produce type Ia supernova explosions. If one of the companions is a red giant and the secondary star a white dwarf, it might happen that the red giant overflows the Roche lobe and that the white dwarf is able to accumulate enough mass to reach the Chandrasekhar mass limit of $1.38 M_{\odot}$. In this case, the star will be completely destructed, returning all of its mass back to the ISM. This type of SNe is also the most important producer of Fe and therefore plays a key role for galaxy evolution.

4.3.5 Implementation

The feedback energy for stellar wind and Lyman continuum radiation is calculated directly from separate tables, which contain the prepared values for a SSP with a mass of $10^4 M_{\odot}$. In the code, the values which are read in are first normalized to $1 M_{\odot}$, interpolated in time and metallicity and then scaled to the mass of the stellar particle in question. The other processes are taken to be fixed energy values per events. In that case, the according number of events is derived from the tables with the same procedure. The total feedback energy ΔE of a single stellar particle within a time interval $[t, t + \Delta t]$ can therefore be written as

$$\Delta E = [\Delta E_{SW}(t) + \Delta E_{PN}(t) + \Delta E_{SNe}(t) \text{SN}_{\text{eff}}] m_{\star} \quad (4.26)$$

$$\Delta E_{PN}(t) = \Delta N_{PN}(t) E_{PN}$$

$$\Delta E_{SNe}(t) = \Delta N_{SNII}(t) E_{SNII} + \Delta N_{SNI}(t) E_{SNI}$$

where ΔN marks the number of events within Δt . The energy released per event is $E_{PN} = 10^{47}$ erg for planetary nebulae and $E_{SNII} = E_{SNI} = 10^{51}$ erg for type Ia and type II SNe. $\Delta E_{SW}(t)$ is calculated separately from the tables as a mechanical energy part $\Delta E_{SW,mech}(t)$ and a UV-radiation part $\Delta E_{SW,UV}(t)$. m_{\star} is the mass of the stellar population. SN_{eff} is the SN-efficiency factor, taken to be 10 % for the standard case. The feedback mass and cumulative number of events are visualized in figs. 4.2 and 4.3.

Apart from the feedback energy, stellar particles also give back mass and enrich the surrounding gas particles with heavy elements. As briefly mentioned before, the stellar particles do not change their overall metallicity as they evolve in time, because it is made sure that the mass fractions for every element stays the same. The neighbouring gas particles will therefore increase their mass and also their

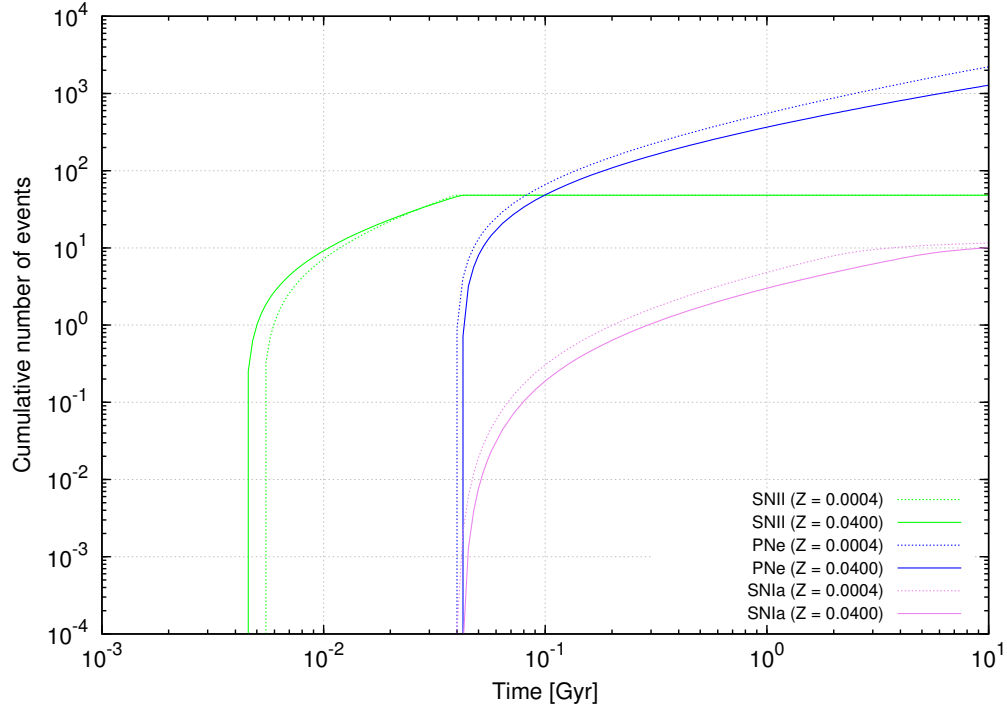


Figure 4.2: Cumulative number of events for Type II SNe (green), planetary nebulae (blue) and type Ia SNe (purple). The dotted line is for a metallicity of $Z = 0.0004$ and the solid line for $Z = 0.04$. The mass of the stellar population is $10^4 M_{\odot}$.

metallicity. If they produce new stellar populations, these will have a higher amount of heavy elements, which retroactively influences the amount of their feedback. The star particle’s mass m_{\star} and the mass fractions for each of the k elements $m_{k,\star}$ will therefore change due to feedback as

$$m_{\star,new} = m_{\star,old} - \Delta m(t, Z) \quad (4.27)$$

$$m_{\star,k,new} = m_{\star,k,old} - \Delta m(t, Z) \frac{m_{\star,k,old}}{m_{\star}}, \quad (4.28)$$

where $\Delta m(t, Z)$ is the part of the stellar particle’s mass, which is reinjected into the ISM and interpolated from the tables. The surrounding gas particles will get a specific fraction from this distributed mass and metals

$$m_{gas} = m_{gas} + \Delta m(t, Z) frac \quad (4.29)$$

$$m_{gas,k} = m_{gas,k} + \Delta m_k(t, Z) frac \quad (4.30)$$

where $m_k(t, Z)$ is the amount of mass of element k , which is lost by the SSP and distributed among all neighbouring gas particles. $frac$ can either be just the

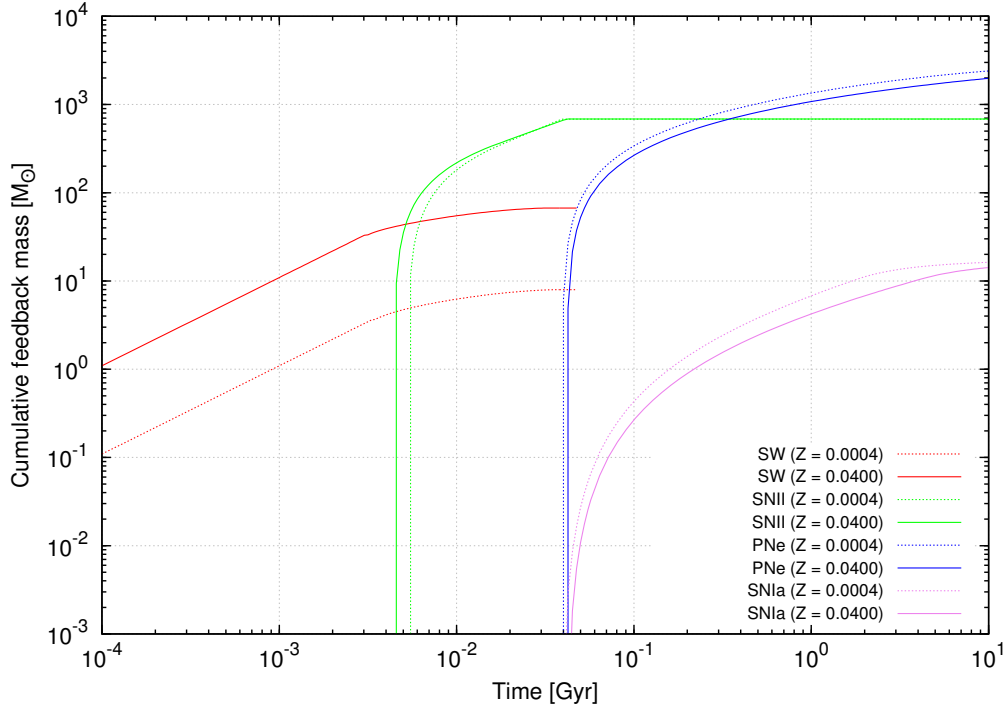


Figure 4.3: Cumulative feedback mass for stellar wind (red), Type II SNe (green), planetary nebulae (blue) and type Ia SNe (purple). The dotted line is for a metallicity of $Z = 0.0004$ and the solid line for $Z = 0.04$. The mass of the stellar population is $10^4 M_{\odot}$.

number of neighbours, or a value weighted by the kernel function. All simulations throughout this thesis are carried out with weighted feedback. To achieve this, it is necessary to change a large number of functions in Gadget-2, so that star particles also enter neighbour search routines and the evaluation of the smoothing length. A relatively large addition to the public version was also made by introducing a communication buffer for gas particles, which saves the information about feedback energy, mass, and metals. Additional functions were needed for writing into and reading from this buffer. This was necessary in order to allow feedback from stars to contribute to gas particles, which are located on a different processor. It is clear, that computation time and memory consumptions are somewhat higher, than compared to the public version of Gadget-2, especially because of the array which has to hold the 11 different elements (H, He, C, N, O, Ne, Mg, Si, S, Ca and Fe).

Chapter 5

Code Tests

5.1 Cooling Test

In this section, tests of the cooling algorithm (section 4.1), which was implemented in the code, are presented. For this purpose, all necessary parts of the cooling routine are extracted into a separate program, which makes it possible to simulate the temperature evolution, a single SPH particle would experience. This gives us the advantage that physical properties like the density and metallicity can be kept constant for this special test case and other thermodynamic processes like adiabatic heating are not present. This seems to be the best way for a proper cooling test, because it is hard to make initial conditions, for instance of a sphere with homogeneous gas distribution, which is stable at high temperatures. In this case, such a gas sphere would need to have a very low density, but then the cooling time is extremely high. On the other hand, we do not want to have a low T_{start} , because the range of the cooling function which is tested should be as big as possible. One way to do this is to constrain some initial conditions to a specific region by using boundary particles, but probably the best way of testing the cooling routine is to use precise physical values directly as input parameters, without simulating everything else.

In this case, three different metallicities and four different densities are tested, each starting with $T_{start} = 10^7$ K. The results are illustrated in fig. 5.1 and the exact values can be found in Table 5.1, along with calculated cooling times

$$\tau_c = \frac{3k_B T_{start}}{2\Lambda_0 n_H}, \quad (5.1)$$

where k_B is the Boltzmann constant, Λ_0 the cooling rate in units of $\text{erg cm}^3 \text{s}^{-1}$ and n_H the hydrogen particle density $n_H = \frac{\rho}{m_p \mu}$. From these results one can

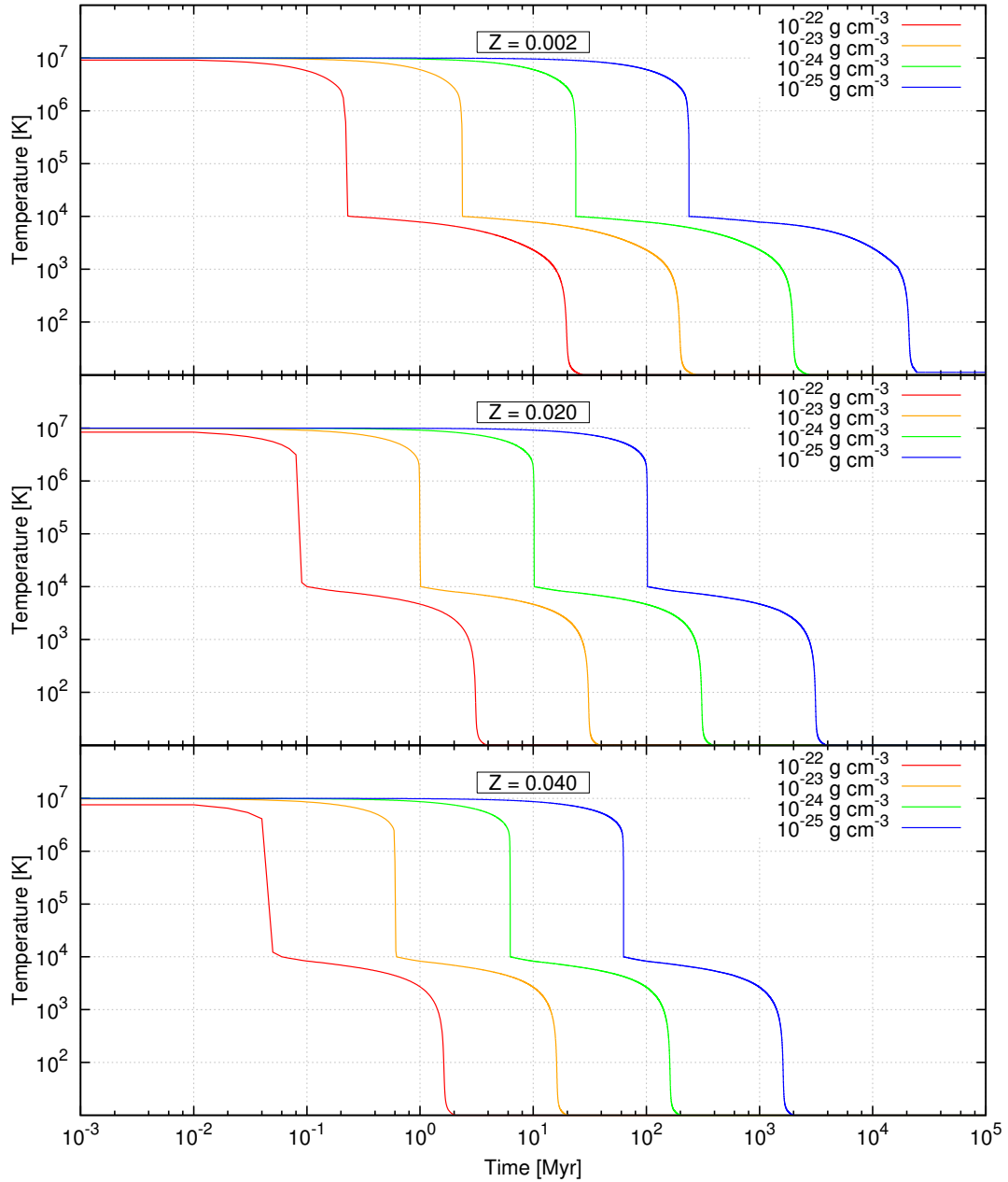


Figure 5.1: Temperature evolution for an actively cooling medium with different densities and metallicities. The densities are: $10^{-22} \text{ g cm}^{-3}$ (red curve), $10^{-23} \text{ g cm}^{-3}$ (orange curve), $10^{-24} \text{ g cm}^{-3}$ (green curve) and $10^{-25} \text{ g cm}^{-3}$ (blue curve). The upper panes corresponds to $Z = 0.1 \times Z_{\odot}$, the middle panel to $Z = Z_{\odot}$ and the bottom panel to $Z = 2 \times Z_{\odot}$.

Density [g cm ⁻³]	τ_c (Z = 0.002) [Myr]	τ_c (Z = 0.02) [Myr]	τ_c (Z = 0.04) [Myr]
10 ⁻²²	0.165	0.0844	0.0537
10 ⁻²³	1.65	0.844	0.537
10 ⁻²⁴	16.5	8.44	5.37
10 ⁻²⁵	165	84.4	53.7

Table 5.1: Calculated cooling times τ_c for different metallicities and gas densities.

see clearly that increasing the gas density by an order of magnitude, shortens the cooling time by the same factor. The metallicity also has a strong impact on the behaviour of the cooling function. The very prominent corner at $T = 10^4$ K of course comes from the transition from fully ionized to less ionized, which causes the cooling rate to drop about three orders of magnitudes there. The calculated cooling times above correspond relatively well to the simulations if one considers the time until $T = 10^4$ K is reached. These plots were also compared with Ploekinger (2014), where a similar cooling routine was used with very good agreement.

5.2 Feedback Test

In order to test the very important and highly complex feedback processes implemented, a gas cube was used with a side length of 2 kpc containing 32^3 particles. The separation between particles along the coordinate axis is therefore 62.5 pc. Each gas particle has a mass of $10^3 M_\odot$, leading to a total mass of $M = 3.277 \times 10^7 M_\odot$ and an initial density of $\rho = 2.773 \times 10^{-25}$ g cm⁻³. In the center of this homogeneous gas distribution a stellar population with a mass of $10^4 M_\odot$ is located and a metallicity of $Z = 0.0004$. $10^4 M_\odot$ is the exact value, for which the feedback tables were calculated and should therefore offer the opportunity to directly compare them with this test run, in which some special simulation behaviour was necessary. Under normal circumstances, the gas particles would start to converge towards the center of the cube, because of self gravity. For this reason, gravity was completely shut off. Also star formation and cooling were not used throughout this simulation.

One can see in figure 5.2 how feedback from the single star particle heats up the ambient medium and sweeps it up, creating an expanding superbubble as expected. A prominent shock wave is created. After 500 Myr the original simulation volume is almost gas free. Now it is easy to test if there are any implementation problems with reading in the feedback tables, filling in the correct arrays, scaling

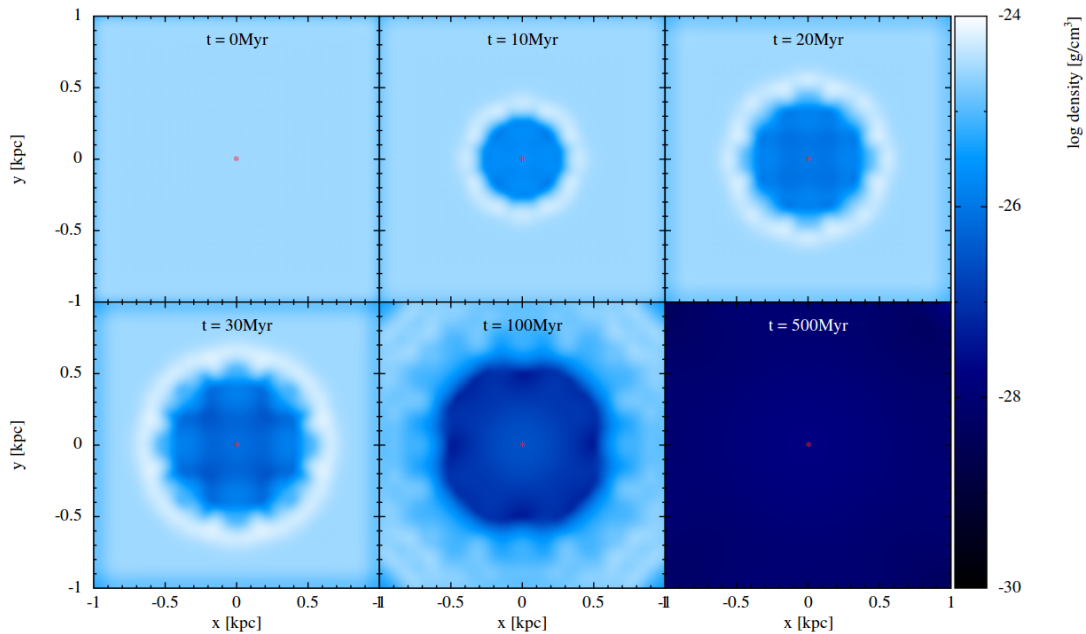


Figure 5.2: Feedback test of a cubic gas distribution. This is a thin slice through the x - y plane for 6 different times. The stellar population is located in the coordinate center and marked by a red star.

the values and so on. This can be done by simply comparing the values for the feedback mass from the tables with the values taken from all gas particles added together. The resulting feedback curve can be seen in figure 5.3, showing good accordance to the reference values. In the first few Myr, the black solid curve is exactly fitting the stellar wind feedback tables. In some parts of the plot below the first 100 Myr, one can see little "steps", which are produced by the fact that the feedback is evaluated only every 1 Myr, and not in every single time step. This would be much more computational expensive. Nevertheless, these little bumps are only a minor error source, keeping in mind that figure 5.3 presents a logarithmic time scale, letting them appear relatively large in the first few Myrs. The cumulative feedback energy is visualized in figure 5.5. This cannot be compared to the tables directly, because they contain the numbers of SNe or PNe but not the injected energy, this is only the case for the calculated stellar wind feedback. A comparison of the number of events, however is displayed in figure 5.4.

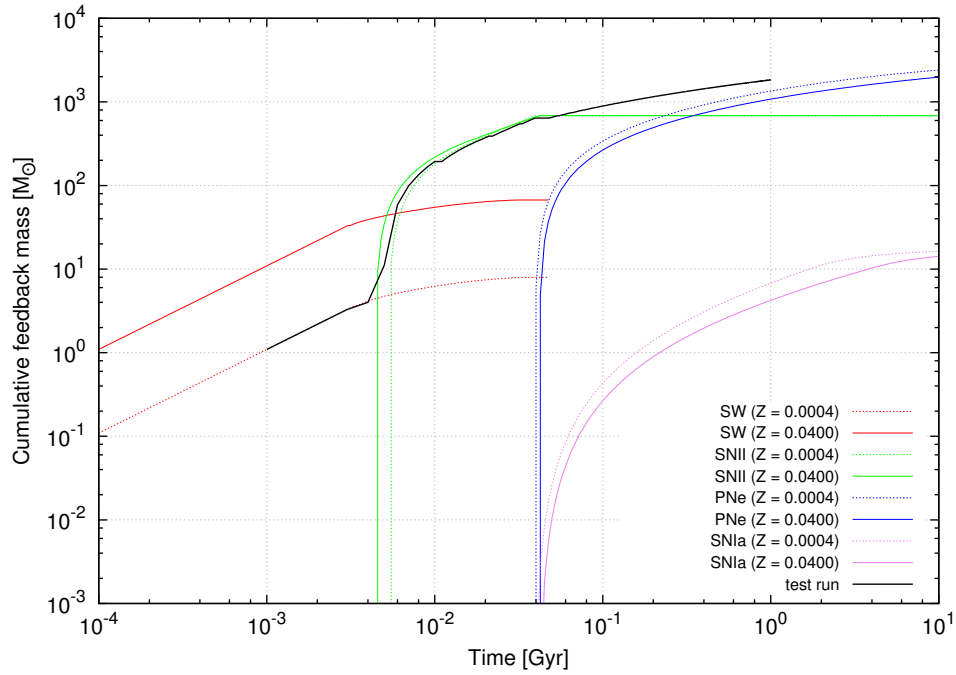


Figure 5.3: Comparison of the cumulative feedback mass as a function of time between the tables (see fig. 4.3) and the test run, indicated by the solid black line. Note that all different feedback processes are added up in the simulation

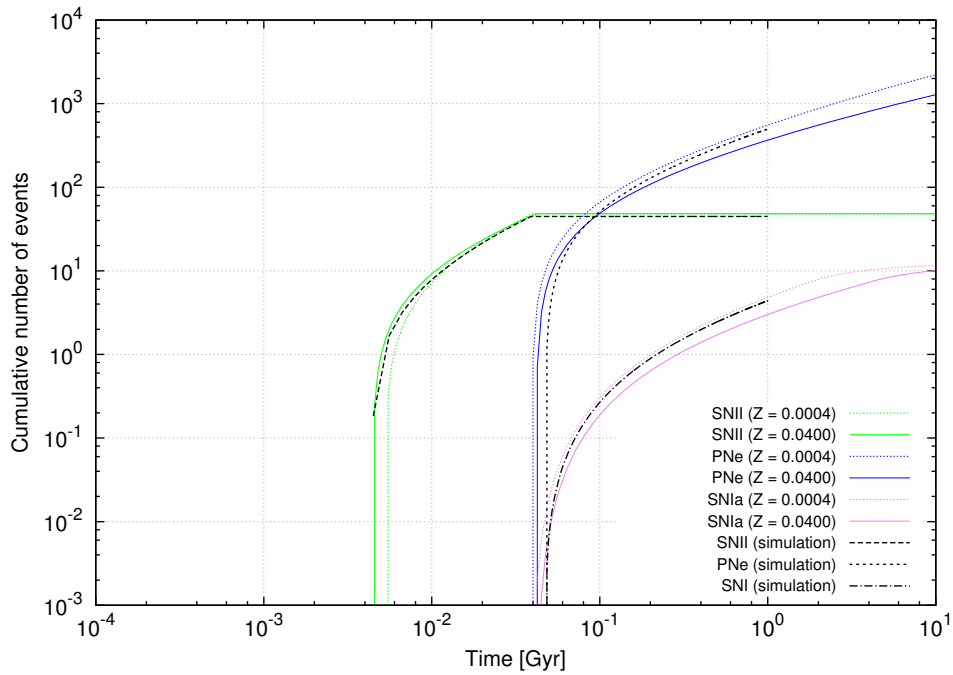


Figure 5.4: As in fig. 5.3 but for the cumulative number of SNe and PNe events.

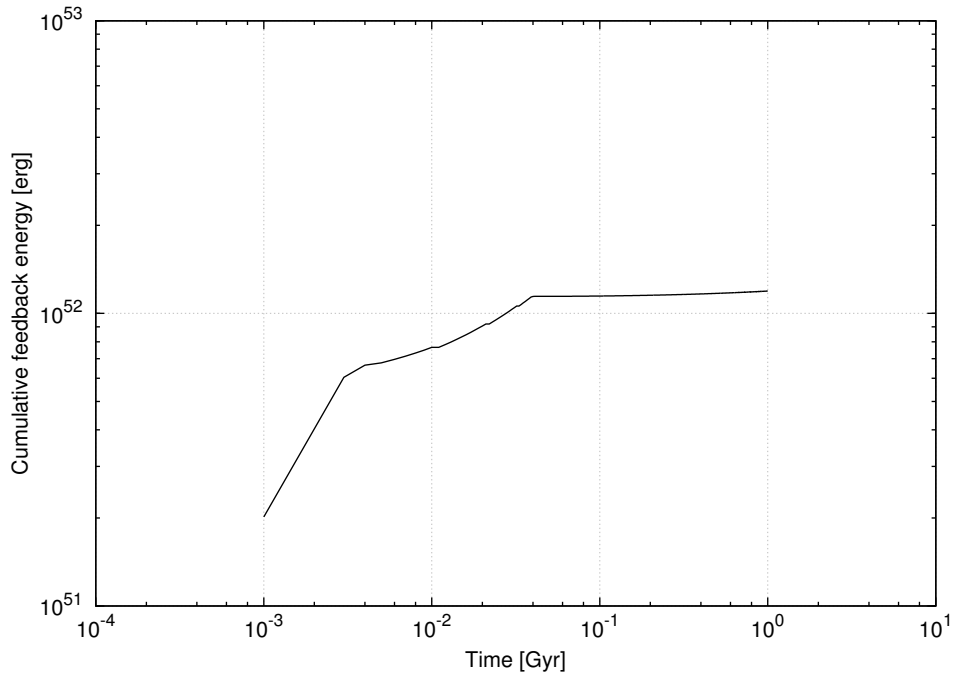


Figure 5.5: Total feedback energy from the simulation within the first Gyr.

Another useful test is to investigate if the calculated amount of feedback is also transmitted to the neighbouring gas particles correctly, because also here a large amount of error sources is present. As discussed earlier, a smoothing length is applied to stellar particles in order to distribute mass, metals, and energy in a weighted manner using the kernel function of Gadget-2. This is a very critical step, because even a small mistake in this function would sum up quickly to large errors. For this purpose, the amount of feedback mass and energy which is calculated from the single star particle in this test run is compared with the amount absorbed by all gas particles in the simulation. It shows, that the average of all resulting errors within 1 Gyr simulation time, is four orders of magnitude below a 1 percent error and therefore it can be assumed that this very small uncertainty is only caused by rounding differences. Results of the error evaluation can be seen in figure 5.6.

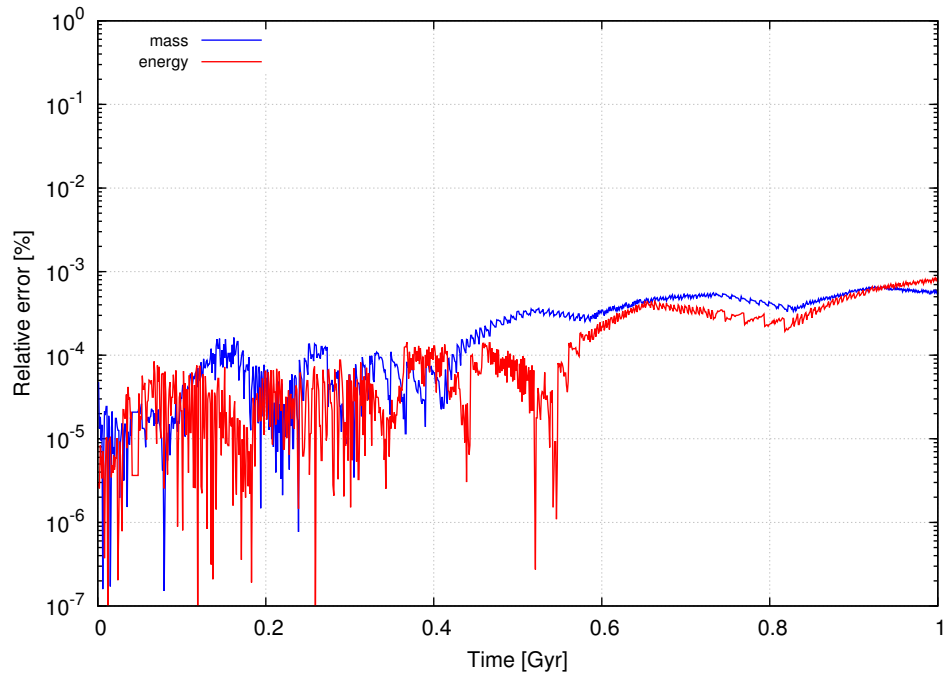


Figure 5.6: Relative discrepancy between the amount of feedback produced by the stellar population and absorbed by all gas particles. Feedback mass is represented by the blue line, energy by the red line. (The "produced" amount already includes the SN efficiency.)

Chapter 6

Simulations

6.1 Initial Conditions

For the simulations in this section, the model of an isolated dwarf galaxy has been initiated. The author wishes to make the model as close as possible to the one used in Liu et al. (2015). Gas particles are distributed according to the Miyamoto-Nagai profile

$$\rho(r, z) = \left(\frac{b^2 M}{4\pi} \right) \frac{ar^2 + (a + 3\sqrt{z^2 + b^2})(a + \sqrt{z^2 + b^2})}{[r^2 + (a + \sqrt{z^2 + b^2})^2]^{5/2} (z^2 + b^2)^{3/2}}, \quad (6.1)$$

where M is the total mass. The parameter values are chosen to be $a = 0.2$ kpc and $b = 0.75$ kpc and a maximum radius of 20 kpc has been applied. 20000 gas particles were created with $9.8 \times 10^4 M_\odot$ and a temperature of 10^4 K, leading to a cold gas mass of $1.96 \times 10^9 M_\odot$. In addition, also 4082 hot particles with $T = 10^6$ K are added, with a reduced mass of only $9.8 \times 10^3 M_\odot$. These numbers are not arbitrary, but chosen to fit the mass of cold and hot material used in Liu et al. (2015). The cause for the reduced mass is to avoid a too small number of hot particles, which are necessary to form a halo around the galaxy, preventing the gas in between from expanding into the vacuum. They do not contribute to star formation processes and therefore it shouldn't be a problem that their masses are an order of magnitude smaller than for cold gas particles. Figure 6.1 shows a color map of the Miyamoto-Nagai density profile for the parameters above.

Dark matter is modelled with a Burkert profile (eq. 6.2), using the same parameters like in the reference simulations, namely a central radius r_0 of 3 kpc and a central density ρ_0 of $0.02 M_\odot \text{pc}^{-3}$, which corresponds to approximately

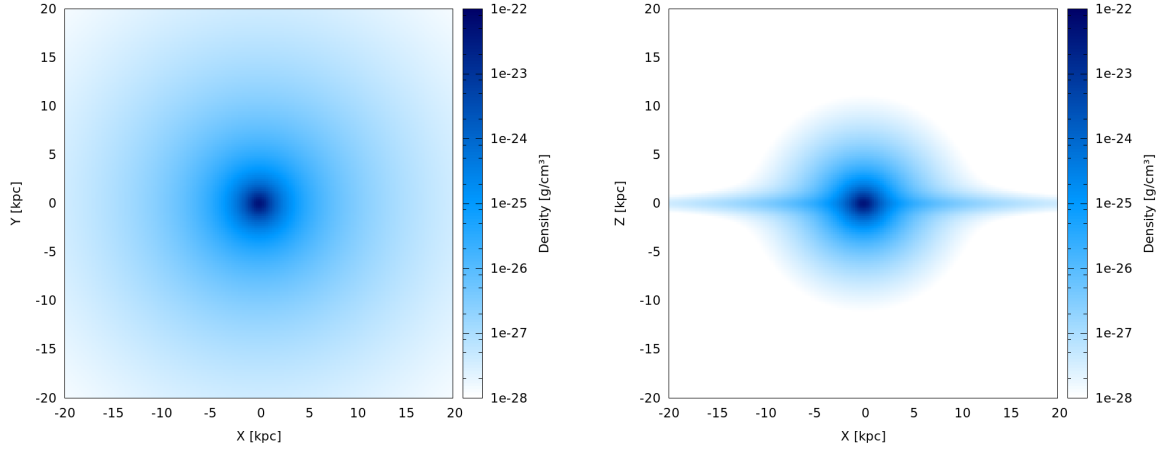


Figure 6.1: Miyamoto-Nagai profile in the xy-plane (left) and xz-plane (right), for $M = 2 \times 10^9 M_\odot$, $a = 0.2$ kpc and $b = 0.75$ kpc

$$1.35 \times 10^{-24} \text{g cm}^{-3}.$$

$$\rho(r) = \rho_0 \frac{r_0^3}{(r + r_0)(r^2 + r_0^2)} \quad (6.2)$$

The Burkert density distribution is visualized in figure 6.2. It is discretized with 50000 dark matter particles.

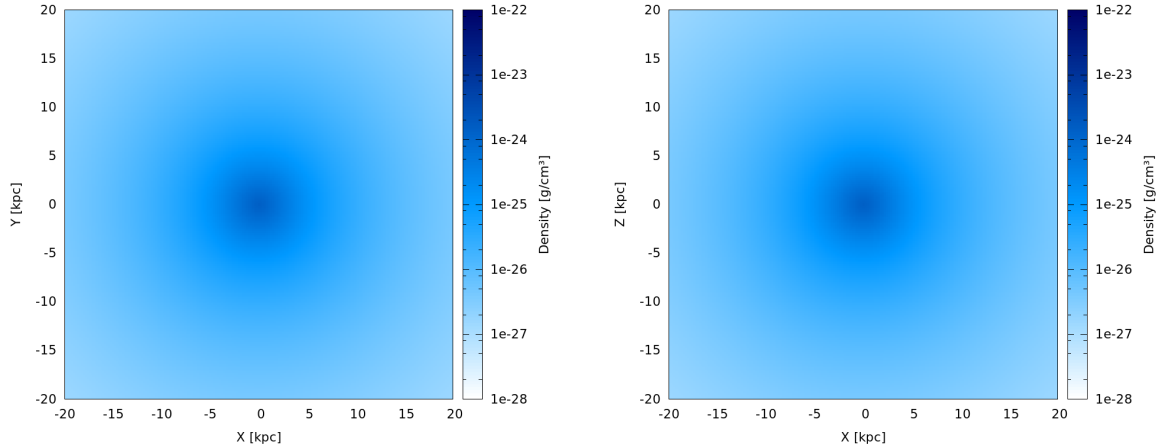


Figure 6.2: Burkert profile in the xy-plane (left) and xz-plane (right), for $\rho_0 = 0.02 M_\odot \text{pc}^{-3}$ and $r_0 = 3$ kpc.

The velocity of all gas particles is set to rotate on Keplerian orbits and a velocity dispersion of 10 km/s is additionally applied to them. The initial metallicity of gas particles is set to a mass fraction of 0.75 for H, 10^{-5} for C, N, O, Ne, Mg, Si, S, Ca and 10^{-6} for Fe. This is done in order to prevent the ratios of element

abundances, like $[\text{Fe}/\text{H}]$ and $[\text{O}/\text{Fe}]$ from starting at 0, which would be the case if an initial metallicity of some small fraction of Z_{\odot} was used.

Careful examinations revealed that the centers of mass for both, dark matter and gas were considerably off-set. The gas component seemed to be shifted approximately 200 pc from the origin of coordinates. Also the momentum vectors of all particles didn't exactly cancel each other out, as one would actually expect. This would lead to a slow shift of the galaxy, as discussed in section 6.2. After subtracting the total momentum vectors and resetting the two components into the point of origin, this problem was solved.

In a next step, these initial conditions are evolved for 200 Myr without physics, except for gas dynamics, using just a pure N-body and SPH simulation. During that time, the gas particles find a quasi-equilibrium configuration, where the gas pressure gradients equals gravitational forces. The hot particles expand outwards to higher radii, forming a halo enclosing cooler material inside. After this relaxation time, the simulation is stopped and all gas particles with a distance larger than 20 kpc are removed. The resulting initial conditions contains 23584 gas particles from 24082 in the beginning. After that, both components were again shifted, in order to relocate their centers of mass exactly in the origin of ordinates and total momenta were also subtracted again. The resulting initial conditions and their physical properties are summarized in the following table.

Component	M [M_{\odot}]	T [K]	N	a [kpc]	b [kpc]	ρ_0 [$M_{\odot} \text{ pc}^{-3}$]	r_0 [kpc]
hot gas	4×10^7	10^6	4082	0.2	0.75	-	-
cold gas	1.96×10^9	10^4	2×10^4	0.2	0.75	-	-
dark matter	9.42×10^9	-	5×10^5	-	-	0.02	3

Table 6.1: Initial conditions for the presented simulations. Hot and cold gas are in this case both part of the same single-phase description but start with different temperature values. M is the total mass of a component, T the temperature, N the particle number, a and b are the parameters of the Miyamoto-Nagai density distribution, ρ_0 is the central density of the burkert profile and r_0 its core radius.

6.2 Accuracy Parameters

As briefly mentioned, there had been some problems concerning momentum conservation, due to insufficient force and time accuracy. It is important to keep in mind that in such simulations one can not expect the total momentum to be exactly conserved, because the tree-algorithm used in Gadget-2 approximates the gravitational forces for instance. Also due to the fact that time steps cannot be

infinitesimally small, there will be obviously some errors. It is therefore very important to make sure that the accuracy parameters for force and time integration are not too large. If however, the accuracy parameters are set too small, a massive increase in computation time will occur. The user needs to choose values for the following different accuracy parameters, which can be easily changed by hand directly in the parameter file.

1. *ErrTolForceAcc*
2. *ErrTolIntAccuracy*
3. *MinSizeTimestep*
4. *MaxSizeTimestep*
5. *CourantFac*
6. *TreeDomainUpdateFrequency*

ErrTolForceAcc is the parameter α introduced in section 3.1 eq. 3.3.

$$\frac{GM}{r^2} \left(\frac{l}{r}\right)^2 \leq \alpha |\vec{a}|, \quad (6.3)$$

Here, $|\vec{a}|$ the length of the acceleration vector from the last time step, l is the extension of the tree node and r the distance between that node and the particle, for which the acceleration needs to be calculated (see section 3.1).

ErrTolIntAccuracy is the tolerance parameter η for the gravity time-step criterion described in section 3.6, eq. 3.16. It also contains *MaxSizeTimestep*, which is Δt_{max} in eq. 3.16.

$$\Delta t_{grav} = \min \left[\Delta t_{max}, \left(\frac{2\eta\epsilon}{|\vec{a}|}\right)^{1/2} \right], \quad (6.4)$$

MinSizeTimestep is just a minimum time-step value, which stops a run immediately, if this value is reached. *CourantFac* is the Courant factor for the hydrodynamic time step criterion

$$\Delta t_{i,hyd} = \frac{C_{courant} h_i}{\max_j (c_i + c_j - 3w_{ij})} \quad (6.5)$$

and *TreeDomainUpdateFrequency* is the time which has to pass until a new domain decomposition is evaluated. In order to test the effect of those accuracy settings on

the behaviour of the galaxy, a low-accuracy and high-accuracy case is calculated and the movement of the center of mass for both cases compared. The values for parameters described above can be found in table 6.2. It is interesting to note, that for the high-accuracy settings, dark matter and baryonic mass are orbiting their collective center of mass, such that its displacement from the coordinate center is not exceeding 3 pc during 1.5 Gyr, whereas for the low-accuracy case, it is a factor 100 above that and constantly increasing (see fig. 6.3 - 6.5).

Case	α	η	Δt_{max} [Gyr]	Δt_{min} [Gyr]	$C_{courant}$	f_{tree} [Gyr]
low-accuracy	5×10^{-3}	2.5×10^{-2}	10^{-4}	0	1.5×10^{-1}	10^{-3}
high-accuracy	5×10^{-5}	5×10^{-5}	10^{-4}	0	1.5×10^{-1}	10^{-3}

Table 6.2: Parameter settings for the low-accuracy and high-accuracy case.

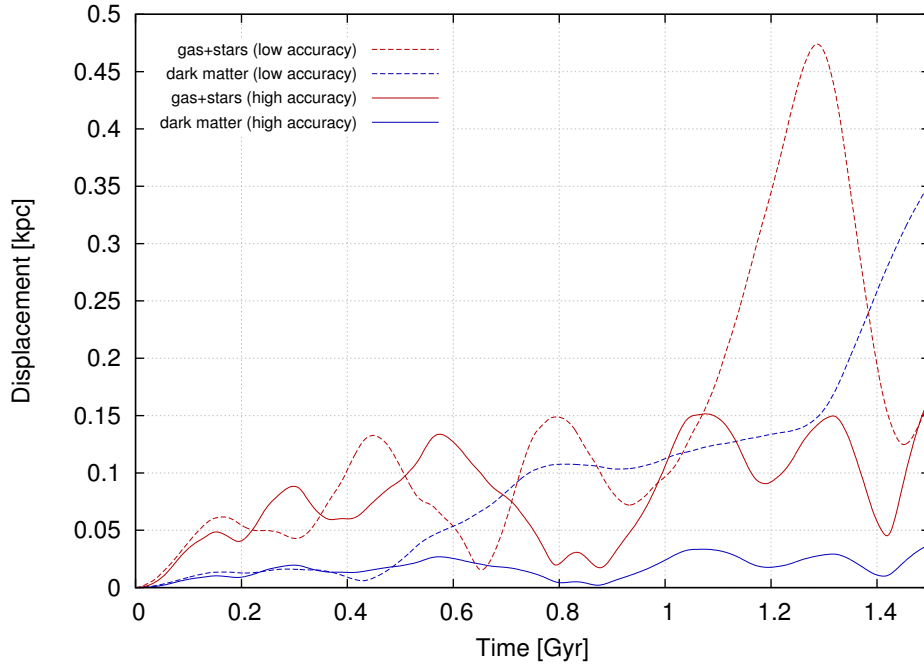


Figure 6.3: Displacement of the center of mass during the first 1.5 Gyr for gas and stars combined (red lines) and for dark matter (blue lines). Dashed lines indicate the low-accuracy case, solid lines the high-accuracy case. The displacement is the distance between the center of coordinates and the center of mass.

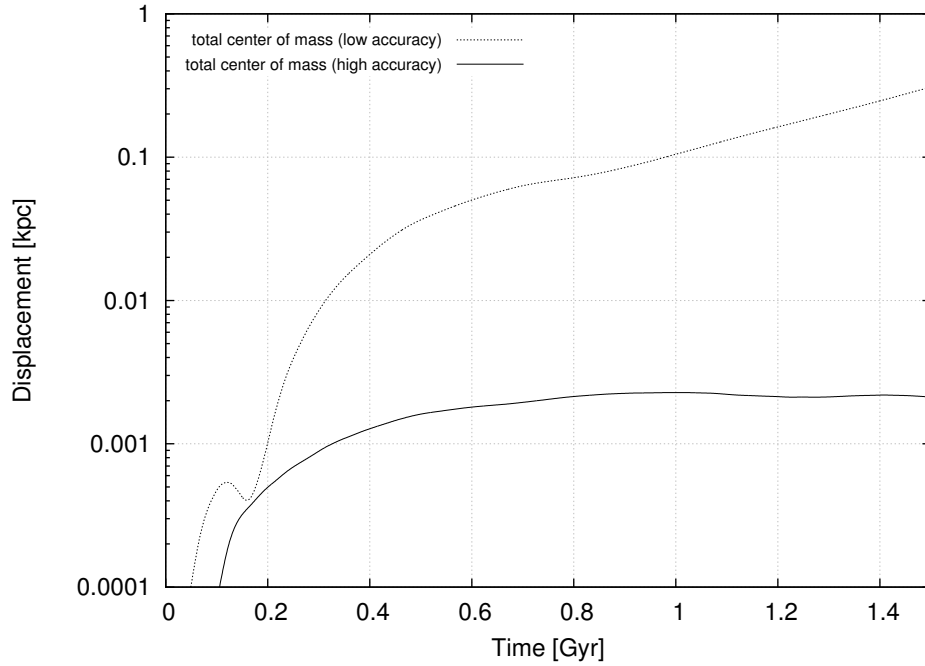


Figure 6.4: Displacement of the total center of mass during the first 1.5 Gyr. Dashed lines indicate the low-accuracy case, solid lines the high-accuracy case. The displacement is the distance between the center of coordinates and the center of mass. Note the logarithmic scale.

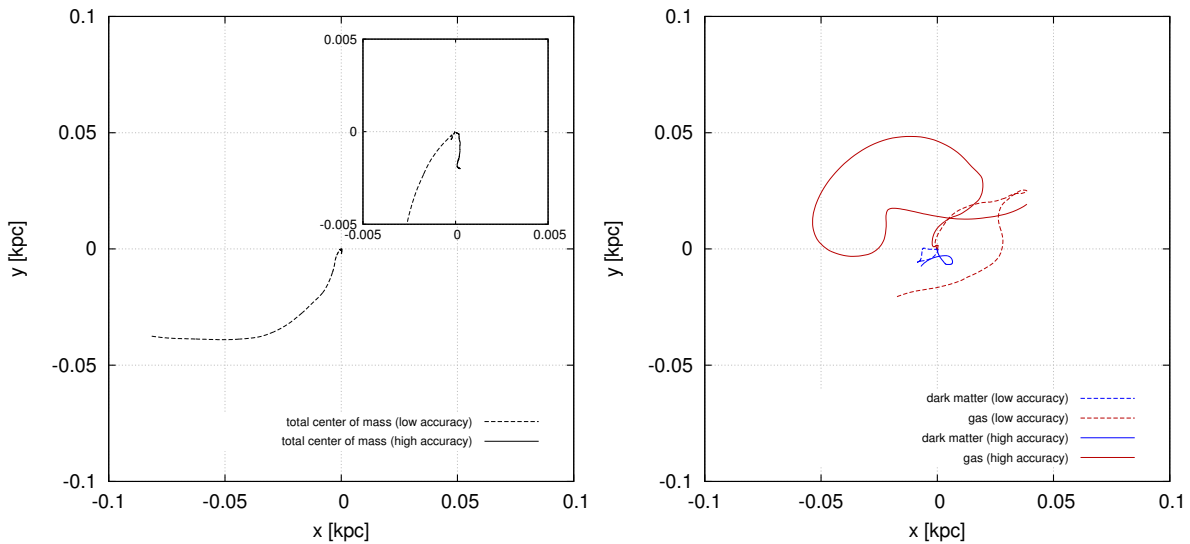


Figure 6.5: *Left:* Motion of the total center of mass during the first Gyr. Dashed lines indicate the low-accuracy case, solid lines the high-accuracy case. Note the zoom for the central ± 5 pc to see the displacement for the high-accuracy case. *Right:* Motion of the center of mass for gas (red lines) and dark matter (blue lines) during the first 300 Myr. Dashed lines indicate the low-accuracy case, solid lines the high-accuracy case.

Chapter 7

Results: Reference Simulations

In this chapter, results and comparisons of different simulation models are presented. The specific parameters for each run can be found in table 7.1. The following section will give a detailed discussion on the "reference simulations", which will be the basis for further investigations, considering the impact of free parameters on the behaviour of the system. Please note that runs in which the self-regulated SF recipe is used, are indicated by "sr" followed by a serial number. For the stochastic SF recipe, runs are marked with "sto". A simulation run using the initial conditions described in 6.1 is carried out with the exact same parameters for the two different star formation recipes. The minimum temperature for these and all the following simulations is 1000 K. A gravitational softening for gas, stars, and dark matter of $\epsilon = 0.2$ kpc is adopted and the supernova efficiency is set to $SN_{eff} = 0.1$. Gas particles near type II SNe have their cooling shut off for 1 Myr. The stochastic SF recipe based on Stinson et al. (2006) is carried out with $N_{gen} = 20$, which means every gas particle can form at least 20 stellar populations before it disappears. The SF thresholds are set to $n = 12.2 \text{ cm}^{-3}$ and $T_{thresh} = 15000 \text{ K}$. The efficiency factor in the exponential term of equation 4.16 is not changed at all, but kept at the standard value of 0.1 (Stinson et al., 2006). In the following subsections, these two reference runs sr01 and sto01 are discussed in detail.

7.1 Mass Evolution

A comparison of the total stellar and gas mass of both runs reveals, that the stochastic SF scheme converts more gas mass into stars after the first 100 Myr (see fig. 7.1). Interestingly, the initial starburst due to activation of cooling and SF happens almost instantaneously when the self-regulated recipe is used. One reason

Name	τ_{CSO} [Myr]	ϵ [kpc]	SN_{eff} [%]	SF-recipe	t_{sim} [Gyr]
sr01	1	0.2	10	self-reg.	3.0
sr02	10	0.2	10	self-reg.	3.0
sr03	20	0.2	10	self-reg.	3.0
sr04	30	0.2	10	self-reg.	3.0
sr05	1	0.1	10	self-reg.	2.9
sr01	1	0.2	10	self-reg.	3.0
sr06	1	0.5	10	self-reg.	3.0
sr07	1	1.0	10	self-reg.	3.0
sr08	1	0.2	5	self-reg.	3.0
sr01	1	0.2	10	self-reg.	3.0
sr09	1	0.2	100	self-reg.	3.0
sto01	1	0.2	10	stochastic	3.0
sto02	10	0.2	10	stochastic	3.0
sto03	20	0.2	10	stochastic	3.0
sto04	30	0.2	10	stochastic	3.0
sto05	1	0.1	10	stochastic	2.7
sto01	1	0.2	10	stochastic	3.0
sto06	1	0.5	10	stochastic	3.0
sto07	1	1.0	10	stochastic	3.0
sto08	1	0.2	5	stochastic	3.0
sto01	1	0.2	10	stochastic	3.0
sto09	1	0.2	100	stochastic	3.0

Table 7.1: Calculated models and their most important specific simulation parameters. τ_{CSO} is the cooling shut-off time, ϵ is the gravitational softening length, SN_{eff} is the SN efficiency, and t_{sim} the simulation time.

for this is the temperature threshold used by Stinson et al. (2006). Although the density threshold is fulfilled in the beginning for a small region in the center of the galaxy ($r < 0.6$ kpc), temperatures are higher than 1.5×10^4 K. This happens due to adiabatic heating during the 200 Myr relaxation time, because the initial temperature for most of the gas particles was originally set to 10^4 K (see 6.1). The little bumps between 0.1 and 0.3 Gyr in figure 7.1 are related to ejected material which falls back into the system, triggering new starbursts. The other recipe does not show such features. As expected from these findings, one can see in fig. 7.2, that the SFR of the self-regulated recipe lies approximately three times below the stochastic one, most of the time.

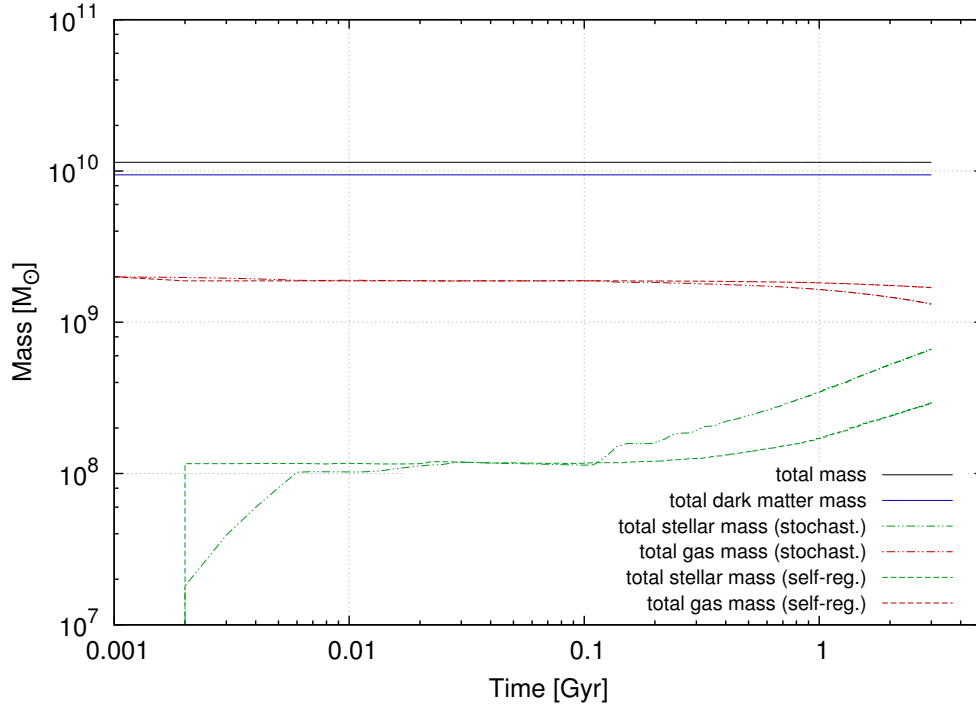


Figure 7.1: Mass evolution of two comparison runs with the stochastic SF recipe (double-dotted dashed line) and the self-regulated one (dashed line). Gas mass is illustrated in red and stellar mass in green. The blue and black solid lines show dark matter and total mass of the system, respectively. Note that these stay constant and both simulations were carried out using the same initial conditions.

7.2 Density and Temperature Distribution

The central gas density of the model galaxy is approximately $2 \times 10^{-22} \text{ g cm}^{-3}$. The initial starburst seems to be more concentrated, when the self regulated SF recipe is used. This can be seen in fig. 7.3, where after 50 Myr the blue dashed-dotted line shows two broad peaks, which are caused by the huge explosion in the central region sweeping up gas material. For a short time, a radius of about 1 or 1.5 kpc gets almost completely free of gas. The stochastic recipe also seems to produce a starburst beginning in the center, which travels outside. The density threshold used, is 12.2 cm^{-3} , which corresponds to $3.71 \times 10^{-23} \text{ g cm}^{-3}$ can be found in fig. 7.3 as vertical grey dashed line. One can see, that the region above this line, is only about 1.2 kpc in diameter. Due to the propagation outwards of the supershell, a much larger area can form stars later on, leading to a stronger gas ejection and small additional starbursts after 100 Myr, as described above. After a longer time, the maximum density stays clearly lower if the stochastic scheme is used, but the density gradient does not appear to be as strong as for the self

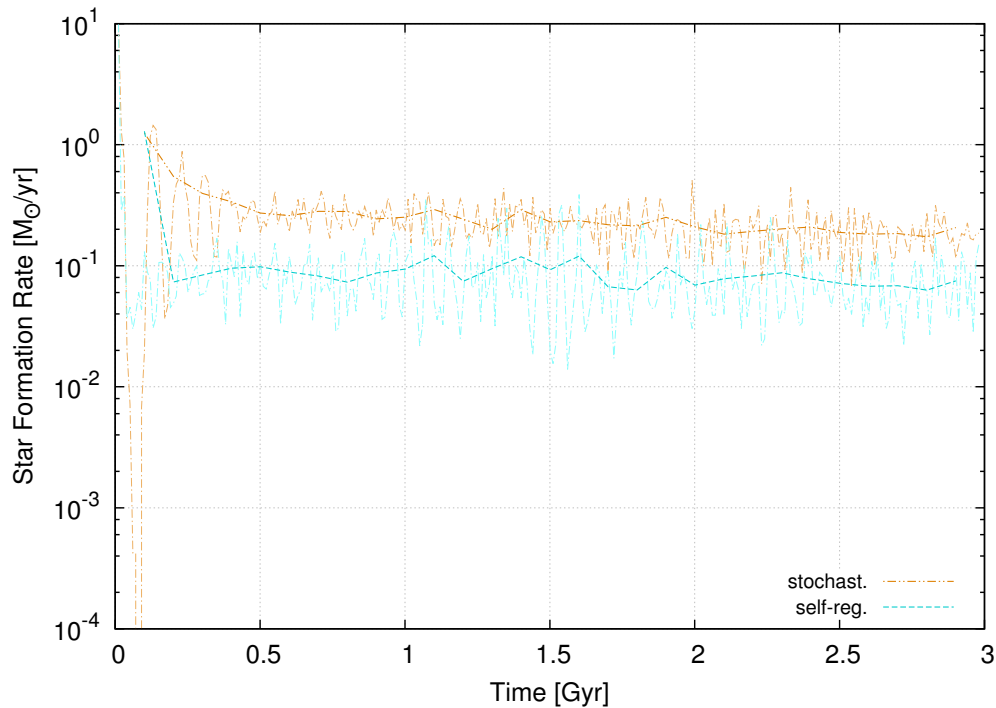


Figure 7.2: Comparison of SFRs for the reference simulations with the stochastic SF recipe (orange double-dotted dashed line) and the self-regulated one (light blue dashed line). The bin sizes for this figure was 100 Myr (heavy lines) and 10 Myr (light colors).

regulated one.

It is also interesting to take a look at the temperature distribution. At the beginning, the original initial conditions are already evolved for 200 Myr. During this time the gas is heated up adiabatically due to the high density in the center. After cooling and star formation are turned on, the temperature drops quickly to 10^4 K, therefore the temperature threshold used in the stochastic recipe reduces the star formation only in the very beginning, but star formation rises soon afterwards. The resulting feedback is so strong, that star formation almost stops completely until a simulation time of 100 Myr is reached (fig. 7.2). This happens mainly because the expanding material can not satisfy the density threshold any more, but also the convergence criterion suppresses star formation efficiently during this expansion phase of the galaxy.

Comparing density directly with the corresponding temperature for each gas particle, one is able to plot a "phase-space" diagram, which is commonly used in literature and reveals interesting insights into the dynamical behaviour of the gas. Figure 7.5 shows a direct comparison for the two SF recipes at the same moments in time. On the left column, it can be clearly seen that gas lies just

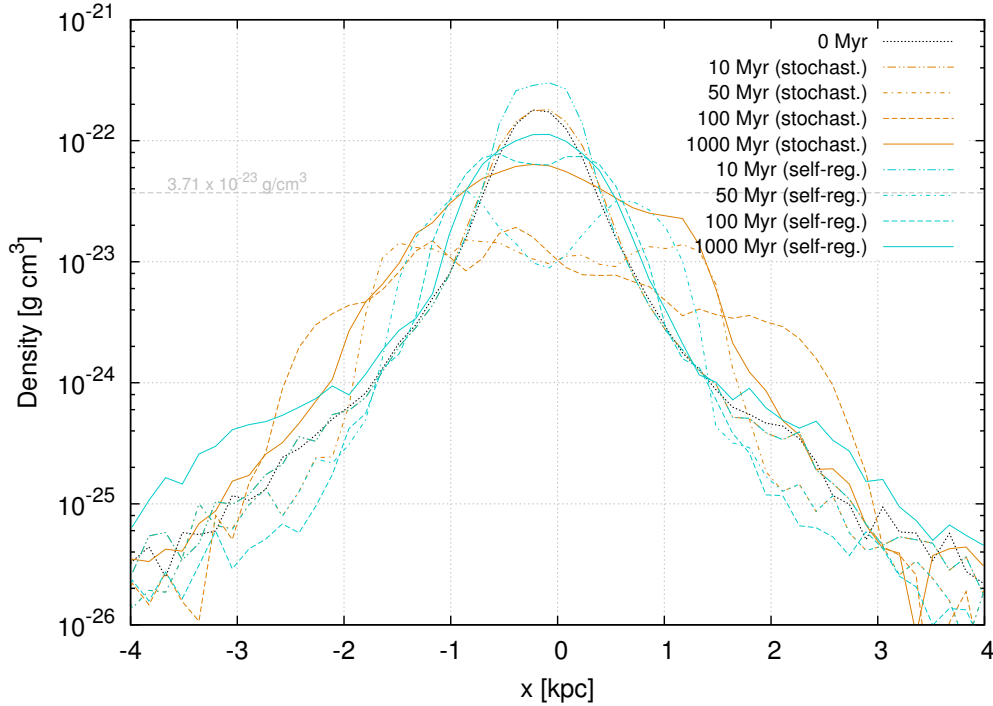


Figure 7.3: Comparison of the density distribution along the x-axis at 4 different times for each SF recipe. Orange lines indicate the stochastic scheme and turquoise lines show results from the self-regulated SF recipe. The grey vertical dashed line shows the density threshold used by the stochastic approach. The values are derived within a ± 5 kpc cut in the x-y plane, and radially binned using 64 segments.

outside of the zone between the threshold values (grey dashed lines in fig. 7.5). Only SPH particles in the lower right corner are eligible to form stars in the stochastic recipe. After 10 Myr, in both simulations the initial starburst is still ongoing, although it is more intense with the self-regulated recipe (see the second line of panels in fig. 7.5). The next panels are extracted at a simulation time of 50 Myr, where a dramatic disparity between the two runs is visible. In these simulations a giant super bubble developed during the first starburst, but using the stochastic star formation recipe, SPH particles stay trapped inside a radius of ~ 1 kpc. This leads to a thin, left-tilted feature in the phase-space diagram, because due to the expansion of the superbubble, density is declining. On the other hand, these particles are not allowed to cool due to the presence of many stars of the first generation, which are still in their type II SN phase. At this time, the expansion already reaches its maximum and some of the material inside the shock front starts to fall back into the center. Additionally, one can see that in this case almost no gas particle is able to fulfil the density threshold anymore, because of this strong expansion. The superbubble of the self-regulated scheme cannot

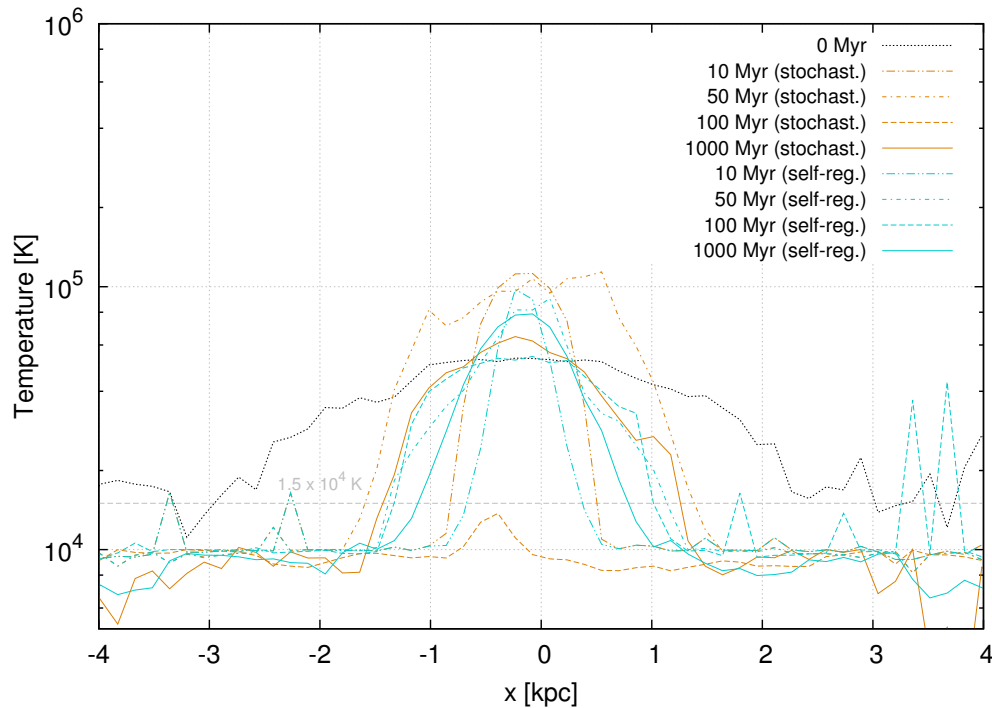


Figure 7.4: Comparison of the temperature distribution at 4 different times for each SF recipe. Orange lines indicate the stochastic scheme. The grey vertical dashed line shows the temperature threshold. Turquoise lines show results from the self-regulated SF recipe. The values are derived within a ± 5 kpc cut in the x-y plane, and radially binned using 64 segments.

hold the hot dense gas inside, leading to fast outflows in positive and negative vertical direction. The expelled material attains very rapidly lower densities while cooling, because a large fraction of it is already outside the reach of Type II SNe, as visible in fig. 7.5. This leads to a more prominent scattering of data points in the left panel, at 50 Myr. At later times, after these turbulent motions are over, both phase-space diagrams look very similar. They show a hot medium of gas particles near the central star formation region, which are constantly heated up, while cooling is shut off. This medium tends to expand and propagate outwards, but further investigations show that it cannot efficiently penetrate through cooler outer layers of gas in the model galaxy. Most of this material stays trapped near the center. Once these gas particles reach a radius where cooling gets turned on again, they will radiate away their internal energy quickly, because they still have a high temperature and density. At the same time, cool material from the outer regions exert pressure on the center, forming a cool envelope around the core, where SF is almost always happening.

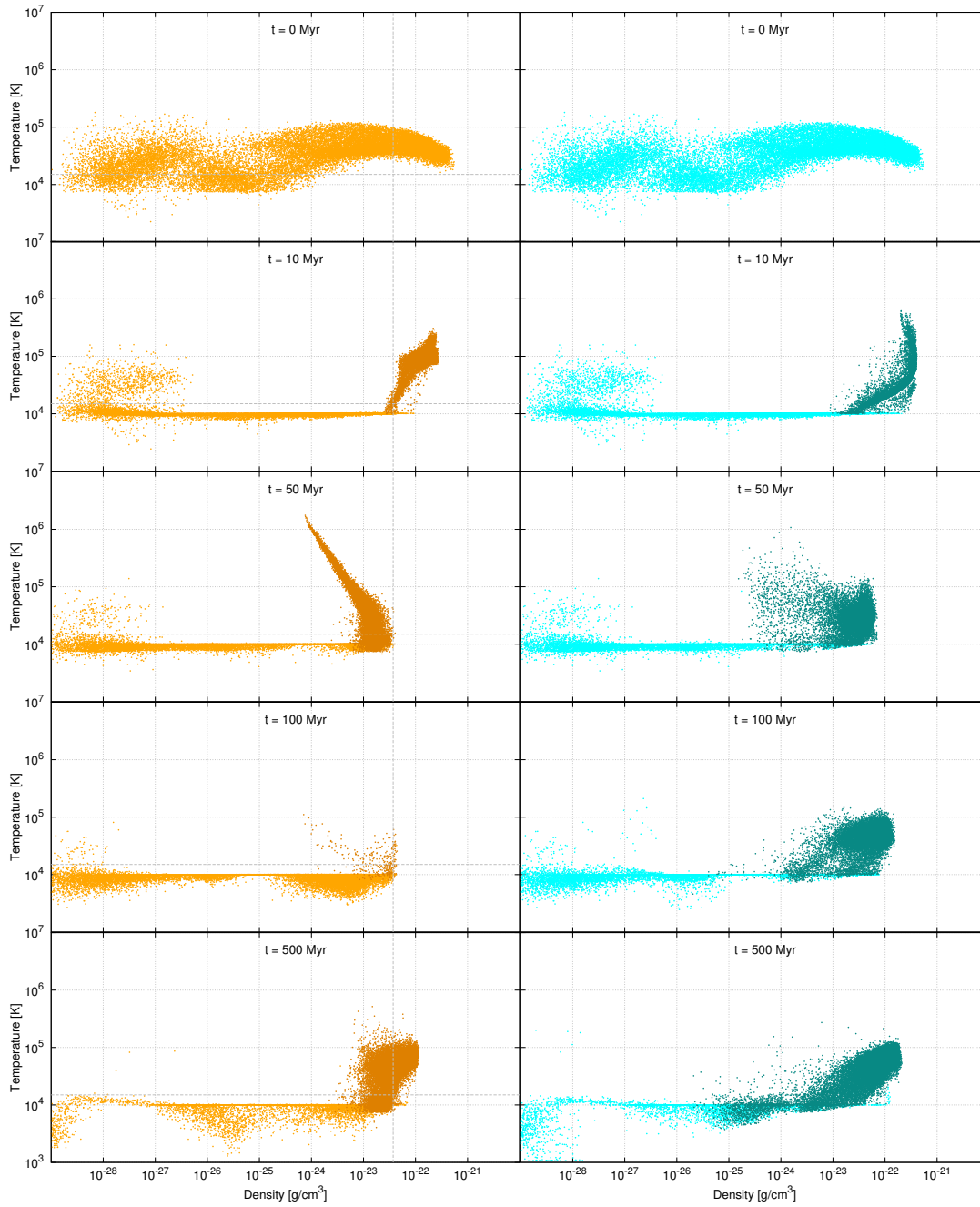


Figure 7.5: Phase-space diagram of gas particles for simulations carried out using the stochastic SF recipe (left column) and the self-regulated approach (right column). Gas particles with disabled cooling are illustrated with slightly darker colors. Density and temperature thresholds are drawn with grey dashed lines in the left column at $3.71 \times 10^{-23} \text{ g cm}^{-3}$ and $1.5 \times 10^4 \text{ K}$ respectively. The simulation times are 0, 10, 50, 100, and 500 Myr from top to bottom.

7.3 Total Energy and Angular Momentum

The total internal energy of gas is about 30% higher when the self-regulated SF recipe is used (see fig 7.6). In this case, the average temperature for the central region has a maximum at approximately 8000 K, whereas for the stochastic scheme, it is at around 6000 K, which explains this difference of about 30%.

It is also interesting to examine the total angular momentum for those simulations. From fig 7.7, one can find first of all, that the angular momentum is very well conserved in both runs. The total average values are $1.25 \times 10^{11} \pm 1.71 \times 10^8 M_{\odot} \text{ kpc}^2 \text{ Gyr}^{-1}$ for the stochastic and $(1.25 \times 10^{11} \pm 1.18 \times 10^8) M_{\odot} \text{ kpc}^2 \text{ Gyr}^{-1}$ for the self regulated recipe. The error in angular momentum is in all cases less than 0.01 %. The angular momentum of the stellar component, must be larger for the stochastic SF scheme, because more gas mass is transformed into stars. Therefore, the angular momentum of gas has to be below the comparison run. There is apparently some transfer of angular momentum between dark matter and baryonic mass. This well-known phenomenon in galaxy simulations, is more apparent for the stochastic run and connected to the larger number of N-body particles, due to the higher SFR. The rotational velocity of the galaxy is approximately between 60 to 70 km s^{-1} , as can be seen in fig. 7.8. The value at time 0 is distinctly below that at around 40 km s^{-1} , which is a result of angular momentum conservation after cooling starts.

7.4 Galaxy Shape

In this section, a more detailed view is taken on the overall shape of the simulated dwarf galaxy. The following figures show a direct comparison of the gas density distribution for the stochastic SF recipe in the first rows and the self-regulated recipe in the second rows. Figure 7.9 - 7.16 show a thin cut through the galaxy with the size of 2 times the smoothing length for each particle. These pictures are created, using *Splash*, a visualization tool for SPH-data, developed by James Price (Price, 2007). Fig. 7.9 shows a detailed view on the initial starburst, after turning on cooling and SF. In both cases the burst is strong enough to produce a ring-like structure, although it is more prominent when the stochastic SF recipe is used. Fig. 7.10, which shows a cut through the xz-plane, reveals a stronger outflow in vertical direction. The reason for that is the less strong concentration of SF in the disc plane, compared to the stochastic SF scheme, as we will see in section 7.5. The first panels in that figure show shock waves travelling through the surrounding medium, caused by the strong starburst. It is also interesting to note

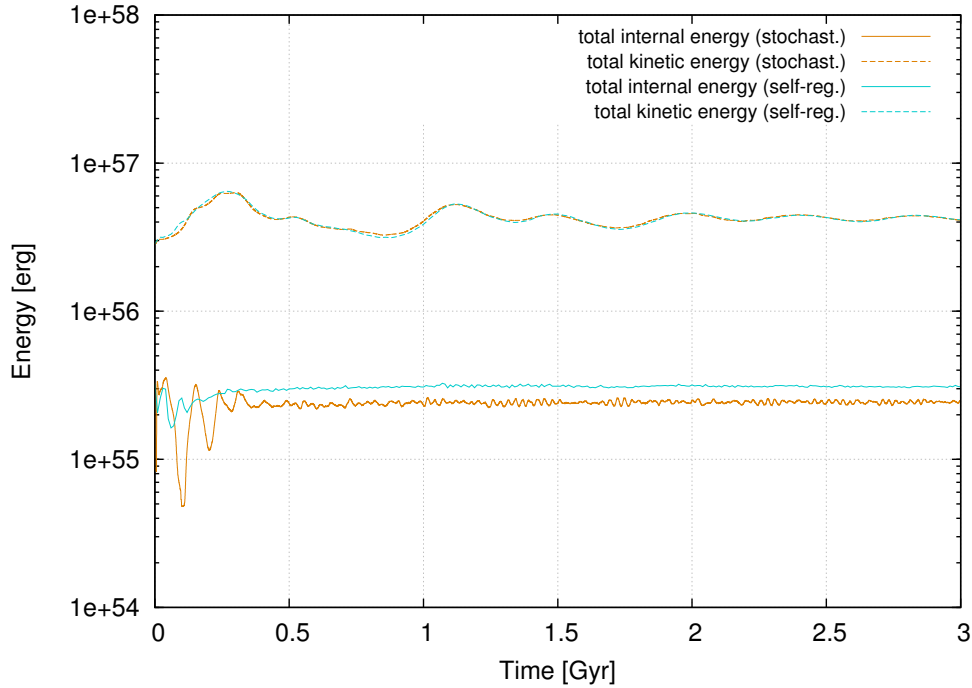


Figure 7.6: Comparison of the total kinetic (dashed lines) and the total internal energy (solid lines) as a function of time. Orange lines indicate the stochastic scheme. Turquoise lines show results from the self-regulated SF recipe.

that it obviously takes longer for the stochastic recipe to vault back to equilibrium, as can be seen also in fig. 7.11 and 7.12 third panel, where the compression of the reinfalling material triggers new starbursts resulting in further oscillations during this early phase. After the first few hundred Myr, the galaxy shape is relatively similar in both cases. Interestingly, this dwarf galaxy seems to form spiral structures in both cases. Most of the time two arm structures are visible, almost like in a barred spiral type galaxy, but the density along those arms is about 1000 times smaller compared to the central region, which has a diameter of ~ 4 kpc. Therefore, the density in those arms is way too low to make SF possible. Dwarf galaxies with spiral structures seem to be extremely rare. Nevertheless, there had been some investigations concerning disc and spiral features in dwarf elliptical galaxies of the Virgo cluster showing comparable features, although they have been observed as stellar component (Lisker et al., 2006, 2009). A dwarf galaxy with very similar physical properties showing extended spiral arms with only extremely little SF in those outer regions would be for instance NGC 2915 (Elson et al., 2010, 2011; Bruzese et al., 2015; Meurer et al., 2015). However, this particular example does not show a steep rotation curve like the presented model dwarf galaxy.

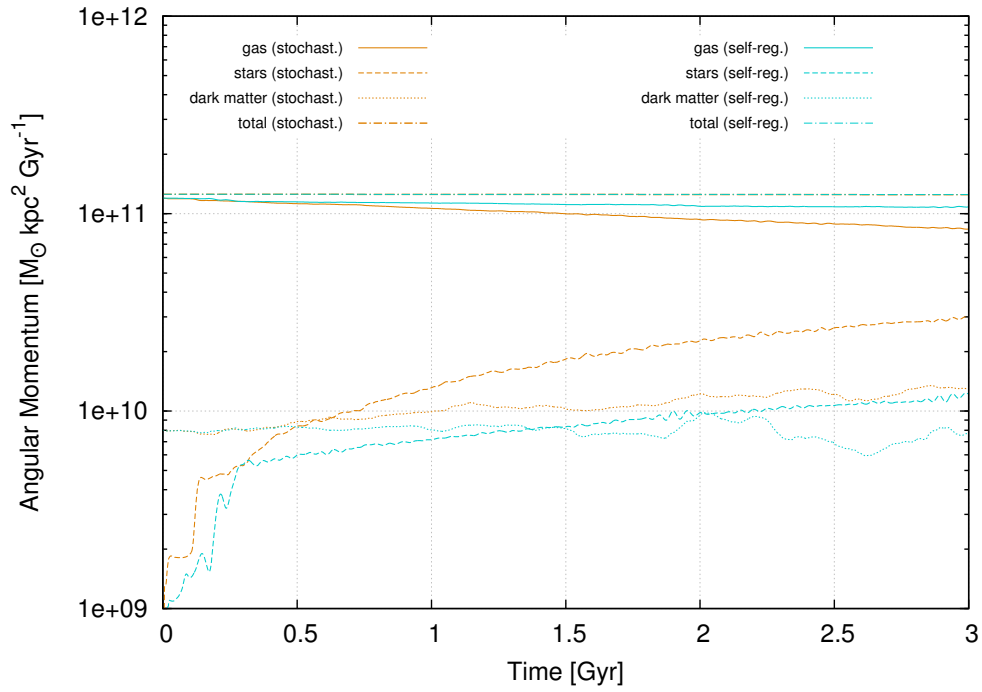


Figure 7.7: Angular momentum evolution of gas (solid lines), stars (dashed lines) and dark matter (dotted lines) for the self-regulated (turquoise) and the stochastic (orange) SF recipe. The total angular momenta are indicated by dotted-dashed lines. Note that the total angular momentum has the same almost constant value in both runs.

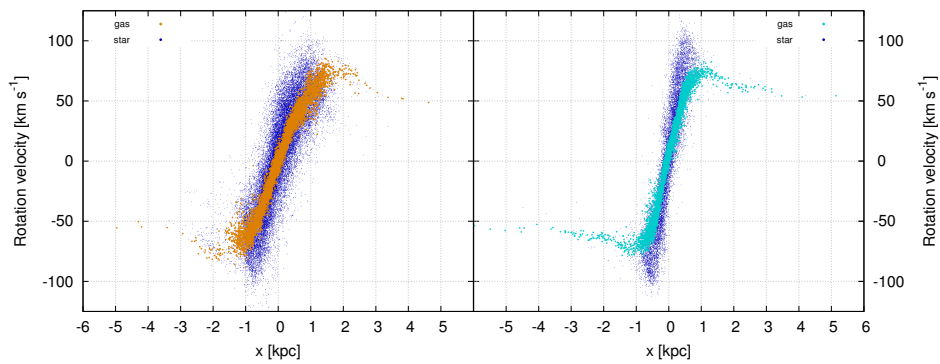


Figure 7.8: Rotation velocity as a function of x position for particles within a cuboid-shaped domain of $|z| < 0.25$ kpc and $|y| < 0.25$ kpc along the x-axis. gas particles are represented by orange dots for the stochastic SF recipe (left panel) and turquoise dots for the self-regulated SF recipe (right panel). Small blue dots show the stellar component. The simulation time is 1 Gyr.

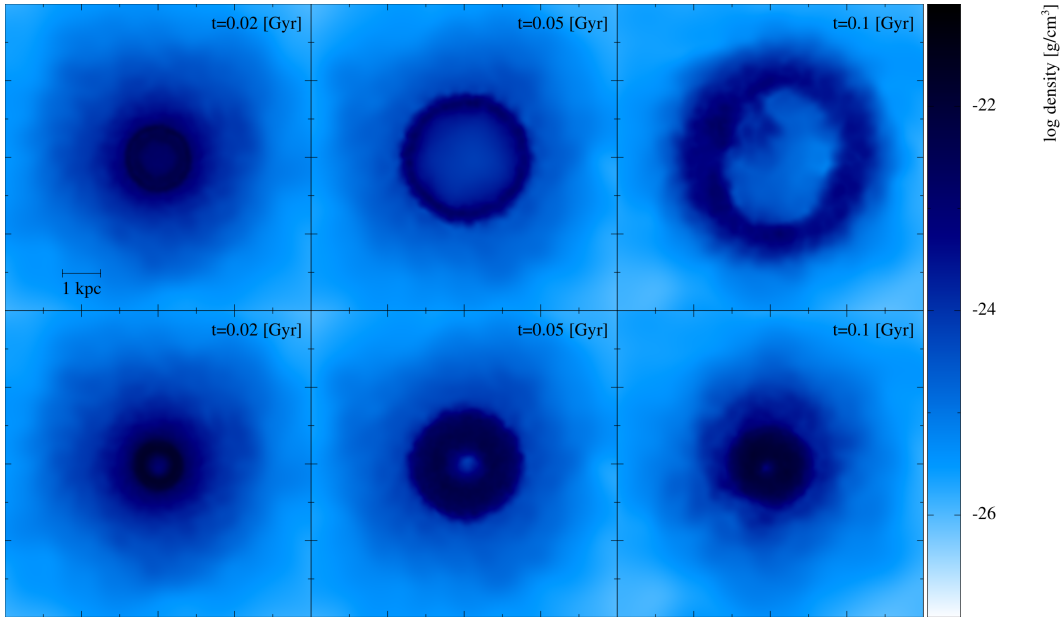


Figure 7.9: Face on view on the simulated dwarf galaxy at 20, 50 and 100 Myr simulation time (across). The plot shows the density distribution with the according color scale in the right-hand strip. Upper row: Stochastic SF recipe, lower row: Self-regulated SF recipe. Each panel has a side length of 8 kpc.

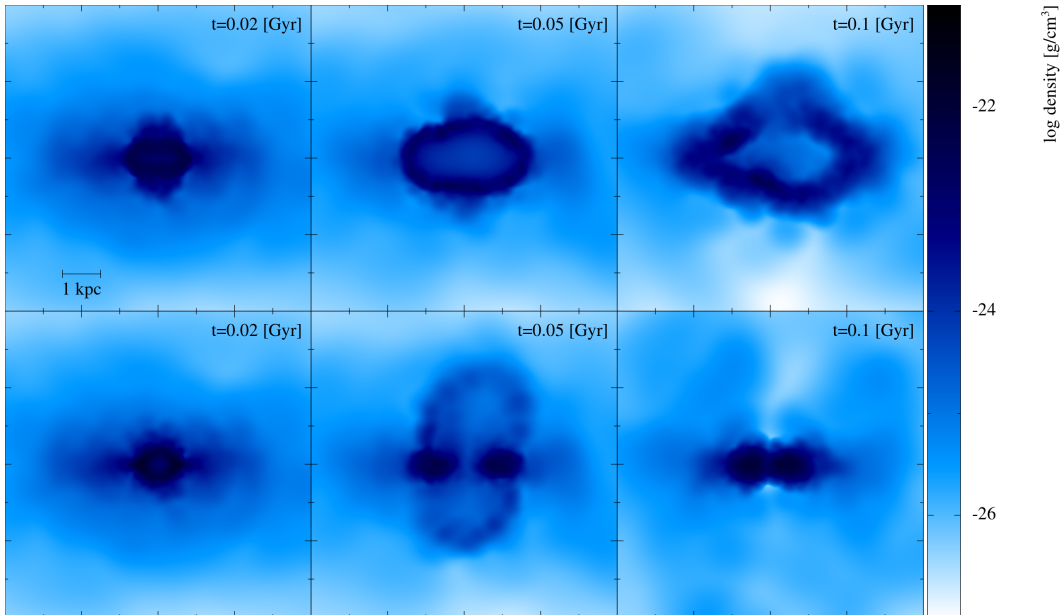


Figure 7.10: As in figure 7.9 but for an edge on view.

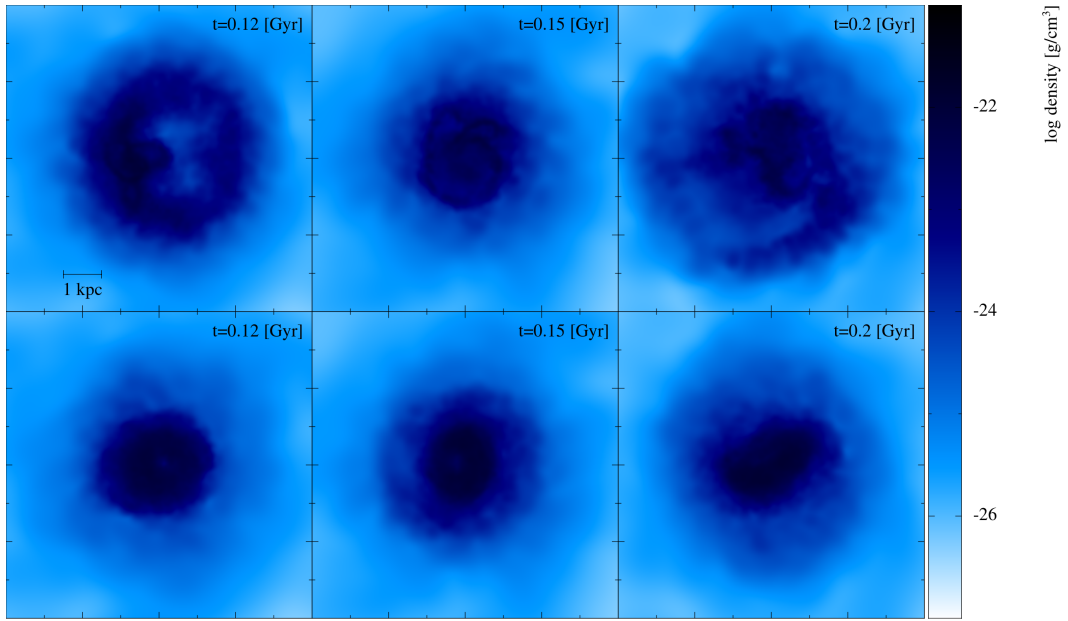


Figure 7.11: As in figure 7.9 but for simulation times of 120, 150 and 200 Myr.

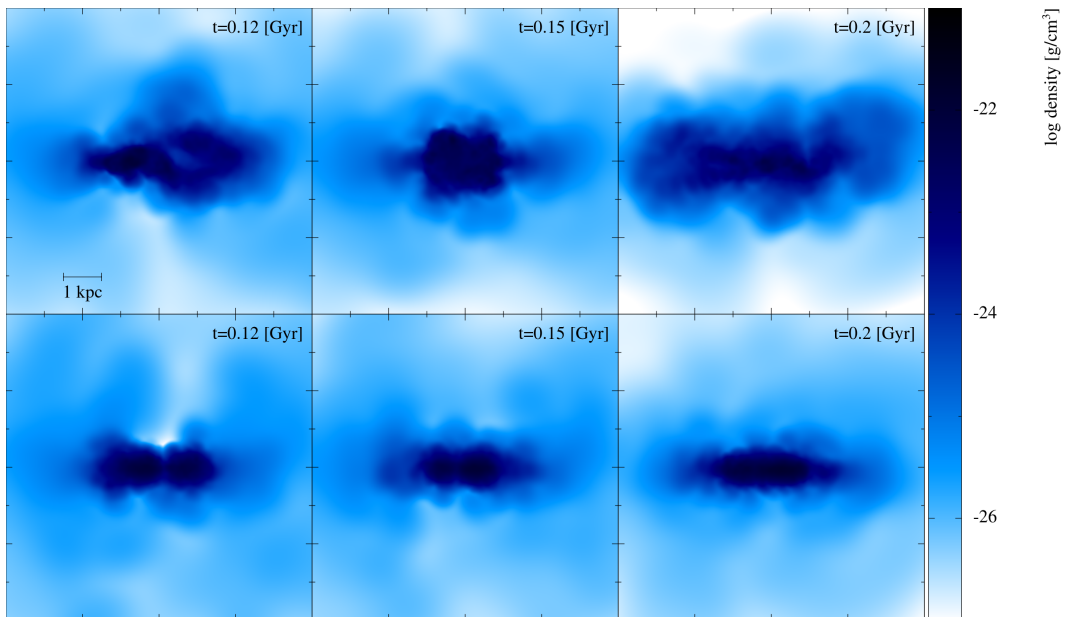


Figure 7.12: As in figure 7.10 but for simulation times of 120, 150 and 200 Myr.

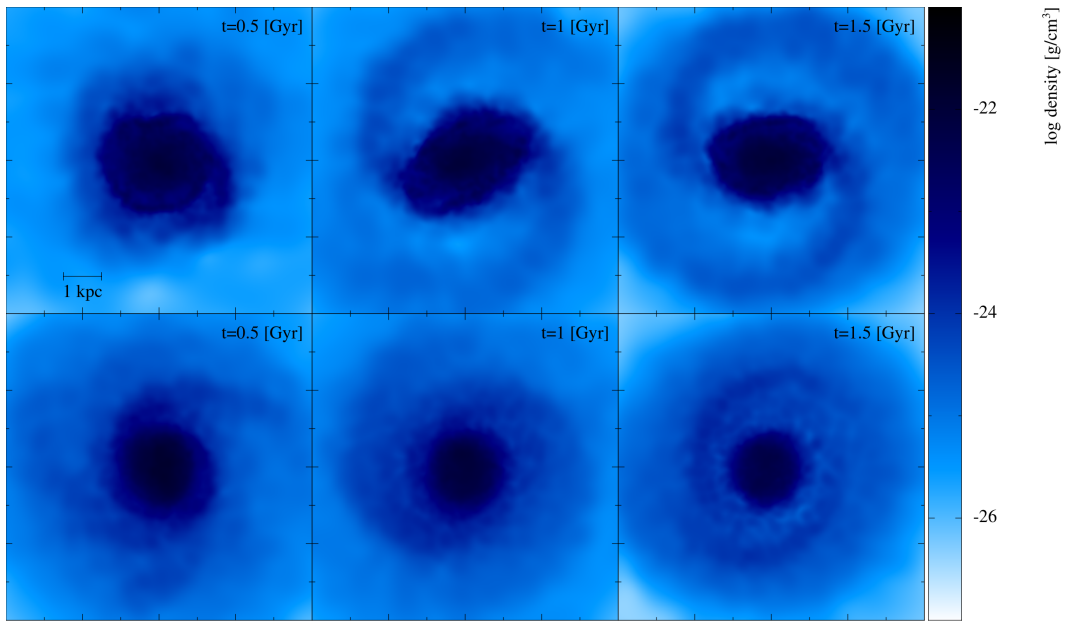


Figure 7.13: As in figure 7.9 but for simulation times of 500, 1000 and 1500 Myr.

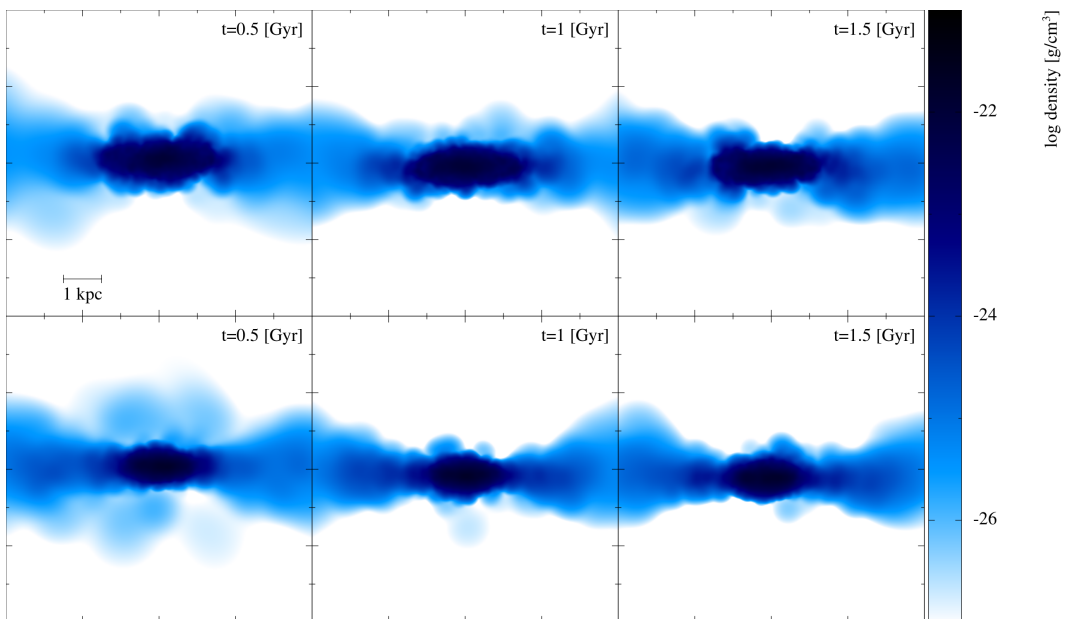


Figure 7.14: As in figure 7.10 but for simulation times of 500, 1000 and 1500 Myr.

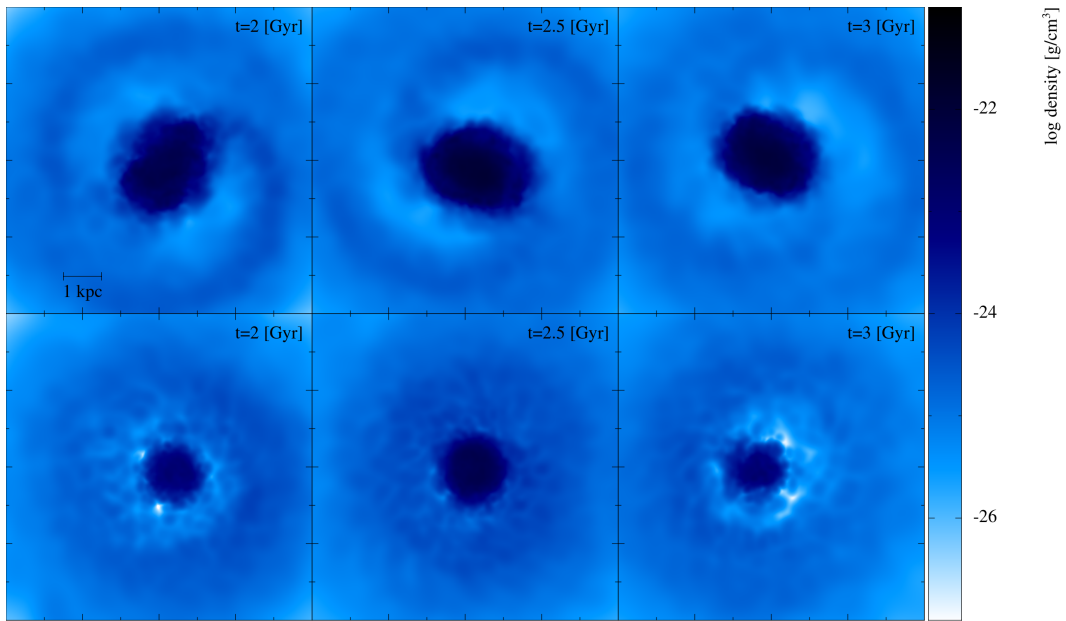


Figure 7.15: As in figure 7.9 but for simulation times of 2000, 2500 and 3000 Myr.

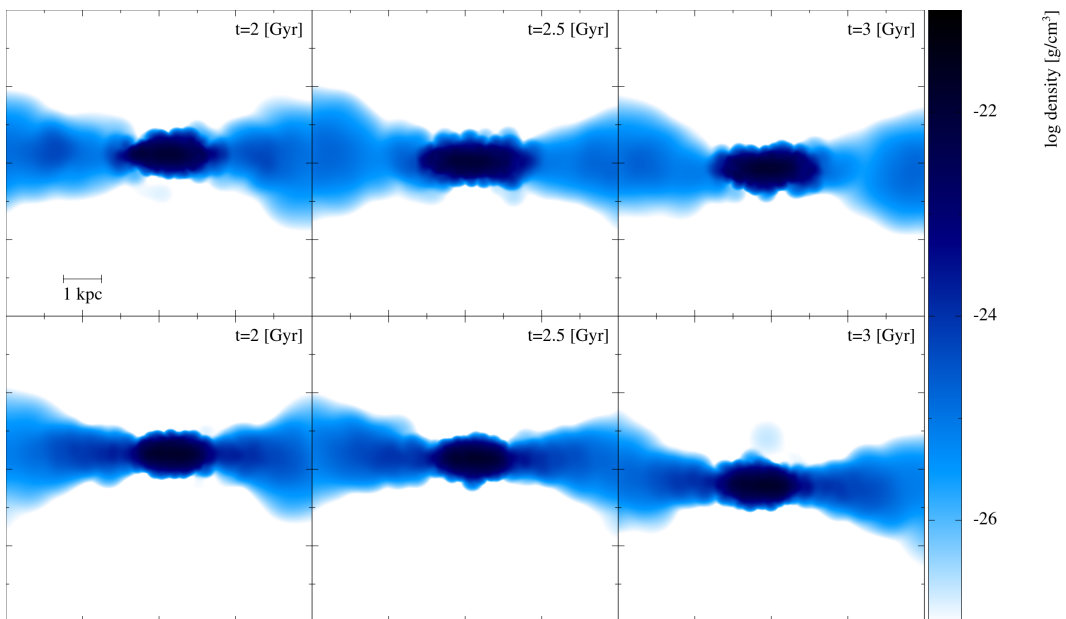


Figure 7.16: As in figure 7.10 but for simulation times of 2000, 2500 and 3000 Myr.

7.5 Star-Formation Rates

In this subsection the properties of SF for both cases are compared and discussed in further detail. A comparison of the SFRs for both reference runs have already been presented in figure 7.2, where strong fluctuations in the SFR are visible, especially for the self-regulated run. These periodically occurring maxima and minima in the SFR seem to be distributed evenly over the whole simulation time, not only shortly after the initial starburst, which indicates that they are not necessarily connected to the explosion in the beginning and the following re-relaxation of the system and therefore must be powered constantly during the simulation. In order to understand which processes are responsible for this phenomenon, it is important to quantify these oscillations by measuring their frequencies. At first, the SFR must be shifted down to oscillate about zero. This makes it possible to apply a simple fast fourier transformation (FFT), creating a frequency spectrum from which we should be able to get a better overview on possible oscillation processes. For the transformation to normalize the SFR around the zero point, a simple subtraction of the average in logarithmic scale was used (eq. 7.1)

$$\log(\text{SFR}_{norm,i}) = \log(\text{SFR}_i) - \log\left(\frac{\sum_{j=1}^{N_{bin}} \text{SFR}_j}{N_{bin}}\right), \quad \text{SFR}_j \neq 0, \quad (7.1)$$

where SFR_i is the SFR within time bin i and N_{bin} is the number of all bins. As expected, the frequency spectra do not show homogeneously distributed noise, but signals the prominence of different oscillation frequencies (fig. 7.17 and 7.18).

The FFT of the SFR for the stochastic recipe shows a region in fig. 7.17 with low-frequency signals between 8 and 16 Gyr^{-1} . A relative high maximum of this almost continuous feature lies at 11.7 Gyr^{-1} , which would give a period of 86.2 Myr. There is also a very clear distinct peak at a frequency of 37.08 Gyr^{-1} . This corresponds to one peak in the SFR every 27 Myr approximately.

Another interesting finding is the occurrence of starbursts in both reference runs, as we will see later. In those simulations, SF is not evenly distributed over the whole galactic disc but there are dense gas clumps frequently forming, which can produce up to a few hundred stellar particles in less than 10 Myr. If the entire galactic disc would constantly form stars at such a high rate, the total gas mass would probably be consumed within the first Gyr. The resulting clumps of young stellar particles are easily distinguishable from their surroundings and from the weak and homogeneously scattered SF. It is possible to examine these structures by constraining the simulation results for a small region around them at a specific

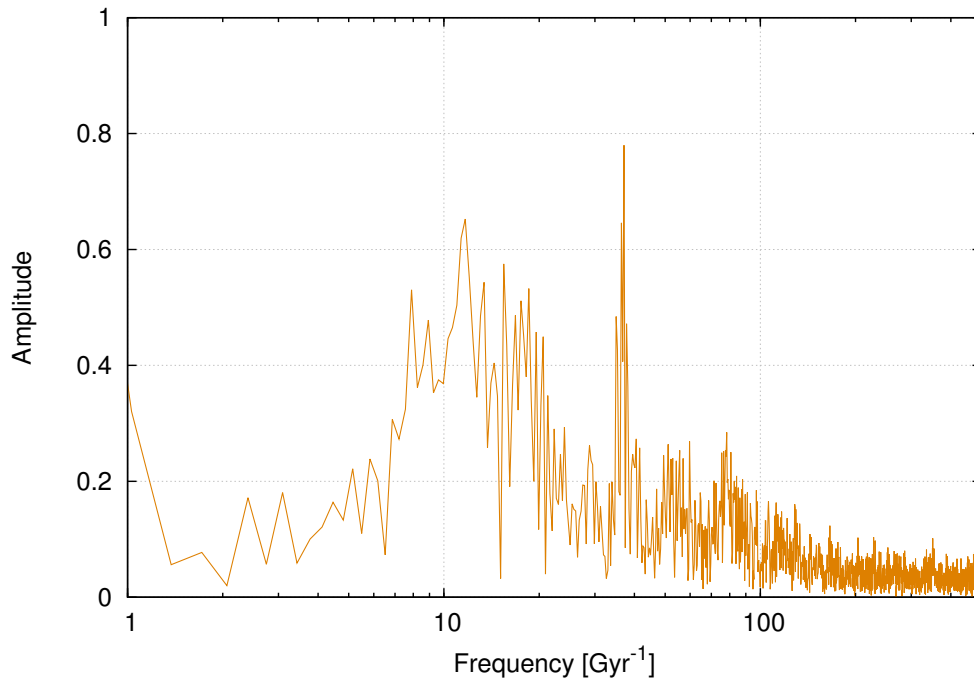


Figure 7.17: Frequency spectrum of the SFR for the stochastic SF recipe. Note the area between 8 and 16 Gyr^{-1} with many clear peaks and a very prominent maximum at 37 Gyr^{-1} .

time. The stellar age of star particles residing within that zone can then be used to calculate the SFR for such individual clumps. Table 7.2 lists a few of those star-burst regions and their physical properties. They produce stellar masses between 10^5 and $10^6 M_{\odot}$, which give significant contributions to the total SFR and are therefore one of the reasons for the strong fluctuations. The SFRs of the six example regions from table 7.2 can be found in fig. 7.19 or in fig. 7.20 for the self-regulated recipe.

The frequency spectrum for the self-regulated SF recipe (fig. 7.18) is not very different from the stochastic one, which was discussed above. Here, the low-frequency signals are much more prominent than peaks in the high-frequency range. There are multiple peaks between 14 and 20 Gyr^{-1} at 14.1, 15.4, 16.5, 17.9 and 19.6, to name the strongest of them. The maximum value is the first one with 14.1 Gyr^{-1} corresponding to a period of approximately 70.9 Myr. This is not far from the low-frequency signal of 86.2 Myr of the other reference run, indicating that similar physical processes might be the cause for this interesting finding. Amplitudes at higher frequencies are much weaker, but there are at least two conspicuous peaks at 36.3 and 33.8 Gyr^{-1} , which would correspond to periods

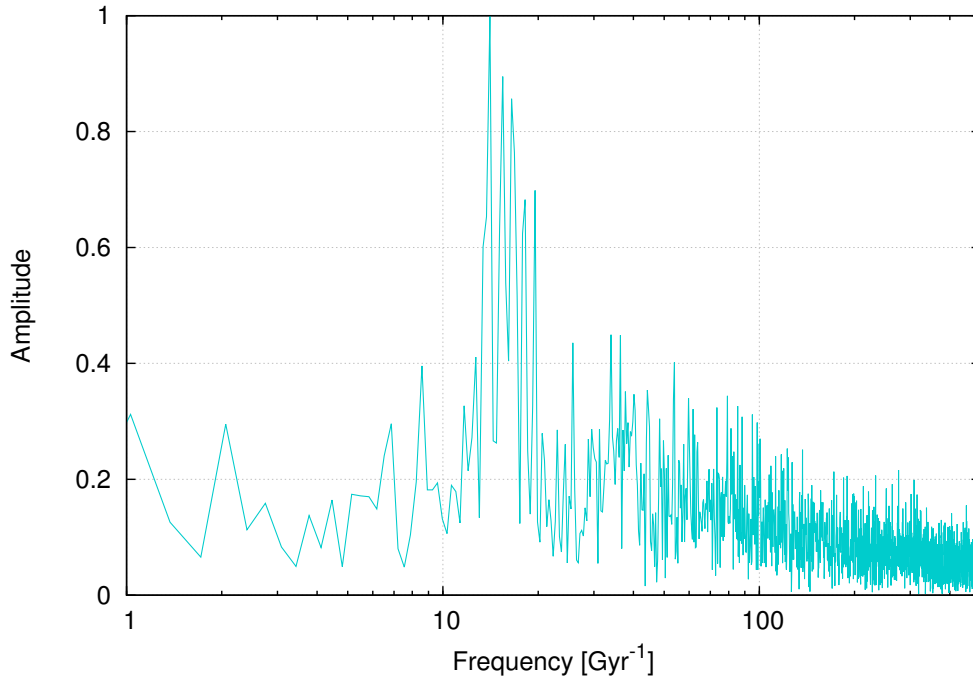


Figure 7.18: Frequency spectrum of the SFR for the self-regulated SF recipe. A major peak can be found at 14.1 Gyr^{-1} and secondary peaks at 15.4 , 16.5 , 17.9 and 19.6 Gyr^{-1} .

of 27.5 and 29.6 Myr.

Additionally, the behaviour of the average density and temperature for the main part of the galaxy within a 1 kpc radius is very similar in terms of periodic fluctuations with comparable temporal separations. One difference is that density and temperature are both higher in the beginning and stay more constant during the simulation, whereas for the case of the SF recipe, those average values are slowly rising. Interesting is the fact, that the self-regulated recipe shows starburst regions with matchable size and SFRs. This phenomenon seems to be independent from the used SF recipe and therefore should be caused by the behaviour of gas and stellar particles. Both runs produce SF fluctuations with frequencies in the order of 12 - 14 Gyr^{-1} . This clearly effects the density and temperature and therefore the total behaviour of the system. One can find comparable numbers of smaller and larger maxima in the density evolution (fig. 7.21, 7.22) within every Gyr like in the SFR.

The free-fall time scale of the galaxy in run sto01, $\tau_{ff} = \sqrt{3\pi/32G\rho}$ is (14.3 ± 12) Myr and the cooling time (5.1) is approximately between 5 and 80 Myr, with relatively high uncertainty because of the strong varying cooling rate. These are average values for the innermost 1 kpc radius of the system and the timescales

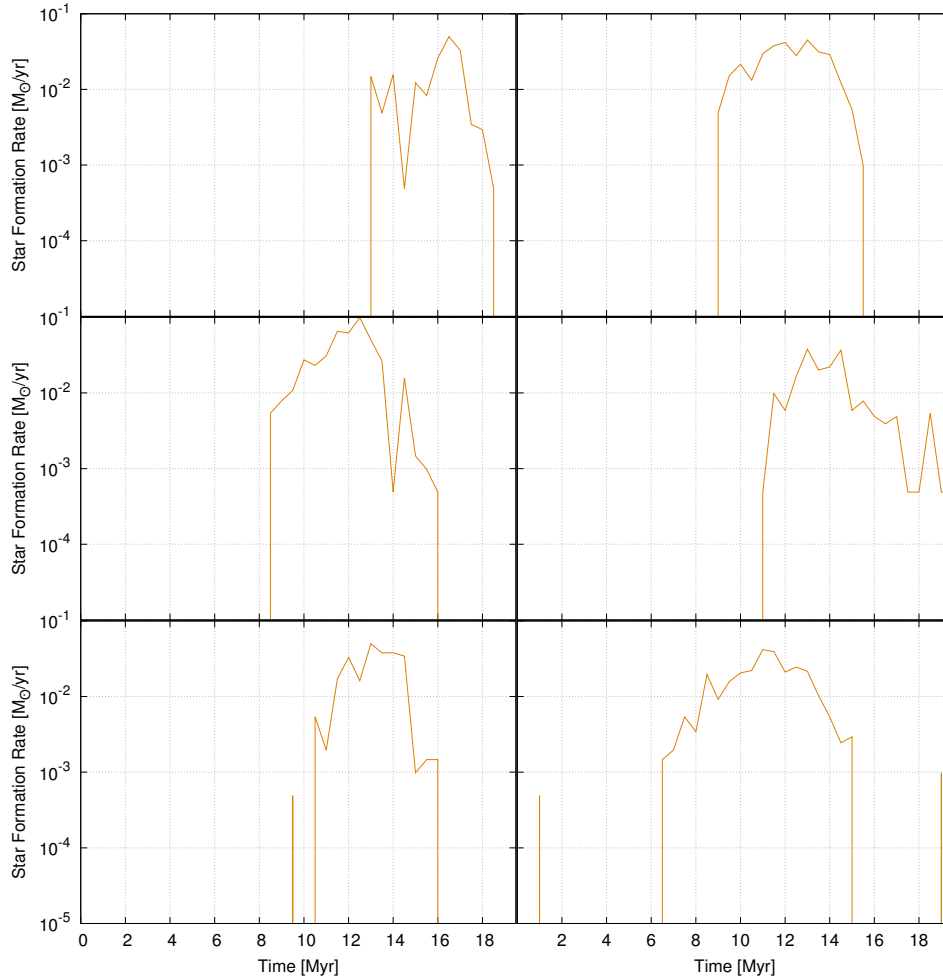


Figure 7.19: Examples for 6 different starburst regions identified in run sto01 from table 7.2 (from left to right and top to bottom). The SFRs are calculated for a small spatial selection during a 20 Myr time window.

might be linked to the short periodic star-formation oscillations. As mentioned before, in both cases one can find regular density variations with similar time intervals. The relatively strong starbursts seem to have much influence on the inner 2 kpc of the galaxy. They can heat up large parts of the system and enable cooling for surrounding gas particles. Here, the cooling shut-off time should play a major role for the further development. Although during the time in which type II SNe are occurring for one stellar population, lasting about 45 Myr, surrounding gas particles are not allowed to cool any more, the neighbouring SPH particles are continuously replaced by other particles. This happens due to differential rotation, scattering and the fact that stellar particles do not gain hydro forces, which means

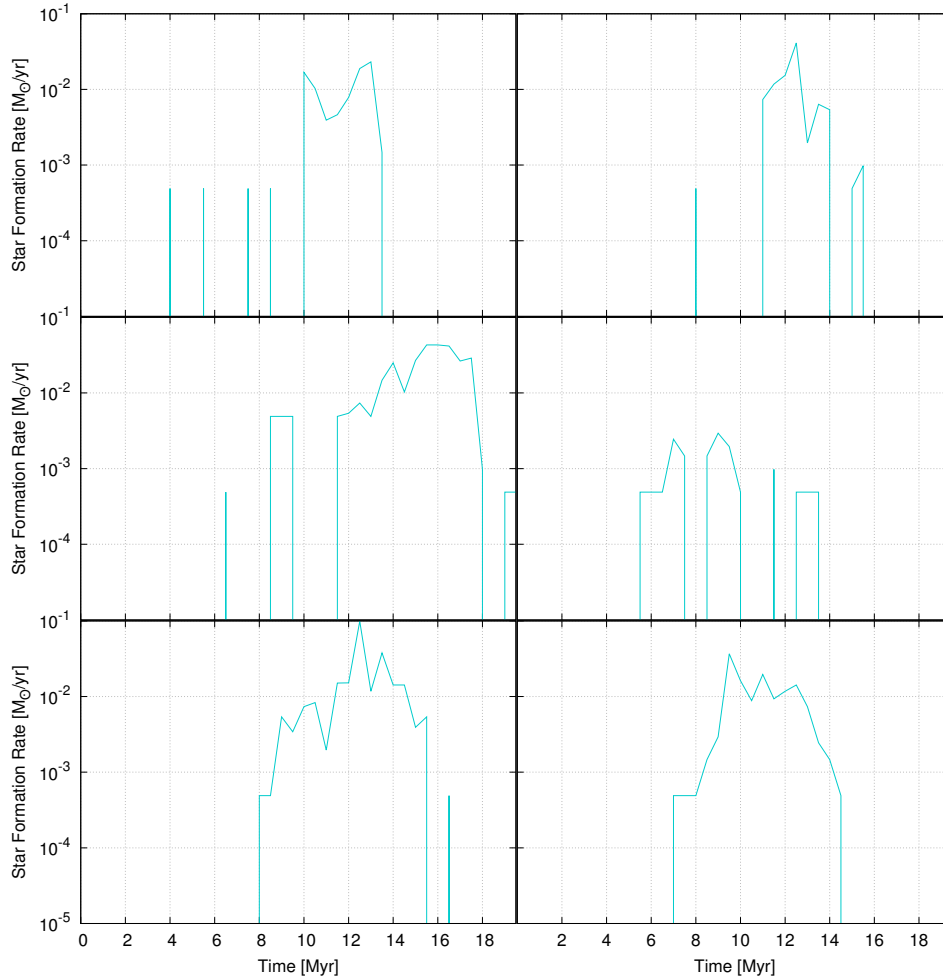


Figure 7.20: Examples for 6 different starburst regions identified in run sr01 from table 7.3 (from left to right and top to bottom). The SFRs are calculated for a small spatial selection during a 20 Myr time window.

that a gas particle which gets out of reach of the young stellar population will continue cooling after just 1 Myr for these simulations. A significant amount of gas mass can have disabled cooling within the major part of the dwarf galaxy. A few such starbursts within a short time range can effectively quench SF. Because the free-fall and the cooling times both lie in the order of a few tens of Myr the system should be able to recover and increase the probability for further SF again within such a period of time.

Another mentionable finding, which might be one cause for the long periodic oscillations in the SFR is, that the starburst regions are very often distributed symmetrically on both sides of the galaxy, especially in run sto01, where a bar

t_{sim} [Myr]	x [kpc]	y [kpc]	z [kpc]	r [kpc]	M_{gas} [M_{\odot}]	M_{\star} [M_{\odot}]	N_{\star}	SFR_{max} [$M_{\odot} \text{ yr}^{-1}$]	t_{burst} [Myr]
762	-0.35	-0.05	-0.08	0.15	1.64×10^7	3.801×10^5	90	5.0×10^{-2}	5.5
923	-0.79	-0.32	-0.05	0.15	7.73×10^6	5.225×10^5	125	4.5×10^{-2}	6.5
980	-0.83	0.56	-0.05	0.15	6.00×10^6	7.220×10^5	173	1.0×10^{-1}	7.5
1149	-0.67	0.7	-0.08	0.15	9.45×10^6	4.840×10^5	115	4.0×10^{-2}	9
1317	-0.16	-0.37	0.1	0.15	2.06×10^7	4.691×10^5	112	4.5×10^{-2}	5.5
2003	-0.45	-0.38	0.2	0.25	5.14×10^7	1.918×10^6	461	4.0×10^{-2}	8.5

Table 7.2: Specifications of 6 different starburst regions from run sto01 with the stochastic SF recipe. t_{sim} is the simulation time in Myr, x , y and z are the position coordinates of the center of the SF region in kpc. M_{gas} and M_{\star} give the total values of gas and stellar mass respectively, within a radius r radius around that central point. The number of stellar particles is given by N_{\star} , followed by the maximum SFR and the duration of of the starburst in Myr.

t_{sim} [Myr]	x [kpc]	y [kpc]	z [kpc]	r [kpc]	M_{gas} [M_{\odot}]	M_{\star} [M_{\odot}]	N_{\star}	SFR_{max} [$M_{\odot} \text{ yr}^{-1}$]	t_{burst} [Myr]
282	0.55	0.05	-0.10	0.15	2.30×10^7	5.38×10^5	100	3.0×10^{-2}	3.5
506	0.40	0.23	0.08	0.15	1.90×10^7	5.00×10^5	98	4.0×10^{-2}	3.0
1005	0.30	0.40	-0.10	0.3	1.17×10^8	5.65×10^5	162	5.0×10^{-2}	6.5
1277	0.38	0.18	0.18	0.15	3.22×10^7	1.75×10^5	30	3.0×10^{-2}	8.0
1604	-0.45	-0.15	-0.28	0.15	2.40×10^7	1.50×10^5	98	1.0×10^{-1}	7.5
2126	-0.17	0.16	0.0	0.15	2.59×10^7	1.93×10^6	211	3.5×10^{-2}	7.5

Table 7.3: Specifications of 6 different starburst regions from run sr01 with the self-regulated SF recipe. t_{sim} is the simulation time in Myr, x , y and z are the position coordinates of the center of the star forming region in kpc. M_{gas} and M_{\star} give the total values of gas and stellar mass respectively, within a radius r around that central point. The number of stellar particles is given by N_{\star} , followed by the maximum SFR and the duration of of the starburst in Myr.

feature within the central part of the galaxy is very clearly visible. Often, one can find starbursts right at both tips of the bar. Furthermore, in fig. 7.8 one can see a dominant part of the galaxy's center, for both SF recipes showing solid-body rotation up to approximately 1 kpc. At this radius where the solid body rotation ends, and the rotational velocity is $\sim 75 \text{ km s}^{-1}$, the period of circulation is around 82 Myr. In case of the self-regulated recipe, the part showing solid body rotation has a smaller radius of $\sim 0.75 \text{ kpc}$ and a rotational speed at the edge of $\sim 70 \text{ km s}^{-1}$, which would give a rotation period around 67 Myr. And indeed, as shown above, the low-frequency peak in the frequency spectrum of the SFR in this case corresponds to a smaller period compared to sto01, namely 70.9 Myr. Because of this evidence it is reasonable to assume, that there might be some causal relationship between the rotation period of the solid body part and the periodic occurrence

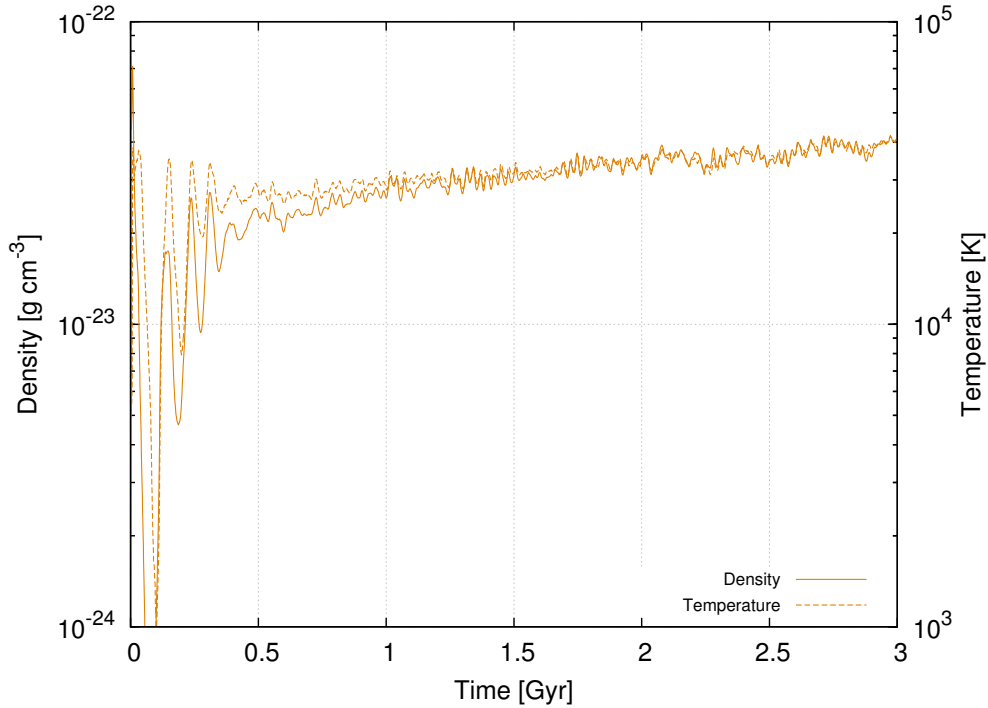


Figure 7.21: Time evolution for average density (solid line) and temperature (dashed line) of SPH particles within the innermost 1 kpc radius of the system. The stochastic SF recipe was used.

of starbursts. Probably, periodic perturbations of the bar can cause this phenomenon, which is very interesting, because there is much discord in literature, whether such starburst phenomena are triggered by internal processes or external mechanisms like tidal perturbations (Noguchi, 1988), mergers (Bekki, 2008), and cold gas accretion (Silk et al., 1987; Hensler, 2010). Most authors suggest that the latter is the more probable case. In Lelli et al. (2014), 18 nearby starburst dwarf galaxies have been investigated and most of them had at least one possible perturber within a distance of $\lesssim 200$ kpc and show relatively strong asymmetries. Nevertheless, there is also good evidence of internal mechanisms, which can cause starbursts. For instance in spiral galaxies, circumnuclear starbursts are believed to be associated with stellar bars (Kennicutt, 1998b; Kormendy and Kennicutt, 2004; McQuinn et al., 2015).

It is also worthwhile to investigate, why there is much more gas mass transformed into stars during the first 100 Myr of simulation sr01 compared to sto01. The reason for this is, that the SF recipe of Koeppen et al. (1995) is able to trigger SF due to strong shocks with the used parameters as demonstrated below. From equation 4.20 we can calculate the density a gas particle needs to have to reach

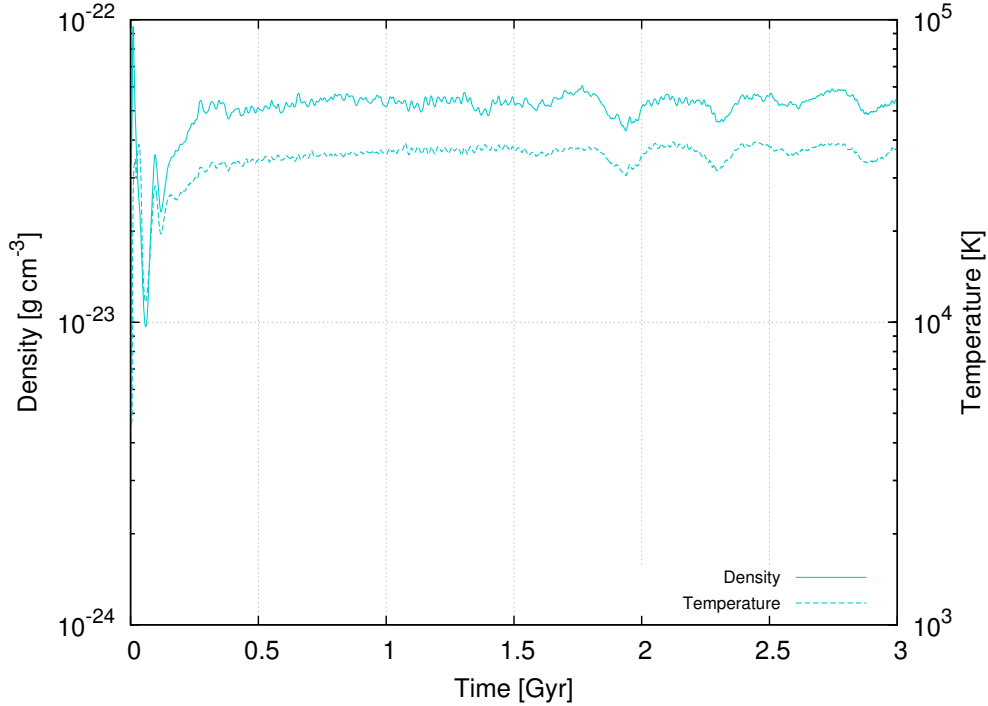


Figure 7.22: Time evolution for average density (solid line) and temperature (dashed line) of SPH particles within the innermost 1 kpc radius of the system. The self-regulated SF recipe was used.

the minimum mass limit of $m_{\star, \min} = 1000 M_{\odot}$.

$$\rho = \sqrt{\frac{m_{\star}}{C_2 \rho^2 e^{-\frac{T}{T_s}} \frac{4\pi}{3} h^3 t_{\text{form}}}} \quad (7.2)$$

For a temperature of $T = 10^4$ K and a typical smoothing length of 0.2 kpc, the gas particle would need a density of $2.34 \times 10^{-23} \text{g cm}^{-3}$. In all simulations, $C_2 = 2.575 \times 10^8 \text{cm}^3 / (\text{g s})$, $T_s = 1000$ K, and the formation time $t_{\text{form}} = 10$ Myr are used. This typical density limit can be reached on higher radii easily during the shock wave travelling through the galaxy, originating from the strong initial starburst, which subsequently leads to the creation of a ring-like structure with strong SF, further accelerating the surrounding gas and heating up material (see fig. 7.23 left panel). This can also be observed a few Myr later in vertical direction, where the compressed material suddenly starts to form hundreds of star particles (see right panel in fig. 7.23). The vertically offset SF ruptures the surrounding gas shell, allowing the hot and dense particles to be ejected from the center. This process is in contrast to run sto01, where the expanding material is not able to trigger further SF and results in a faster cooling of gas, which falls

back and creates much stronger secondary starbursts, because this material comes in more concentrated. Additionally, most of the gas can not penetrate through the cooler envelope, keeping it trapped near the central region.

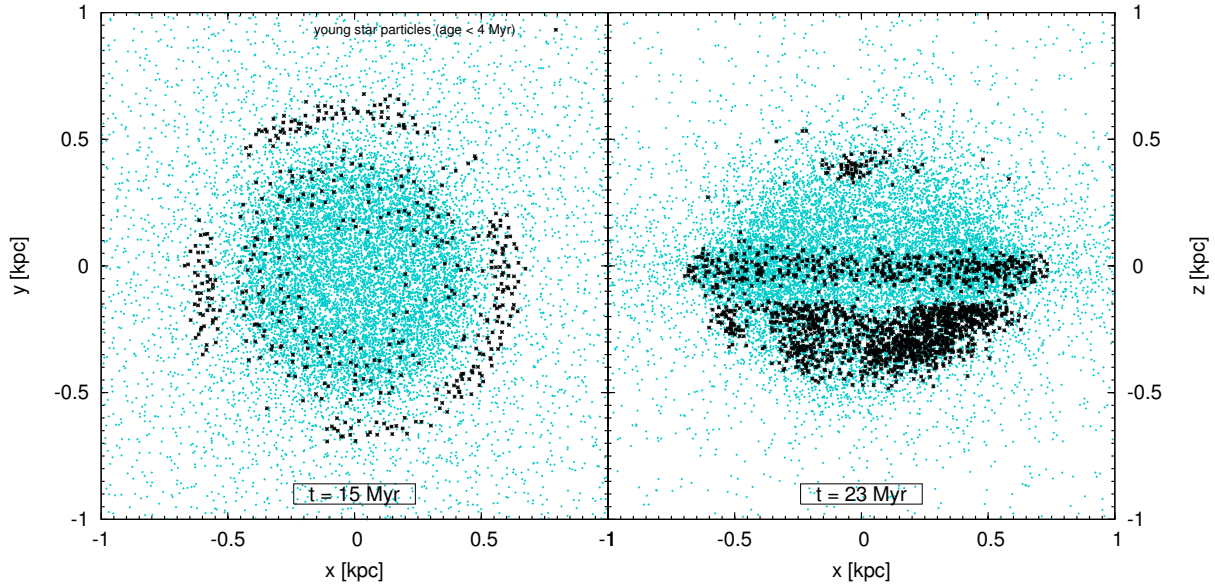


Figure 7.23: *Left*: Face on view on the central region after the first 15 Myr of run sr01. Gas particles are indicated by turquoise dots. Black stars show young stellar populations with age < 4 Myr. *Right*: Edge on view after the first 23 Myr.

7.6 Chemical Evolution

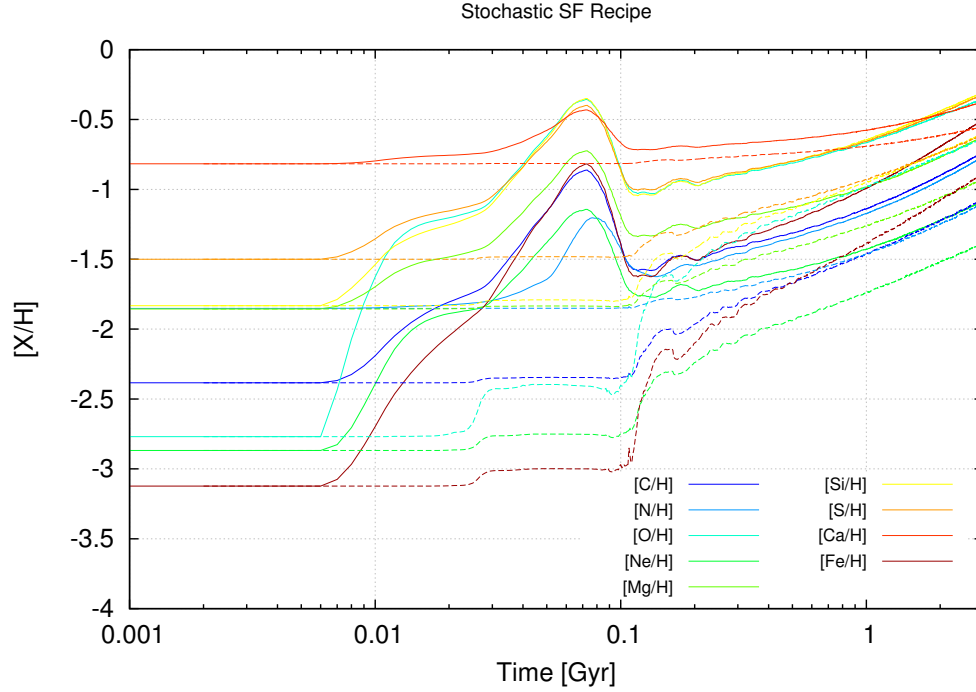


Figure 7.24: Evolution of the chemical abundances for 9 different elements using the stochastic star-formation recipe. Solid lines indicate compositions of gas, and dashed lines of the stellar component. Values are averaged for the innermost 2.5 kpc radius of the dwarf galaxy.

The chemical enrichment of the galactic system due to feedback processes described in chapter 4.3, has very strong effects, mostly on cooling, therefore, also on SF and can significantly change the behaviour of the whole system. In figures 7.24 and 7.25, chemical abundances relative to the sun are presented on a logarithmic timescale for both SF recipes during the total simulation time of 3 Gyr. The chemical abundances $[X/H]$ of element X should be understood as the fraction between the number density of this element relative to hydrogen on a logarithmic scale compared to solar values. Unless we only consider fractions with solar abundances, the particle masses would cancel each other out and we can simply compare mass fractions:

$$[X/H] = \log\left(\frac{m_X}{m_H}\right) - \log\left(\frac{m_{X,\odot}}{m_{H,\odot}}\right) \quad (7.3)$$

It is relevant to note, that once the first type II SNe emerge, the medium gets enriched with a very high amount of oxygen relative to other elements. This

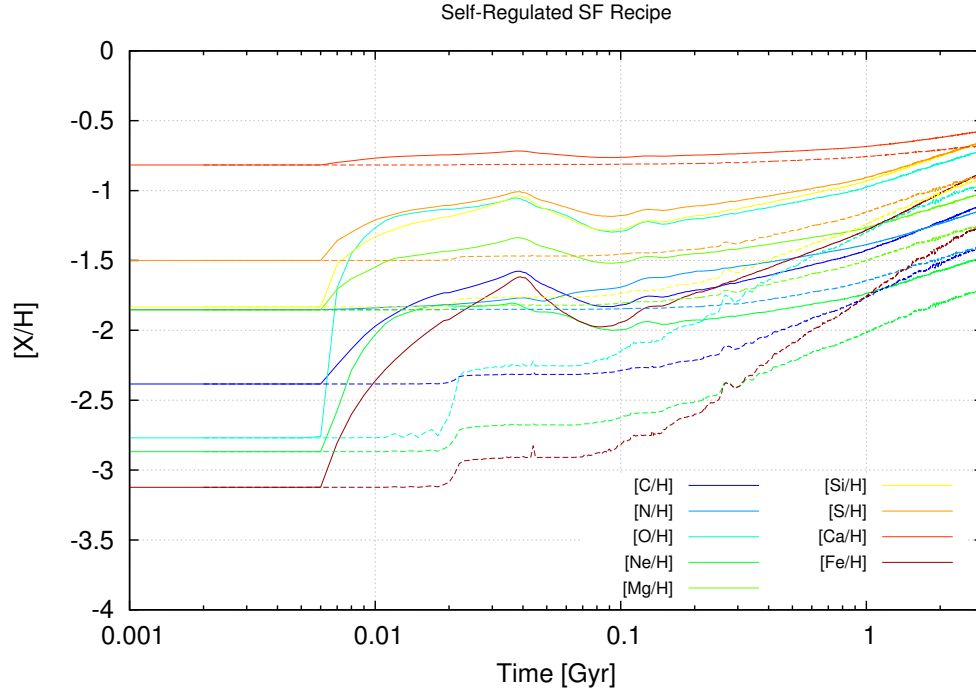


Figure 7.25: Evolution of the chemical abundances for 9 different elements using the self-regulated star-formation recipe. Solid lines indicate compositions of gas, and dotted lines of the stellar component. Values are averaged for the innermost 2.5 kpc radius of the dwarf galaxy.

causes a strong "bump" in the abundance plots. There is also a weak secondary bump, mostly recognisable in N, which is caused about 40 Myr later when the first planetary nebulae start to contribute. This first feature has a steeper shape in run sr01, because in the early phase of the simulation, the self-regulated SF recipe produces more stellar mass and more material is expelled in vertical direction, creating a galactic fountain. Most of this gas falls back in from the side, in horizontal direction from the center, leading to a less prominent second peak compared to the case of the stochastic SF recipe, where type Ia SNe are more concentrated in the central region. This second peak is so recognisable for the case of the stochastic SF recipe mostly because of strong additional starbursts caused by the material which falls back to the center after the initial starburst, as described in the previous section.

Another important question is, how elements are distributed and get mixed with the surrounding medium. To address this issue, the galaxy domain between 0 and 6 kpc is divided into 30 bins, in which the average abundances for O and N are evaluated. The results for both reference runs can directly be compared in fig. 7.26

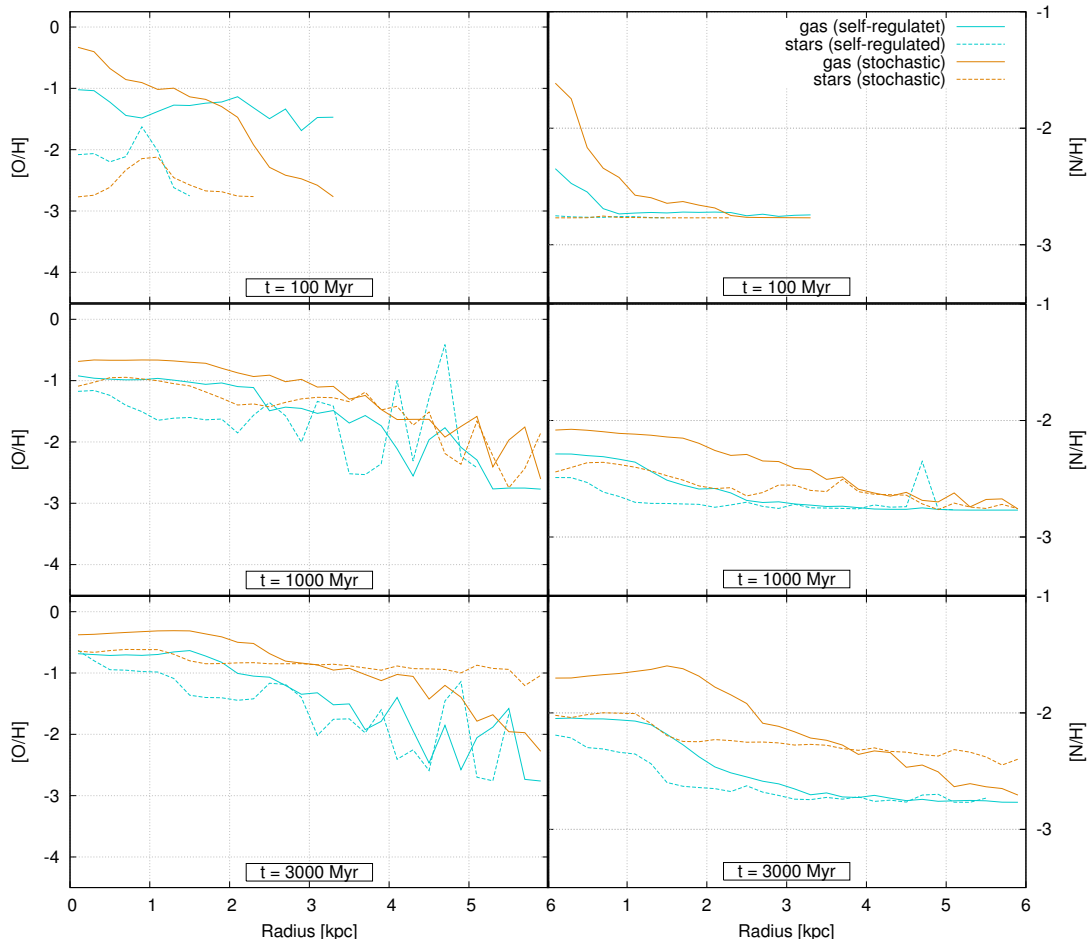


Figure 7.26: Comparison of the O (left column) and N (right column) abundance distribution. Solid lines exhibit values for gas and dashed lines for the stellar component. As usually, turquoise colors indicate run sr01 and orange lines run sto1. Values are calculated for 30 radial bins between 0 and 6 kpc and between ± 1 kpc in vertical direction.

at 3 different times. One finds at 100 Myr simulation time, that for the stochastic SF recipe, gas is more enriched in the center, although the other run managed to turn more gas into stars in the beginning. This is caused by the stronger outflow, as already described. Metal-rich gas is expelled out of the central disc, which thus does not increase its metallicity. Material ejected in vertical direction with $|z| > 1$ kpc, does not contribute to this figure any more. Stars appear to be more enriched in O around a radius of 1 kpc for the self-regulated SF recipe which might be a direct cause of the ring-like structure triggering SF as it expands. This is also the cause why gas is much more enriched in this case for radii above 2 kpc. At this time, neither gas nor stellar particles have reached a radius above 3.5

kpc. Later, in case of the stochastic recipe, gas has been more enriched at most radii due to higher SF. $[O/Fe]$ is only a little bit higher. Figure 7.27 presents the

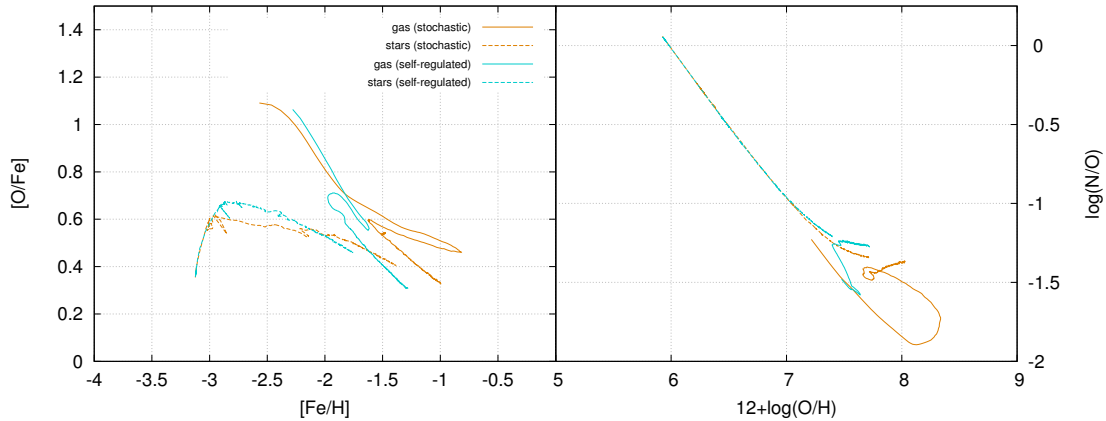


Figure 7.27: *Left*: $[O/Fe]$ abundance relative to solar values as a function of $[Fe/H]$, plotted during the first 1 Gyr. *Right*: Comparison of absolute mass fractions O/H and N/O on logarithmic scale, also for the first Gyr. Gas is indicated by solid lines and the stellar component by dashed lines. Turquoise lines indicate run sr01 where the self-regulated SF recipe was used and orange lines run sto01, carried out with the stochastic SF recipe.

time evolution of iron to hydrogen mass fraction as a function of oxygen over iron relative to solar values. This was done for the innermost 2.5 kpc radius during the first 1 Gyr of the simulation. The right panel exhibits O/H and N/O also for the first 1 Gyr on logarithmic scales, where 12 had been added to the abscissa. The first 10 Myr of the simulation are removed, because of the very fast enrichment during that time. Also these plots confirm the finding, that the stochastic SF recipe is able to enrich the gas somewhat more compared to the other reference run. The Fe/H fraction ends approximately at 1/10 of solar values, whereas the self-regulated run reaches only approximately -1.3 dex, which corresponds to about 1/20 relative to solar values. Both runs show in the left panel of fig. 7.27 a loop, where obviously gas gets diluted, going back to lower iron values. This is also visible in fig. 7.24 and 7.25, where a strong decline is present after the first "bump". Iron is mostly produced by type Ia SNe in the present model and obviously, the small amount of material which stays in the central region after the initial starburst is very quickly enriched with huge amounts of O. Later, when the expelled material starts to fall back, a significant decline of O is visible between the first 70 and 100 Myr of the simulation. It takes another 80 Myr approximately, until enough type Ia SNe occurred, allowing the Fe production rate to overtake

the one of O. The right hand side of fig. 7.27 shows an O/H vs. N/O plot, between 10 Myr and 1 Gyr. Because the first 10 Myr are cut out, gas does not start at a $\log(\text{N/O})$ ratio of 0, but are already shifted down to negative values, because of the first generation of type II SNe, enriching the material with high amounts of O. This track starting at 0 is still visible in the stellar component, which mostly consists of first generation stars, still carrying initial metallicity values. During the simulation gas and stellar components are approaching each other and end up after 1 Gyr at around 8 for $12+\log(\text{O/H})$ in case of run sto01 and approximately 0.25 dex lower for run sr01. The values for $\log(\text{N/O})$ are approximately at -1.4 and around -1.3 for these simulations respectively, which are typical $\log(\text{N/O})$ values for metal-poor dwarf galaxies. Once again, the difference can be explained by the higher amount of stellar mass produced by the stochastic recipe.

Chapter 8

Effects of the Cooling Shut-Off Time τ_{CSO}

The aim of this chapter is to investigate the effects of the cooling shut-off time τ_{CSO} on the behaviour of the same dwarf galaxy system, which was discussed in the previous chapter. In single-phase codes it is in most cases necessary to turn off cooling for a specific fraction of gas near type II SNe, because otherwise most of the feedback energy would be radiated away within a typical time step. In order to be able to also examine possible differences in the sensitivity of a SF recipe on τ_{CSO} , four different runs (sto01, sto02, sto03, sto04) are compared, using the stochastic approach with values for the cooling shut-off time of 1, 10, 20 and 30 Myr, with each other and also with four simulations using the self-regulated SF recipe (sr01, sr02, sr03, sr04).

8.1 Star Formation

In all cases, the SFRs show a clear dependency on τ_{CSO} . This is not very surprising, considering that more energy is radiated away during a simulation run with a shorter τ_{CSO} . The discrepancy in SFR between sr01 ($\tau_{CSO} = 1$ Myr) and sr04 ($\tau_{CSO} = 30$ Myr) is about an order of magnitude when the stochastic SF recipe is used and almost two orders of magnitude for the self-regulated approach (see figs. 8.1 and 8.2). This is caused by the fact that in the self-regulated SF recipe, the mass of the spawned particle is directly depending on the density and more importantly on the temperature of the gas particles, whereas in the stochastic case, the physical parameters are only considered for the density and temperature threshold, but they do not contribute to the SF probability function. Changing this parameter has a huge impact on SF in this case and therefore on

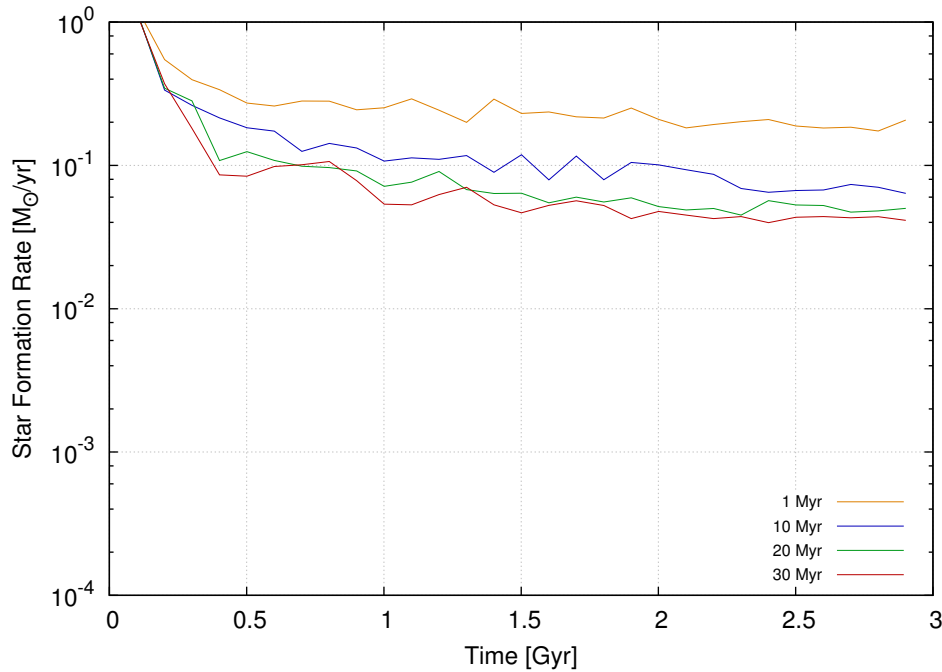


Figure 8.1: SFR for 4 different cooling shut-off times: 1, 10, 20, and 30 Myr, indicated by orange, blue, green and red lines respectively, where the stochastic SF recipe is used. The bin size is 100 Myr.

the overall behaviour of the dwarf galaxy. In Stinson et al. (2006) the authors found very little dependence of the cooling shut-off time on the mean SFR, which is in contrast to these results. One of the reasons for this might be, that in the presented models, no actual blast-wave region is calculated, but the neighbouring SPH-particles which are located inside the smoothing sphere receive feedback and can have their cooling disabled. Therefore, a direct comparison could be problematic. More importantly, in Stinson et al. (2006) a galaxy with baryonic mass content of $4.55 \times 10^{10} M_{\odot}$ was simulated, which means that it has more than 20 times as much gas mass as the dwarf galaxy discussed here. Such a system with relatively flat potential well, simulated in this thesis, is much more sensitive to feedback processes. This surely leads to some discrepancy and is one reason for the different findings. To compare the average SFRs for these simulations, see table 8.1. These values were calculated between 0.5 and 3.0 Gyr, to avoid the strong initial starburst, which would not only lead to huge standard deviations but would also make the differences much harder to see in those results, because a very significant amount of stellar mass is already produced after the first few Myr. These results show that when the stochastic SF recipe is used and the cooling shut-off time is increased from 1 Myr to 30 Myr, in average the SFR is higher

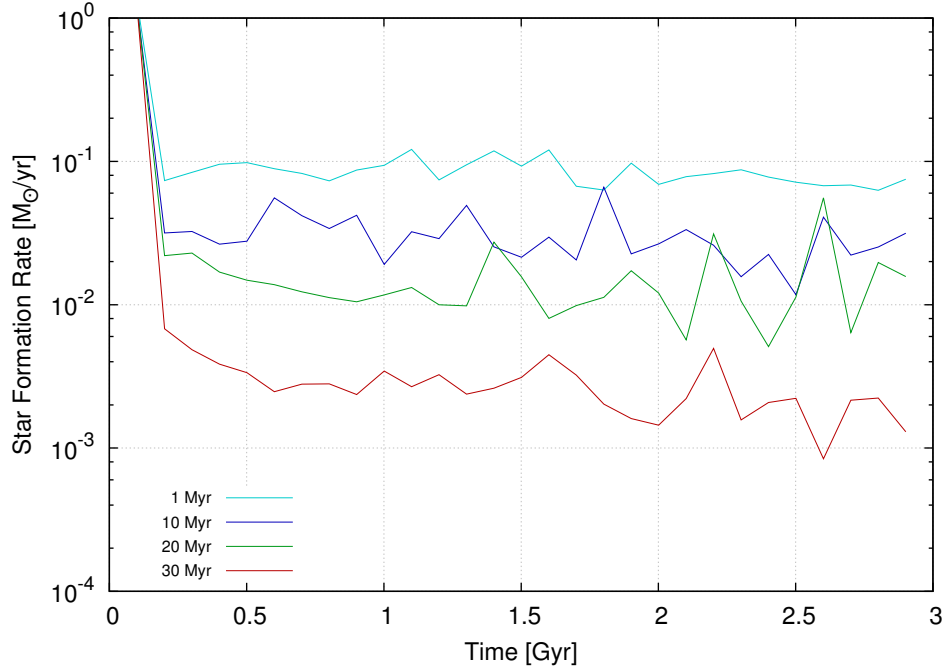


Figure 8.2: As in fig. 8.1 but for the self-regulated SF recipe, where the turquoise line indicates $\tau_{CSO} = 1$ Myr.

by a factor 4.0 ± 0.9 ; for the self regulated recipe this factor is 34.0 ± 4.8 . This suggests, that for such an increase of τ_{CSO} , the self regulated SF recipe reacts much more sensitively, namely by a factor 8.5 ± 0.4 compared with the stochastic recipe. The cause for this is that density and especially the temperature of the gas particle have immediate and direct influence on the self-regulated SF recipe, whereas in the other case the stochastic probability function does not really consider the temperature of particles. Only a temperature threshold is used in this case. Figure 8.3 and 8.4 exhibit the mass evolution for the 8 different simulations discussed in this chapter. Also here one can see clearly, how the amount of stellar mass increases with shorter cooling shut-off time.

8.2 Chemical Evolution

The chemical enrichment of the system is not as strongly influenced by τ_{CSO} as one would probably expect. For higher SFRs the $[O/Fe]$ and $[Fe/H]$ values are higher, but the differences for the gas component after 1 Gyr between a τ_{CSO} of 1 and 30 Myr are less than 0.05 dex and 0.5 dex respectively if the stochastic SF recipe is used (see fig. 8.5). For the comparison runs with the self-regulated approach, the discrepancy between those 4 different runs appears a little bit less

Name	τ_{CSO} [Myr]	ϵ [kpc]	SN_{eff} [%]	SF-recipe	t_{sim} [Gyr]	SFR [$M_{\odot} yr^{-1}$]	σ_{SFR} [$M_{\odot} yr^{-1}$]
sto01	1	0.2	10	stochastic	3.0	2.244×10^{-1}	0.08
sto02	10	0.2	10	stochastic	3.0	9.854×10^{-2}	0.06
sto03	20	0.2	10	stochastic	3.0	6.480×10^{-2}	0.03
sto04	30	0.2	10	stochastic	3.0	5.639×10^{-2}	0.03
sr01	1	0.2	10	self-reg.	3.0	8.427×10^{-2}	0.06
sr02	10	0.2	10	self-reg.	3.0	3.034×10^{-2}	0.04
sr03	20	0.2	10	self-reg.	3.0	1.456×10^{-2}	0.03
sr04	30	0.2	10	self-reg.	3.0	2.481×10^{-3}	0.01

Table 8.1: Results of average SFRs and their standard deviation σ_{SFR} for different cooling shut-off times τ_{CSO} and star-formation recipes.

prominent, but in general one can conclude that the chemical evolution is not very strongly affected by the cooling shut-off time. This is also confirmed by fig. 8.6, where the N/O number density fractions are plotted as a function of O/H. Also here only a small difference can be found for longer τ_{CSO} values.

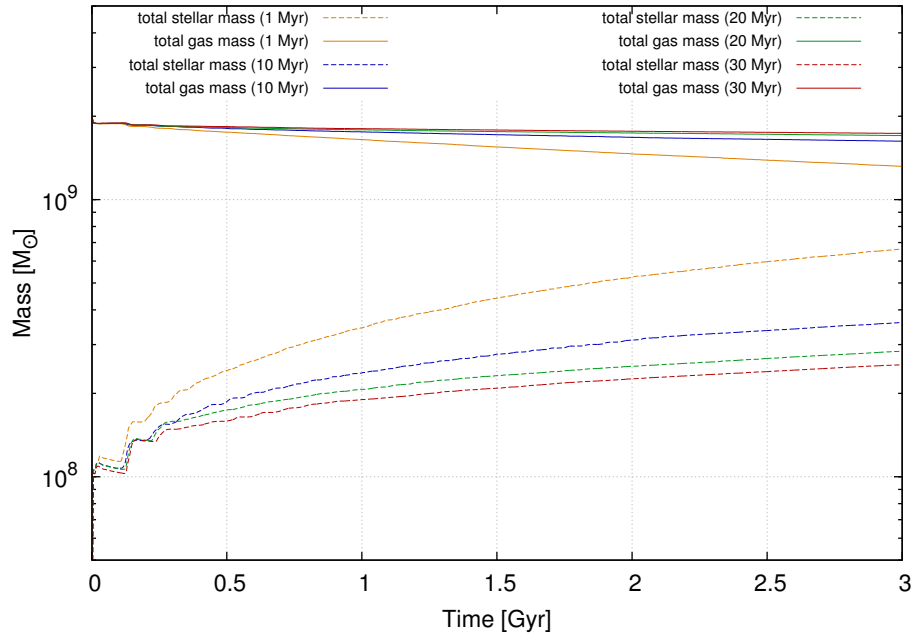


Figure 8.3: Mass evolution for different cooling shut-off times, where the stochastic SF recipe is used. Orange, blue, green and red lines correspond to $\tau_{CSO} = 1, 10, 20$ and 30 Myr respectively. The gas component is represented by solid and the stellar component by dashed lines.

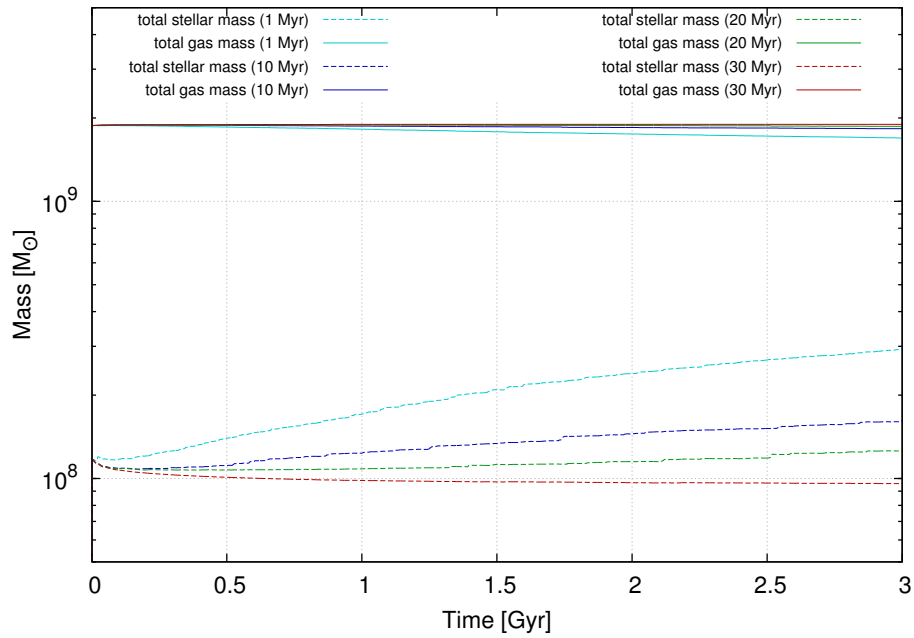


Figure 8.4: As in fig. 8.3 but for the self-regulated SF models where turquoise lines indicate $\tau_{CSO} = 1$ Myr.

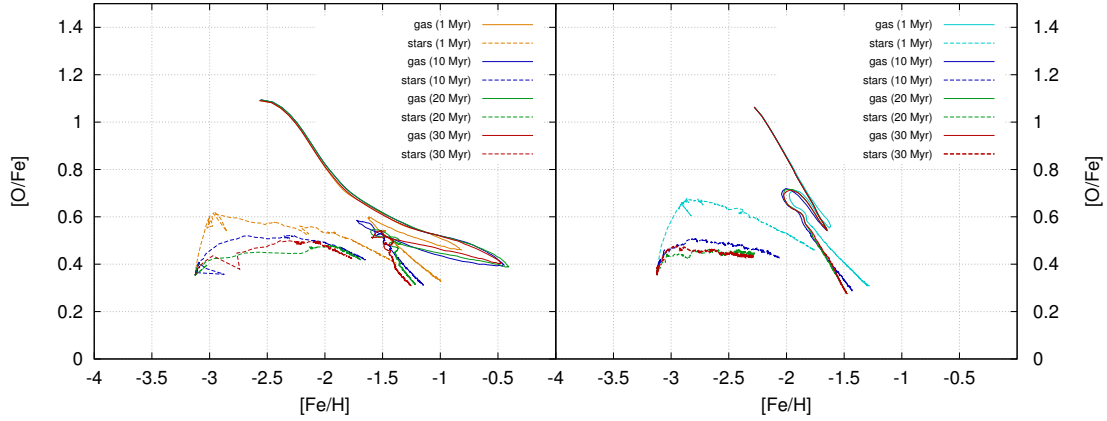


Figure 8.5: $[O/Fe]$ abundance relative to solar values as a function of $[Fe/H]$, plotted during the first 1 Gyr. *Left*: Evolution for different cooling shut-off times using the stochastic SF recipe. Orange, blue, green and red lines correspond to $\tau_{CSO} = 1, 10, 20$ and 30 Myr respectively. *Right*: Same for the self-regulated SF recipe, where the turquoise line shows results for $\tau_{CSO} = 1$ Myr. The gas component is represented by solid and the stellar component by dashed lines.

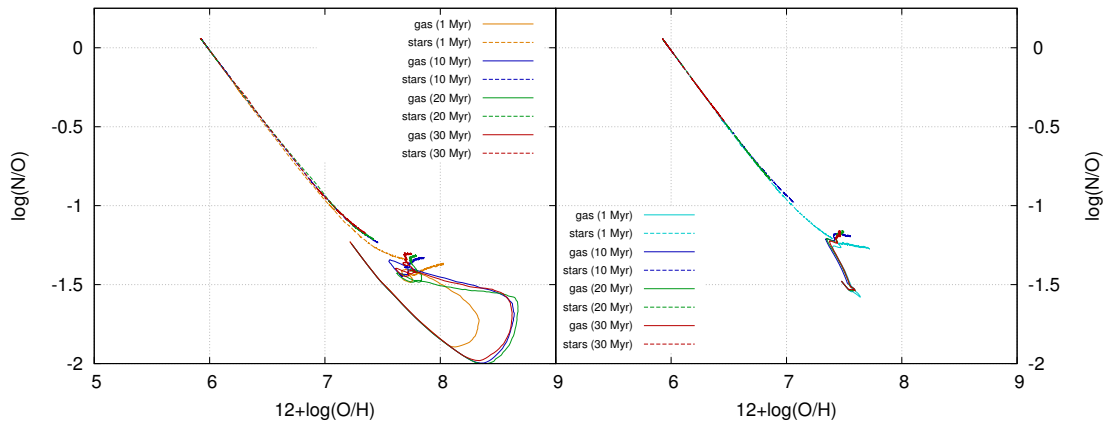


Figure 8.6: As in fig. 8.5 but for the absolute mass fraction N/O as a function of O/H on logarithmic scale.

Chapter 9

Effects of the Gravitational Softening ϵ

As briefly described earlier in this thesis (Chapter 3), the gravitational softening is a very important parameter, which must be set carefully in SPH simulations. A softening is necessary to prevent singularities in gravitational forces for very small particle separations. If the gravitational softening ϵ is set too small, gas would artificially clump and strong accelerations might be encountered. On the other hand, if ϵ is set too large, SPH particles will be prevented to converge on too large scales, leading to big gas clumps with low density (Bate and Burkert, 1997). If a fixed gravitational softening is applied, like in simulations discussed throughout this thesis, it is considered to be a good idea to set ϵ larger than the typical smoothing length h (Springel, 2005), which is in this case, at least for the main body of the galaxy usually < 0.1 kpc. As presented in the next subsections, in some cases the star-formation recipes can react differently on too large values of ϵ . Four simulation runs have been carried out for each of the star-formation recipes. The gravitational softening was set to 0.1, 0.2, 0.5 and 1.0 kpc.

9.1 Star Formation

As expected, the stochastic SF recipe shows a clear increase of the SFR for smaller ϵ , because gas can form clumps more easily, which will get Jeans unstable, collapse and form stellar particles (see fig. 9.1). The average SFRs between 0.5 and 3 Gyr can be compared in table 9.1. For the 1.0 kpc case, SF even completely vanishes on many occasions. In case of the self-regulated SF recipe, similar results have been found (fig. 9.2).

A big difference, however is present if we look at the initial starburst. It is much

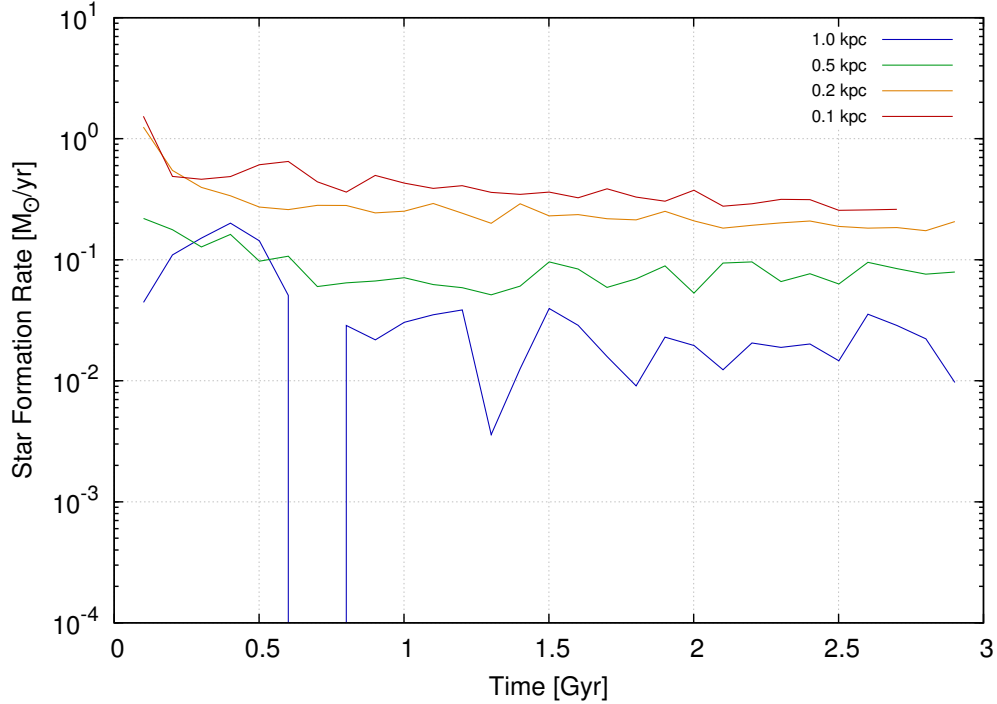


Figure 9.1: SFR for 4 different gravitational softening: 0.1, 0.2, 0.5 and 1.0 kpc, indicated by red, orange, green, and blue lines respectively for the stochastic SF recipe. The bin size is 100 Myr.

stronger for shorter gravitational softening lengths than for longer ones. For runs sr07 and sr06, the SFR within the first few Myr, reached a maximum value of 81.3 and $52.8 \text{ M}_\odot \text{ yr}^{-1}$ respectively. This produced enough feedback energy to push the whole system so far out of its equilibrium, that the $\epsilon = 1.0$ kpc simulation couldn't fully relax again. Only a relatively small fraction of gas was able to fall back into the dark matter potential well within 3 Gyr. In sr06, the system was also more chaotic, compared to other runs after the strong burst at the start, but after 0.5 - 1 Gyr, the SFR went back to a more or less normal level. These differences can probably be seen better, if the overall mass evolution is compared (fig. 9.4 and 9.3). The blue dashed line in fig. 9.3 and 9.4 exhibit the total stellar mass for the stochastic and self-regulated SF approach respectively. In the latter case, about 40 % of the initial gas content is turned into stars. Because there is almost no further SF, it then declines relatively fast due to feedback and even gets overtaken by the 0.1 kpc run. The 0.5 kpc case behaves in a relatively similar way, but the stellar content is shifted down by about $3 \times 10^8 \text{ M}_\odot$. The cause for these findings is most likely the dependency of the stellar particle mass on the SF volume (eq. 4.20) $m_\star = \psi(\rho, T)Vt_{\text{form}}$, where the volume was taken to be a

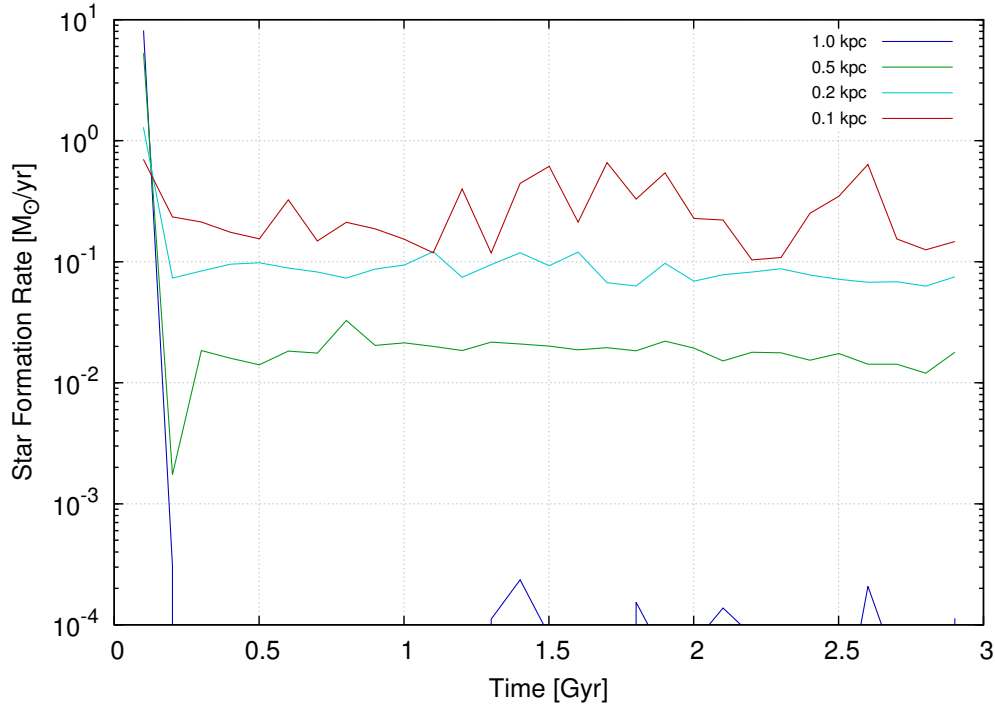


Figure 9.2: As in fig. 9.1 but for the self-regulated SF recipe, where the turquoise line corresponds to $\epsilon = 0.2$ kpc.

sphere with radius of the smoothing length $V = 4\pi h^3/3$. Due to a larger ϵ , in the very beginning of the simulation, most SPH particles do not feel gravity forces and will drift apart, which also increases their h . This will greatly increase their volume enclosed by h and therefore a large number of gas particles are turned into stars completely. One way to prevent this from happening, would be for instance to introduce an additional limitation factor, which artificially quenches SF especially within the first few 10^7 years. In some simulations using this SF scheme, I encountered occasionally some gas particles at high radii which suddenly begin to form star particles with the minimum mass of $1000 M_\odot$. This is caused by the same effect. Although the density is low, there is sometimes the possibility for high smoothing lengths and low temperatures that the mass limit is reached. Nevertheless, this was observed at late simulation times, when only a few gas particles of the hot halo managed to cool down to temperatures well below 10^4 K and therefore, their effect on the evolution of the system should be negligible. It is also interesting to note for short ϵ , a massive strengthening of the frequency of star-formation peaks. In this case, where the gravitational softening is half the size of the reference run, the gravitational forces can act on smaller scales, leading to stronger collapses and higher densities. The subsequently following increase of

Name	τ_{CSO} [Myr]	ϵ [kpc]	SN_{eff} [%]	SF-recipe	t_{sim} [Gyr]	SFR [$M_{\odot}yr^{-1}$]	σ_{SFR} [$M_{\odot}yr^{-1}$]
sto05	1	0.1	10	stochastic	2.7	3.600×10^{-1}	0.21
sto01	1	0.2	10	stochastic	3.0	2.244×10^{-1}	0.08
sto06	1	0.5	10	stochastic	3.0	7.544×10^{-2}	0.06
sto07	1	1.0	10	stochastic	3.0	2.273×10^{-2}	0.06
sr05	1	0.1	10	self-reg.	2.9	2.825×10^{-1}	0.59
sr01	1	0.2	10	self-reg.	3.0	8.427×10^{-2}	0.06
sr06	1	0.5	10	self-reg.	3.0	1.878×10^{-2}	0.01
sr07	1	1.0	10	self-reg.	3.0	5.430×10^{-5}	9.96×10^{-5}

Table 9.1: Results of average SFRs and their standard deviation σ_{SFR} for different gravitational softenings ϵ and star-formation recipes.

the SFR leads to an expansion of the system which will converge again later. It seems that this periodic process, which is also visible for higher softening lengths as well, as discussed in previous sections, gets dramatically increased, especially in case of the self-regulated SF recipe, where the maxima and minima of the SFR can span over more than two orders of magnitude.

9.2 Chemical Evolution

It is clear that, especially due to the much stronger initial starburst in case for big ϵ and the self-regulated star-formation recipe, the chemical evolution of the galaxy must be somewhat different. Within the first 10 Myr of active SF, the central region is enriched so quickly that it reaches solar values for the Fe/H ratio. In fig. 9.5, the first 10 Myr have not been cut out, like in other plots of this kind, in order to see a little bit better what happens at the beginning. Within the first Myr of active SF, the $\epsilon = 1$ kpc case jumps from the initial values for [O/Fe] to 1.4 dex. A few Myr later, the strong starburst wiped the whole central region, examined in fig. 9.5 and 9.6 (inner 5 kpc) free of any gas. This is where the grey solid line vanishes and continues at later times when gas begins to re-enter this area. Similar behaviour can be observed for the 0.5 kpc run (dark grey line). These values should not be viewed as reliable results for dwarf galaxies and are not comparable to real systems, but they still show, how small changes in some parameters are able to cause completely different outcomes also on short time scales. In case of the stochastic SF recipe (left hand side), one can also see some differences between the two simulations with lower and the two with higher ϵ . Also in this case, the latter shows a much stronger burst-like behaviour in the beginning, where one can find decreasingly strong peaks in [O/Fe]. Due to global

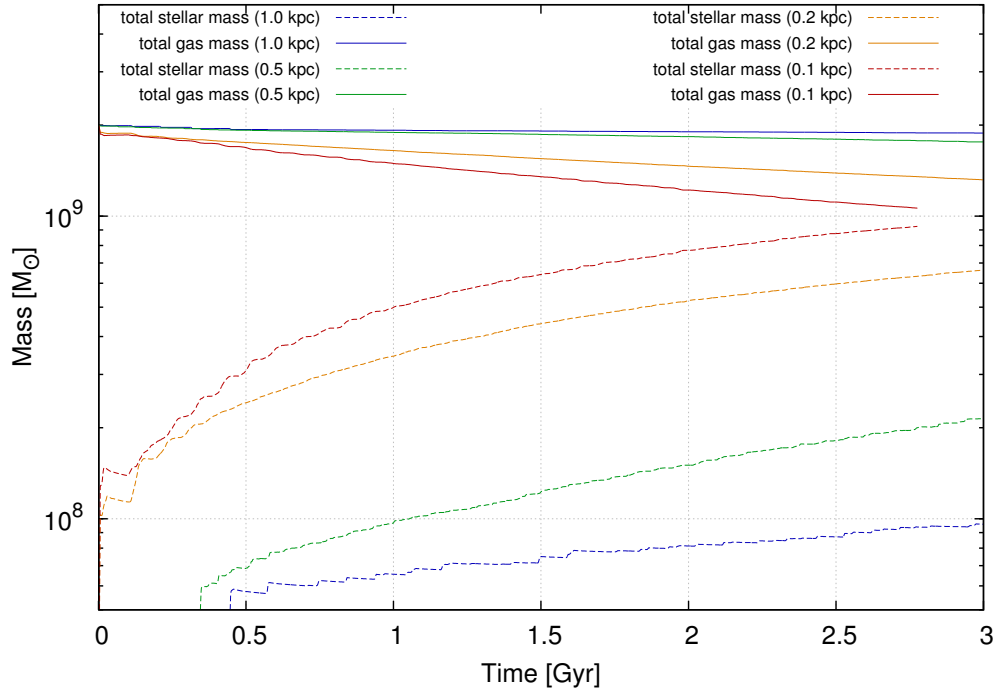


Figure 9.3: Mass evolution for different gravitational softenings, where the stochastic SF recipe is used. Blue, green, orange and red lines correspond to $\epsilon = 1.0$, 0.5 , 0.2 and 0.1 kpc respectively. The gas component is represented by solid and the stellar component by dashed lines.

starbursts at early times, gas is enriched quickly and expelled from the central region, low-metallicity material gets delivered subsequently until the expelled gas falls back in, triggering the next starburst. The other two cases seem to be somewhat more quiescent at early times but also here, the almost periodic peaks in the SFR for the $\epsilon = 0.1$ kpc case are reflected by numerous little bumps of the red solid line in fig. 9.5.

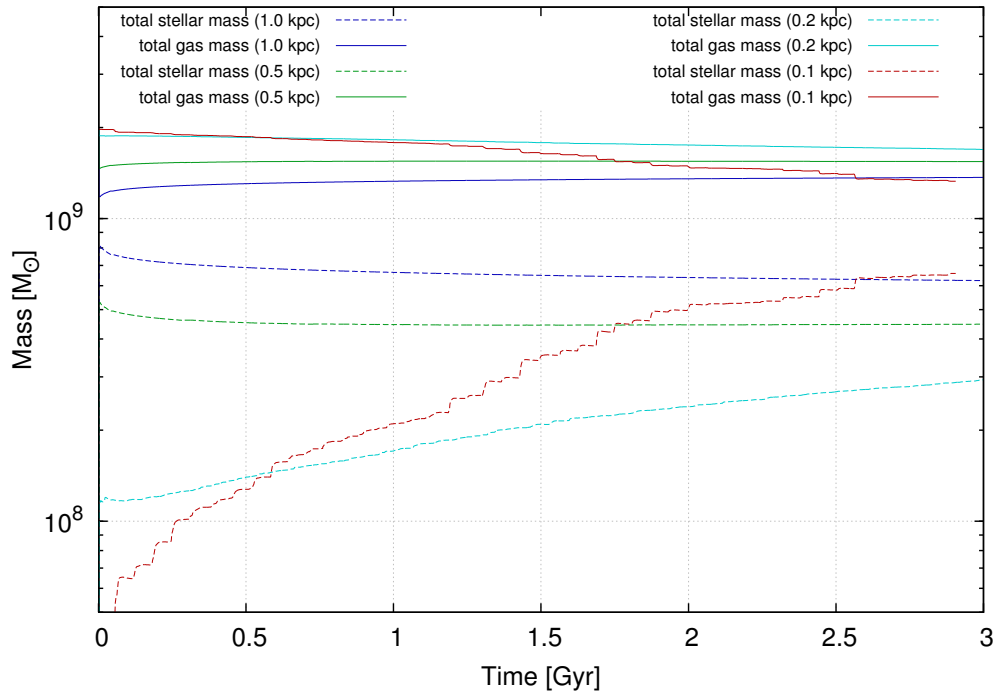


Figure 9.4: As in fig. 9.3 but for the self-regulated SF recipe. The turquoise lines correspond to $\epsilon = 0.2$ kpc. The gas component is represented by solid and the stellar component by dashed lines.

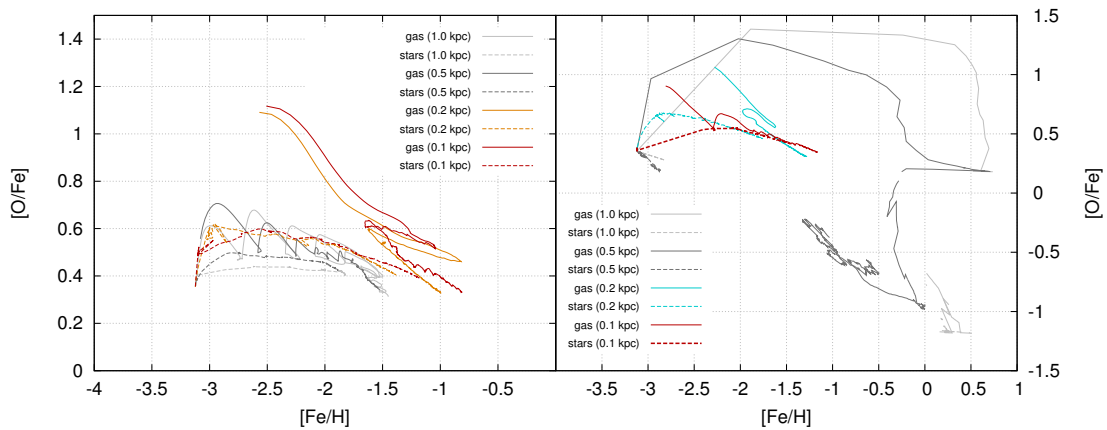


Figure 9.5: $[O/Fe]$ abundance relative to solar values as a function of $[Fe/H]$, plotted during the first 1 Gyr. *Left*: Evolution for different gravitational softening lengths using the stochastic SF recipe. Grey, dark grey, orange and red lines correspond to $\epsilon = 1.0$, 0.5 , 0.2 and 0.1 kpc respectively. *Right*: Same for the self-regulated SF recipe, where the turquoise line shows results for $\epsilon = 0.2$ kpc. The gas component is represented by solid and the stellar component by dashed lines.

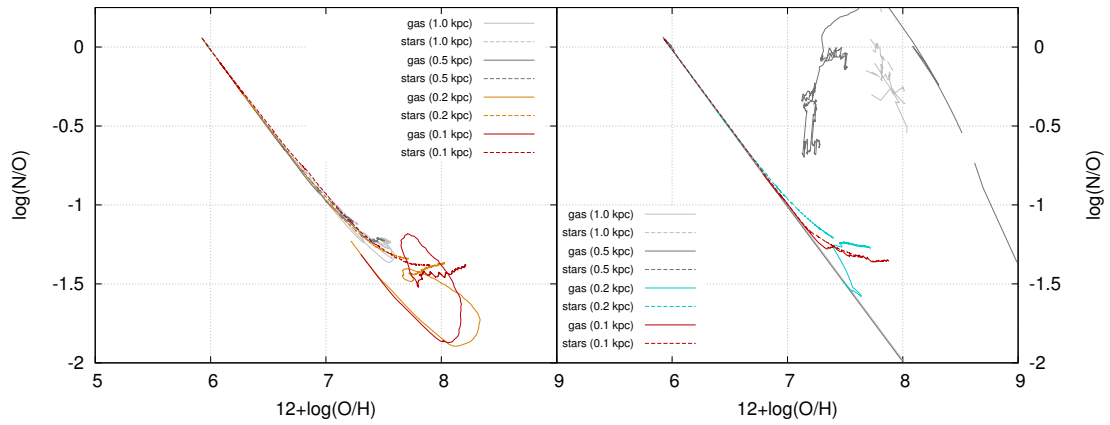


Figure 9.6: As in fig. 9.5 but for the absolute mass fraction N/O as a function of O/H on logarithmic scale.

Chapter 10

Effects of the Supernova

Energy E_{SN}

The efficiency with which the 10^{51} erg SN energy are injected into the ISM is a free parameter in the present models. In general, most simulations of such kind use SN efficiencies of 10 or 5%, because it is believed that the remaining 90 - 95% of SN energy are radiated away. For instance in Thornton et al. (1998) numerical simulations of the evolution of SN remnants were carried out and it was found, that the total energies at late stages was in the range of 9×10^{49} up to 3×10^{50} erg. In this section comparisons are made between the 6 different simulations sto09, sto01, sto08 carried out with $SN_{eff} = 100\%$, 10% and 5% respectively and runs sr09, sr01, sr08 for the same values.

10.1 Star Formation

If the SN efficiency is set to lower values, one would expect that due to less feedback, gas should be able to cool faster leading to a higher SFR. However, these simulations show that this is true for the self-regulated SF recipe but not if the stochastic one is used. Figures 10.1 and 10.3 show that the orange line lies at higher SFR values and that therefore more gas mass is consumed for the 10% simulation. Going down to a SN efficiency of 5% leads, in this case, to a decline of the SFR by $\sim 22.4\%$. In case of the self-regulated recipe it is increased by $\sim 25.6\%$. Both recipes show unrealistic behaviour for a SN efficiency of 100%, leading to a complete destruction of the entire dwarf galaxy during the initial starburst. To compare the average SFRs for these simulations with each other, see table 10.1. In fig. 10.4, where the self-regulated model was used, the SFR for the 100% case does not completely drop to zero like for the stochastic recipe.

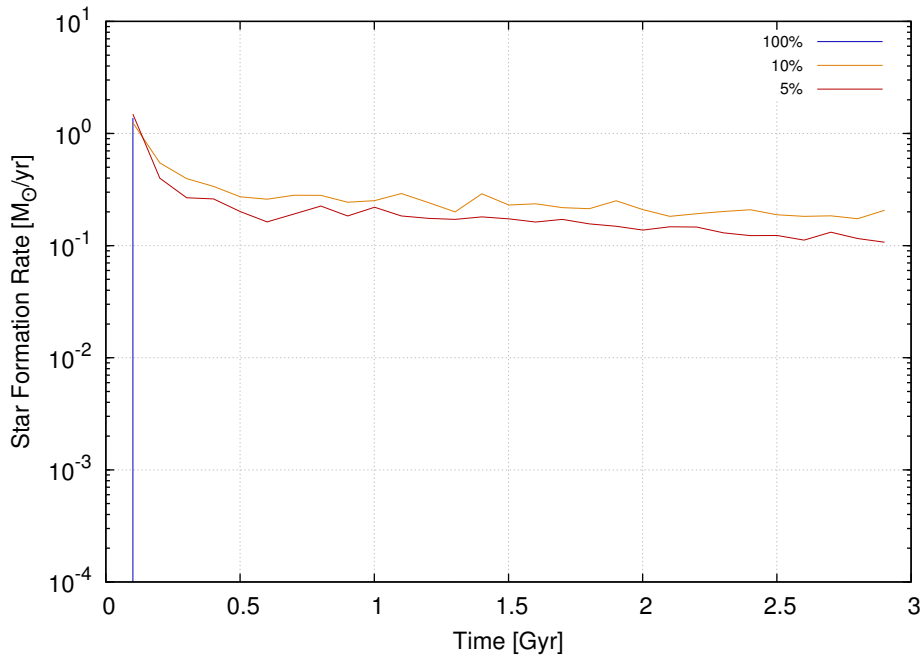


Figure 10.1: SFRs using the stochastic recipe, for 3 different SN efficiencies: 5%, 10% and 100%, indicated by red, orange and blue lines respectively. The bin size is 100 Myr. Note that the SFR for the 100% case is only visible until 100 Myr because later the SFR is always close to zero.

10.2 Chemical Evolution

Similar to the last chapter, where the central region was wiped free from gas due to the very strong initial starburst, also here for the case of 100% SN feedback efficiency a similar behaviour occurs. Therefore, the grey lines in fig. 10.5 and 10.6 represents no reliable results for real dwarf galaxies. Besides of that, a comparison between the 10% and 5% cases are interesting. Due to the higher SFR of run sto01 compared with the $SN_{eff} = 5\%$ simulation, the $[Fe/H]$ and $[O/Fe]$ values both are a little bit higher. The difference is ~ 0.05 dex respectively. One can also see, that the "loop", which is visible in these abundance plots, is less prominent for the lower SN efficiency. This finding confirms that this feature is most probably caused by the initial starburst, as described earlier, which is of course weaker when a lower amount of energy is injected into the ISM. In case of the stochastic SF recipe, element abundances end at higher values for the $SN_{eff} = 5\%$ case, where the SFR is higher compared to the standard value. The difference is approximately 0.1 dex for $[Fe/H]$ and 0.05 dex for $[O/Fe]$. Also in this case it can be clearly seen that the "loop" feature is less noticeable.

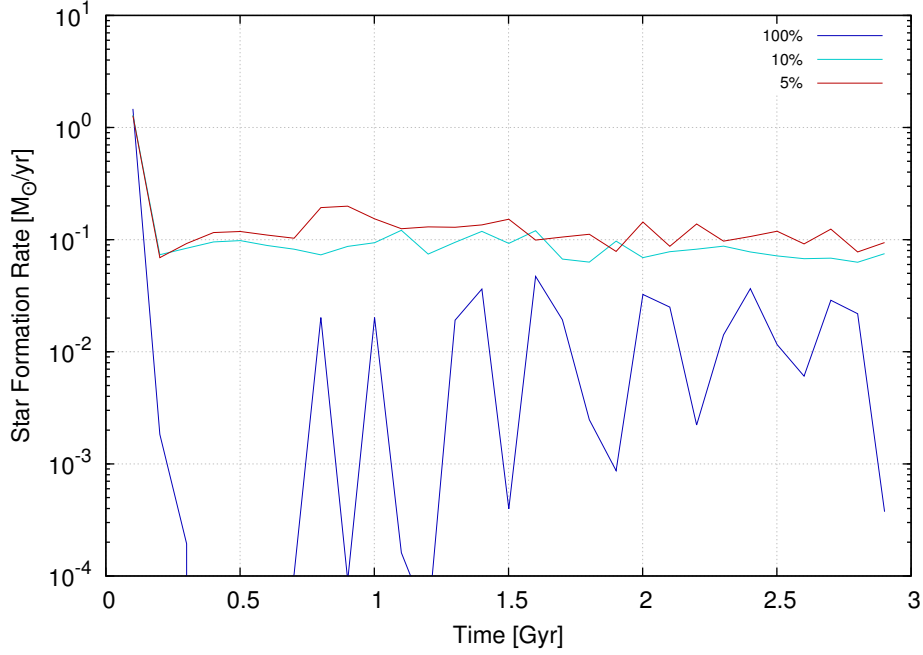


Figure 10.2: As in fig. 10.1 but for the self-regulated SF recipe where the turquoise line corresponds to $SN_{eff} = 10\%$.

Name	τ_{CSO} [Myr]	ϵ [kpc]	SN_{eff} [%]	SF-recipe	t_{sim} [Gyr]	SFR [$M_{\odot}yr^{-1}$]	σ_{SFR} [$M_{\odot}yr^{-1}$]
sto08	1	0.2	5	stochastic	3.0	1.562×10^{-1}	0.07
sto01	1	0.2	10	stochastic	3.0	2.244×10^{-1}	0.08
sto09	1	0.2	100	stochastic	3.0	-	-
sr08	1	0.2	5	self-reg.	2.9	1.214×10^{-1}	0.11
sr01	1	0.2	10	self-reg.	3.0	8.427×10^{-2}	0.06
sr09	1	0.2	100	self-reg.	3.0	1.442×10^{-2}	0.03

Table 10.1: Results of average SFRs and their standard deviation σ_{SFR} for different SN efficiencies and star-formation recipes.

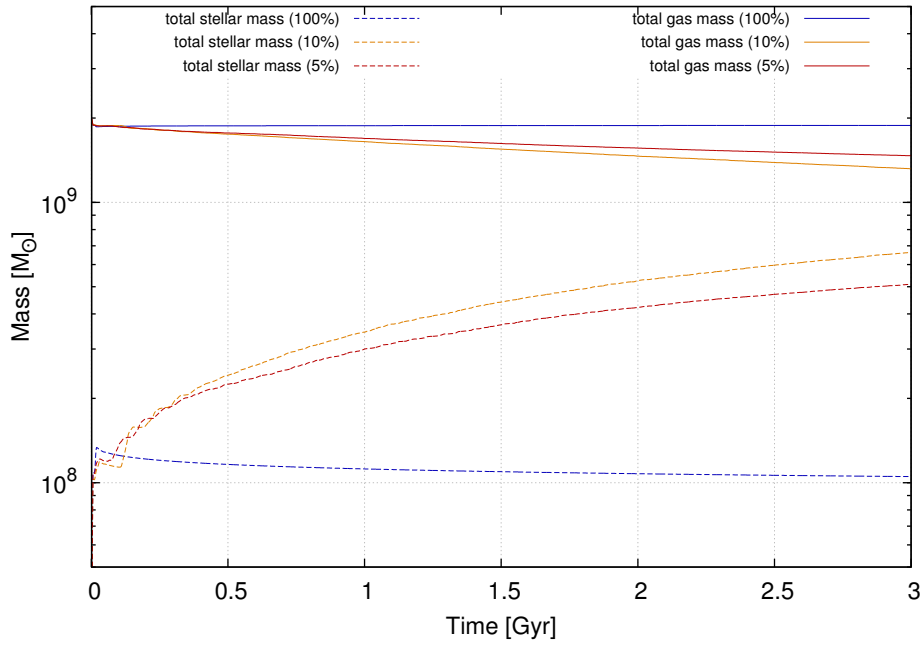


Figure 10.3: Mass evolution for different SN efficiencies, where the stochastic SF recipe was used. Red, orange and blue lines correspond to $SN_{eff} = 5\%$, 10% and 100% respectively. The gas component is represented by solid and the stellar component by dashed lines.

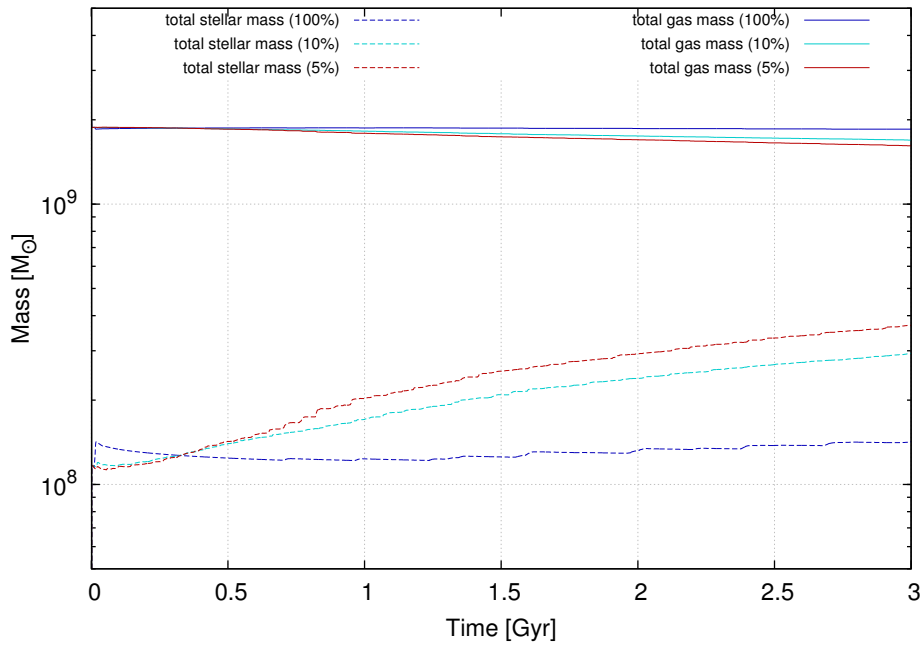


Figure 10.4: As in fig. 10.3 but for the self-regulated SF recipe where the turquoise lines correspond to $SN_{eff} = 10\%$.

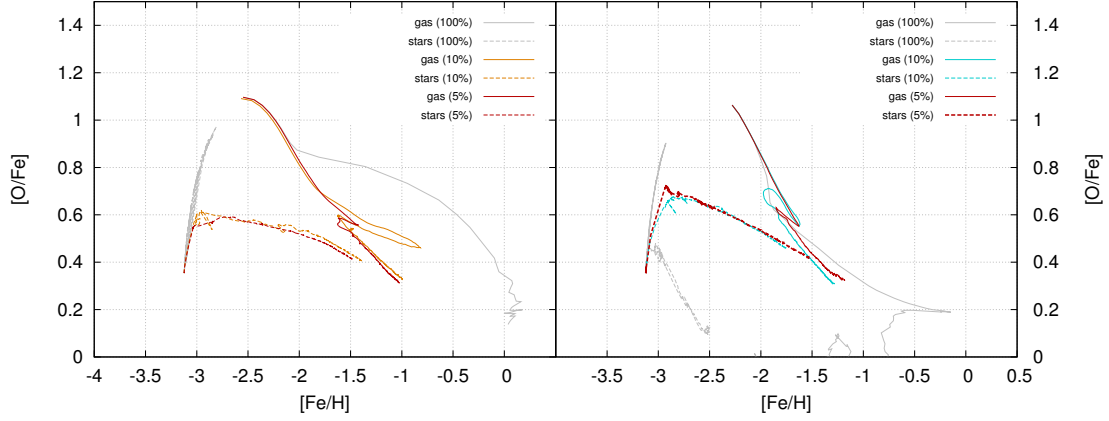


Figure 10.5: $[O/Fe]$ abundance relative to solar values as a function of $[Fe/H]$, plotted during the first 1 Gyr. *Left:* Evolution for different SN efficiencies using the stochastic SF recipe. Red, orange and grey lines correspond to $SN_{eff} = 5\%$, 10% and 100% respectively. *Right:* Same for the self-regulated SF recipe, where the turquoise line shows results for $SN_{eff} = 10\%$. The gas component is represented by solid and the stellar component by dashed lines.

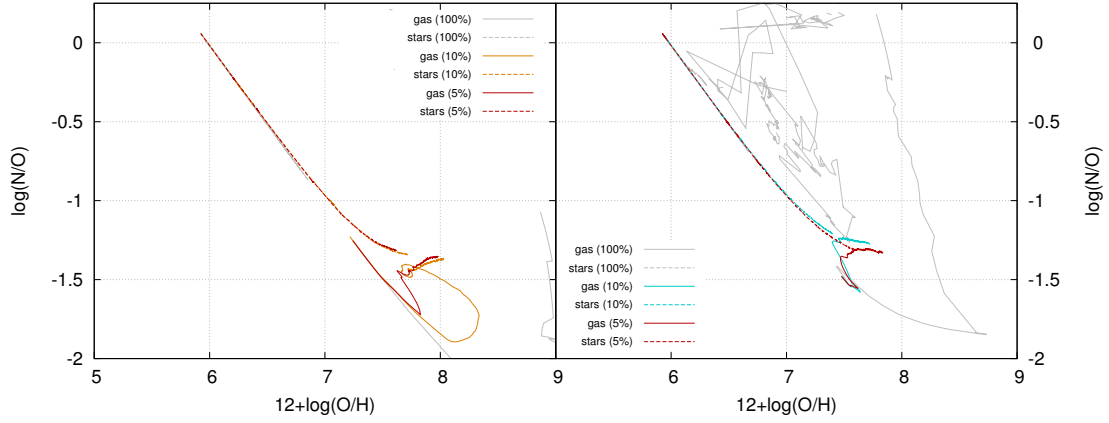


Figure 10.6: As in fig. 10.5 but for the absolute mass fraction N/O as a function of O/H on logarithmic scale.

Chapter 11

Comparisons With the Multi-Phase Model

The aim of this chapter is to compare results of the presented simulations carried out via a single phase description of gas with the multi-phase code "cdSPH", developed by Liu et al. (2015). As explicitly described in section 6.1, almost identical initial conditions of this dwarf galaxy system discussed in previous chapters are used. Additionally, as mentioned earlier, the same cooling functions and feedback tables are implemented. This offers us the opportunity to investigate the effects of a multi-phase description of the ISM.

11.1 The Multiphase Description

It is useful to introduce very briefly the concepts of a multiphase description at first. For a more extensive discussion considering this topic, let me refer you to Theis and Hensler (1993) or Harfst et al. (2006). The basic idea of the multi-phase description is to treat hot/warm gas separately from cold clouds. In this case, the authors used the so-called "sticky" particle scheme (Theis and Hensler, 1993), where cold gas clouds are treated as N-body particles and hot/warm gas with the standard SPH description, like in the single phase code. Cold clouds can coagulate due to collisions. This is done by applying a collisional cross section to them. If two such clouds collide, the newly formed cloud is placed in the center of mass of the two former particles. The resulting velocity is the one of the center of mass and the surplus kinetic energy is transformed to thermal energy. Cold clouds can of course also fragment if they form stars and subsequently receive stellar feedback. Such a cloud is divided into four smaller clouds symmetrically, which get the velocity of an expanding SN shell and additionally, 5% of the feedback energy of

the newly formed star are transferred to the kinetic energy of the 4 smaller cloud particles. The rest of the stellar feedback is also treated somewhat differently to the single phase description, because only cold clouds receive feedback from stellar wind, whereas only hot/warm particles get feedback from SNe. This also means that mass ejected by type II SNe is only deposited in the hot/warm medium, not in cold clouds. Nevertheless, the hot/warm and cold phases can exchange mass, momentum and energy between each other due to condensation, evaporation and also drag forces. The latter is directly caused by the different dynamics of the two components. The force acting on a cold cloud, moving through a homogeneous hot medium with relative velocity $\vec{v}_{cl} - \vec{v}_{hot}$ is

$$\vec{F}_D = -C_D \cdot \pi h_{cl}^2 \rho_{hot} \cdot |\vec{v}_{cl} - \vec{v}_{hot}| \cdot (\vec{v}_{cl} - \vec{v}_{hot}), \quad (11.1)$$

where C_D is the drag coefficient, which is set to 0.1 in Liu et al. (2015) and h_{cl} the cloud size.

11.2 Initial Set Up

The overall properties of the dwarf galaxy system, like mass and density distribution are the same in both cases and have already been described in section 6.1. However, there are some minor differences already in the initial conditions. The properties of different components for the single- and multi-phase simulations are summarized in table 11.1, including masses, temperatures and number of particles.

Component	Mass [M_\odot]	Temperature [K]	No. of particles init. in total
hot/warm	4×10^7	10^6	2×10^4
cold	1.96×10^9	10^3	1×10^4
single-phase gas	4×10^7	10^6	4082
single-phase gas	1.96×10^9	10^4	2×10^4

Table 11.1: Initial set up for the multi-phase model of Liu et al. (2015) and my single-phase model.

The particle numbers and masses were changed in order to match the total mass fraction between hot/warm and cold component of the multi-phase simulation. The temperature of the colder gas particles is 10^4 K instead of 10^3 K, because otherwise the initial starburst would have been much higher, and probably leading to the complete destruction of the dwarf galaxy. The initial metallicity of gas in the multi phase simulation is zero, but it was noted by the author that it does not

differ much from runs where the initial metallicity was set to some small value. As described before, in both simulations, the initial conditions were evolved without any physics except for gas dynamics, as a pure N-body and SPH run for 200 Myr, which allows the gas to find a quasi-equilibrium. Gas particles with radii > 20 kpc were removed from the simulation after this time. In my case, from 24082 particles, 23584 remained, in case of the multi-phase description, 12819 from 20000 hot/warm and 9998 from 10000 cold particles remained.

11.3 Star Formation

Although the overall evolution of the model is relatively similar in both cases, it is worth mentioning that the starburst in the beginning, which occurs when cooling and SF are activated, is not present with such strength in the multi-phase simulations (see fig. 11.1). In this case, the SFR is also higher at the beginning, but starts at approximately $1 M_{\odot} yr^{-1}$, whereas for the single-phase case it can exceed $100 M_{\odot} yr^{-1}$, but just within 1 Myr and then drops down to low values. Liu et al. (2015) report that their system also breaks out of equilibrium after $t = 0$ and is able to relax after the first 100 Myr. In the presented models, this process takes about 200 or 300 Myr. At a simulation time of about 900 Myr, both cases reach a SFR at around $0.1 M_{\odot} yr^{-1}$ but for the multi-phase simulation it seems to steadily decline. The SFR in the single-phase simulation stays relatively constant not only during the first Gyr but during the total simulation time of 3 Gyr. This difference can be seen also very well in fig. 11.3, where the green solid line exhibits the total mass of cold clouds. It declines faster than the solid turquoise line showing the total single-phase gas mass. At about 200 Myr, the cumulative stellar mass of the multi-phase model exceeds the one of the single-phase simulation due to the higher SFR. At this point it should be mentioned that the SF recipe used in Liu et al. (2015) is a Jeans criterion, where the Jeans length

$$\lambda_J = c_{cl} \sqrt{\frac{\pi}{G\rho_{cl}}} \quad (11.2)$$

is compared to the cloud size h_{cl} , and must be smaller than that in order to form stars. c_{cl} is the sound speed in eq. 11.2. It is assumed that the mass enclosed by the Jeans volume V_J is turned into stars within a free-fall timescale of $\tau_{ff} = \sqrt{3\pi/(32G\rho)}$ multiplied by a randomized SF efficiency factor ϵ between

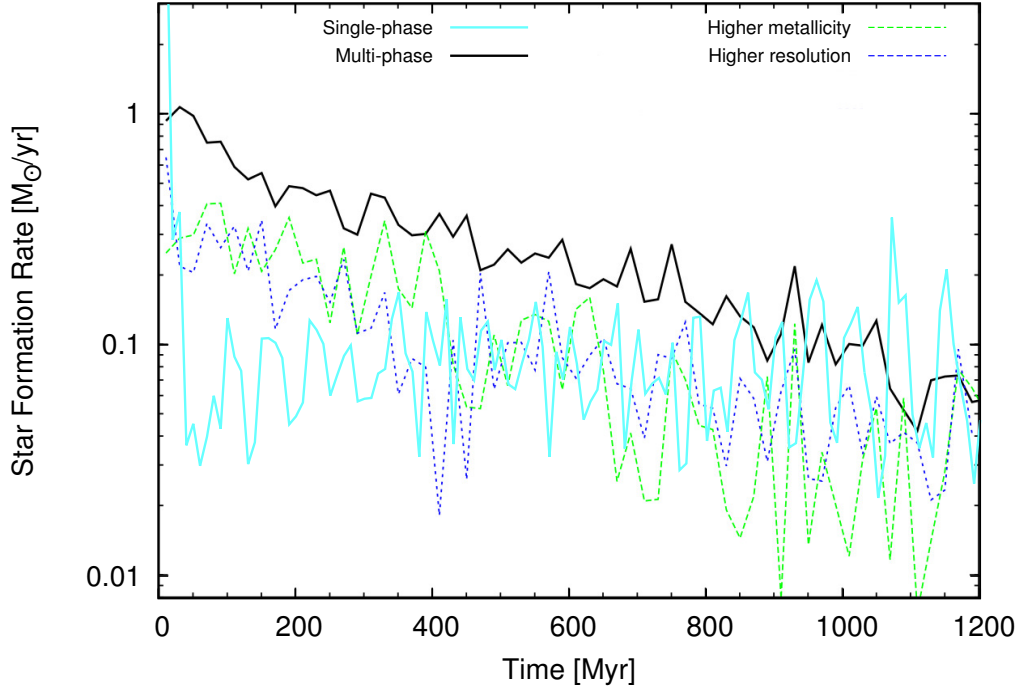


Figure 11.1: SFR for the first 1200 Myr. Turquoise and black solid lines correspond to single- and multi-phase simulations. The green and blue dashed lines exhibit models with higher initial metallicity ($5 \times 10^{-2} Z_{\odot}$) and higher resolution (10^5 instead of 10^4 cold cloud particles), for the multi-phase model. The picture is taken from Liu et al. (2015) with results of the presented single-phase description overplotted.

0.01 and 1. Therefore, the maximum SFR is

$$\frac{d\rho_{\star}^{\max}}{dt} = \frac{M_J}{\tau_{ff}V_J} = \frac{4}{3}\sqrt{\frac{6G}{\pi}}\rho_{cl}^{3/2} \quad (11.3)$$

and with the additional efficiency factor we get

$$\frac{d\rho_{\star}}{dt} = \epsilon \frac{d\rho_{\star}^{\max}}{dt}. \quad (11.4)$$

Additionally, they use another probability criterion which only allows for 0.5% of cold clouds to form stars within 1 Myr. This is equivalent to an inactive timescale of 200 Myr. Such a criterion is an effective SF quenching mechanism, which seems to be very useful, especially to suppress the initial starburst and therefore makes an important difference. Because of this criterion, during the first Myr in which SF is active, only a maximum of 0.05% of the initial total cold cloud mass can turn

into stars, which is $9.8 \times 10^6 M_{\odot}$. In the case of the single-phase model, where this criterion is not included, more than $10^8 M_{\odot}$ of stars are produced during this time. During this first Myr, feedback from the first generation of stars will further quench SF, especially because it consists of stellar wind and radiative feedback, heating up the cold clouds. It is clear that due to the 10 times higher stellar mass in the beginning, the single-phase model will already evolve somewhat differently from the multi-phase case, but after both systems found their equilibrium state again and the multi-phase model's stellar mass begins to overtake the one of the single-phase description, one can see that their total internal energies reach the same plateau (see fig. 11.2). It is also interesting to note the different evolution

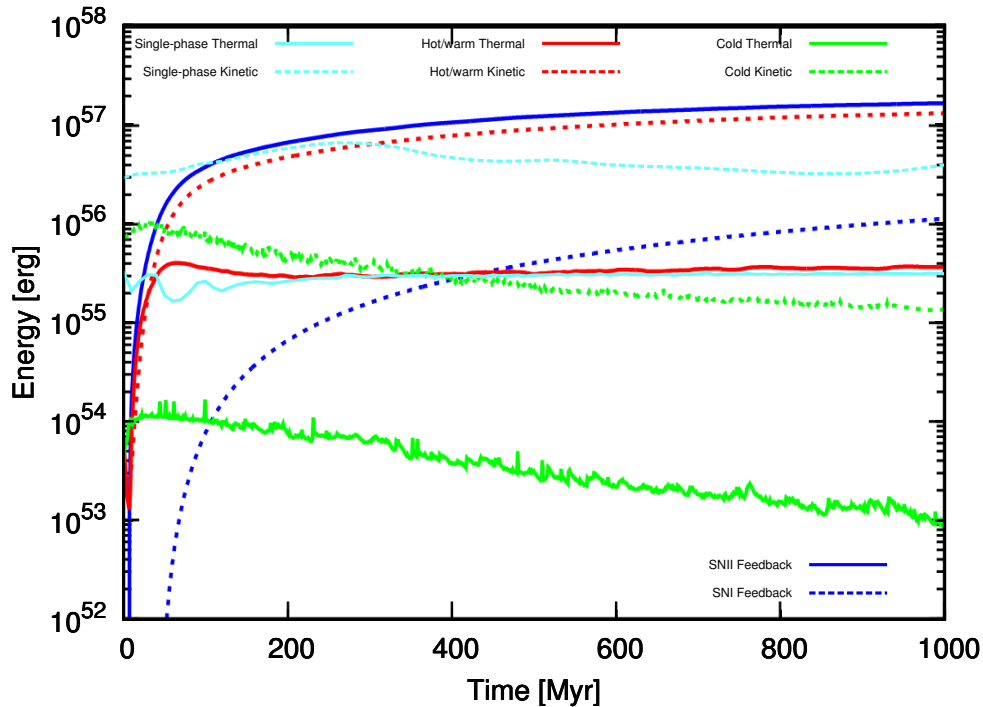


Figure 11.2: Energy evolution during the first 1 Gyr. Red and green lines correspond to hot/warm gas and cold clouds respectively. Turquoise lines exhibit results from the single-phase code (run sr01). Blue lines show the accumulated SN energies from the multi-phase simulation. The picture is taken from Liu et al. (2015) with my results of the single-phase description plotted over.

of the kinetic energy, which is not surprising considering that in the multi-phase description not only drag forces act on clouds, but they also get additional kinetic energy due to SF, namely the velocities of an expanding SN shell when they fragment and additionally 5% of the stellar feedback, as mentioned above.

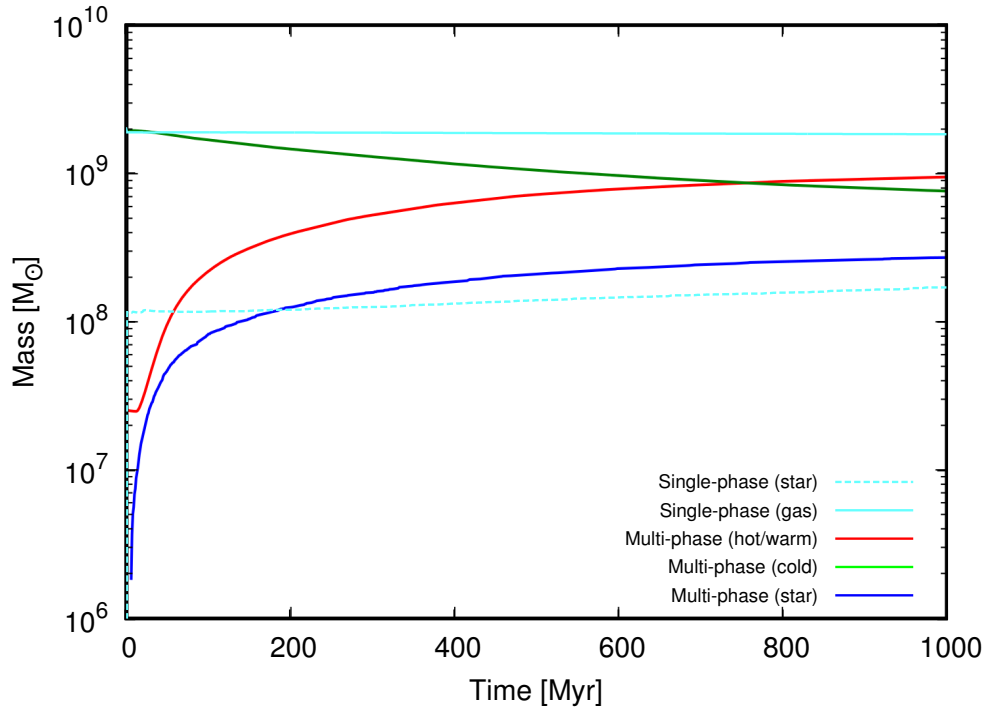


Figure 11.3: Mass evolution during the first 1 Gyr. Red, green and blue lines correspond to hot/warm gas, cold clouds and stellar component of the Multi-phase simulation respectively. Turquoise lines exhibit results from the single-phase code (run sr01). The picture is taken from Liu et al. (2015) with my results of the single-phase description plotted over.

11.4 Chemical Evolution

Figure 11.4 shows O/H abundance ratios relative to solar values as a function of radius at time $t = 1$ Gyr. It can be clearly seen that the oxygen abundances for gas in the single-phase simulation attain much lower values compared to the hot/warm component in the multi-phase case. In the central regions, the difference is 0.3 - 0.4 dex, but for higher radii the distinction is much stronger. The multi-phase model shows even a little increase of [O/H] with radius, whereas in the other case it declines. At a radius between 2 - 3 kpc, where the density of the single-phase dwarf galaxy goes down to $\sim 10^{-24}$ g cm $^{-3}$, one can see a stronger decline of O. This is a strong indication that the multi-phase model is able to mix its hot/warm gas more efficiently. This confirms the finding that for the single-phase simulation, most of the hot gas which gets heated up by stellar feedback in the central region is trapped in an envelope of cooler gas, which explains the strong gradients in

density, temperature and chemical abundances with radius. Interestingly, the cold clouds in the multi-phase model show a comparable radial decline in $[O/H]$, but have 0.5 - 1 dex lower values. This can be explained with the fact that type II SNe inject their feedback only into the hot/warm component, which implies that most of the produced O will not contribute directly to cold clouds. As explained in Liu et al. (2015), the condensation rate is low, especially for higher radii, which means that most of the oxygen is carried away by the hot/warm component due to outflow. This also explains why the stellar component in the single phase simulation is more enriched compared to the multi-phase, where the stellar particles are produced by cold clouds with relatively low O content.

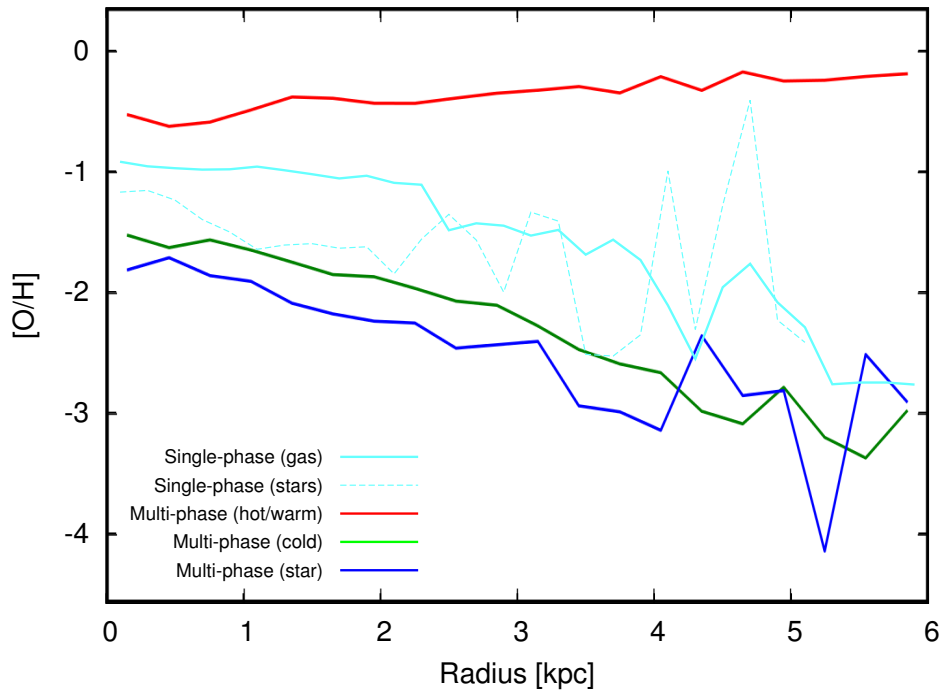


Figure 11.4: Radial oxygen abundances at a simulation time of 1 Gyr. Red, green and blue lines correspond to hot/warm gas, cold clouds and stellar component of the Multi-phase simulation respectively. Turquoise lines exhibit results from the single-phase code (run sr01), where the dashed line exhibits stellar values. The picture is taken from Liu et al. (2015) with my results of the single-phase description plotted over.

The chemical evolution with time shows additionally that the overall enrichment of the system is stronger for the multi-phase simulation, which is once again a result of the higher SFR in this case. Interestingly, fig. 11.5 shows that the $[Fe/H]$ values for the stellar component are more than 1 dex higher than for the multi-

phase case and this is also true for the single-phase models carried out by Liu et al. (2015), which is caused by the same reasons already explained above for the oxygen abundances. Fe is mainly produced by SNeIa but their ejected material go into the hot phase and the cloudy phase remain iron-poor. The resulting values for the single-phase reference simulations can be reconstructed very well with only small differences after 1 Gyr, also for the gas component (blue and red dotted line in fig. 11.5). This confirms that due to the decoupled way of treating

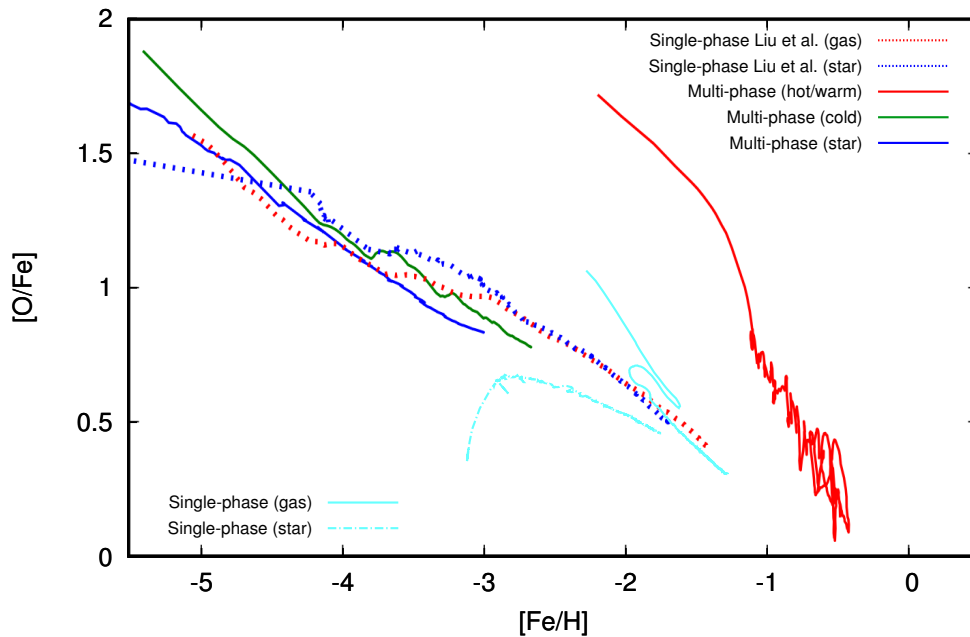


Figure 11.5: Fe/H abundances relative to solar values as a function of O/Fe, plotted during the first 1 Gyr. The line colors and types are the same as in previous figures. The picture is taken from Liu et al. (2015), where a SN efficiency of 100% was used and with my results of the single-phase description (run sr01) plotted over.

hot/warm gas and cold clouds, the chemical abundances between gas and stars develop bigger differences between each other, whereas in the single phase models, these differences are much smaller and the overall abundance values lie somewhere between hot/warm gas and stars or clouds of the multi-phase description. The same can be said about the O/H and N/O number density fractions (fig. 11.6), where the results for single-phase simulations lie also between the values of the cold cloud and hot/warm component of the multi-phase case. The gas component of the presented simulations are here also in agreement to single-phase runs of Liu et al. (2015). The turquoise dashed line starts at 0, which is in contrast to the

reference simulations, because as mentioned in section 6.1, N and O both start with a fraction of 10^{-5} of the gas particle mass. Nevertheless, this makes only a minor difference due to the fast enrichment of the system and within 1 Gyr, one can see that the discrepancy is approximately 0.3 dex in $\log(\text{N}/\text{O})$ for both, the stellar and gas component. Liu et al. (2015) also compared his results with observational data of HII regions from van Zee et al. (1997), which are indicated as black crosses in fig. 11.6. The values for the presented single-phase models are located at the low O/H end of these observations, whereas the hot/warm component of the multi-phase simulations are relatively close to the center of these data points.

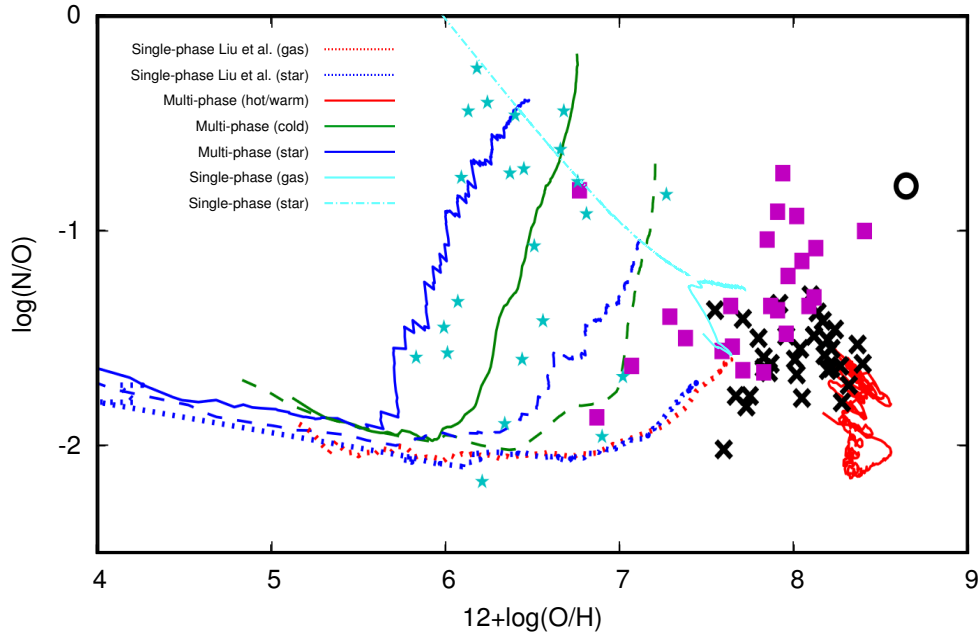


Figure 11.6: N/O fraction as a function of O/H on logarithmic scale, for the first Gyr. The line colors and types are the same as in previous figures. The picture is taken from Liu et al. (2015) with my results of the single-phase description plotted over. Additionally, the blue and red dashed lines show results of the reduced SN energy model (with $SN_{eff} = 10\%$) discussed in Liu et al. (2015). Observational data was already included for comparisons: galactic extremely metal-poor halo stars are labelled with cyan pentagons (Spite et al., 2005) and magenta squares (Israelian et al., 2004). Black crosses show observations of HII regions from van Zee et al. (1997). The black circle indicates solar values from Asplund (2005); Caffau et al. (2009).

Chapter 12

Brief Summary

The main aims of this master thesis are:

1. To investigate differences between a stochastic star formation recipe using a density threshold of 12.2 cm^{-3} , a temperature threshold of $1.5 \times 10^4 \text{ K}$ and a convergence criterion with another star formation recipe based on self-regulation equations in which the mass of the produced SSPs are directly depending on the density and temperature of the ISM.
2. To compare different settings of numerical parameters, in particular the cooling shut-off time, the gravitation softening length and the SN efficiency and to examine their effects on each of the two different SF recipes.
3. To investigate the differences between the single-phase and multi-phase gas description of the ISM and how they effect the chemo-dynamical evolution of a dwarf-galaxy system.

The single-phase SPH code presented in this thesis was developed using the publicly available N-body and SPH code *Gadget-2* from Volker Springel as its basis. Cooling, star formation and different feedback processes were implemented in order to address the issues outlined above. For this purpose, particle simulations of a dwarf galaxy system are carried out and the effects of three very important parameters, which are widely used in SPH simulations, are summarized below in three figures. Those are showing the average star-formation rate as a function of the cooling shut-off time, the gravitational softening and the SN efficiency, which makes it easier to realize the essence from the previous chapters.

The SFR is for both cases inversely proportional to the cooling shut-off time, which is exactly what one would expect, considering the higher amount of thermal energy, which can be radiated away from the gas. For short τ_{CSO} , the stochastic

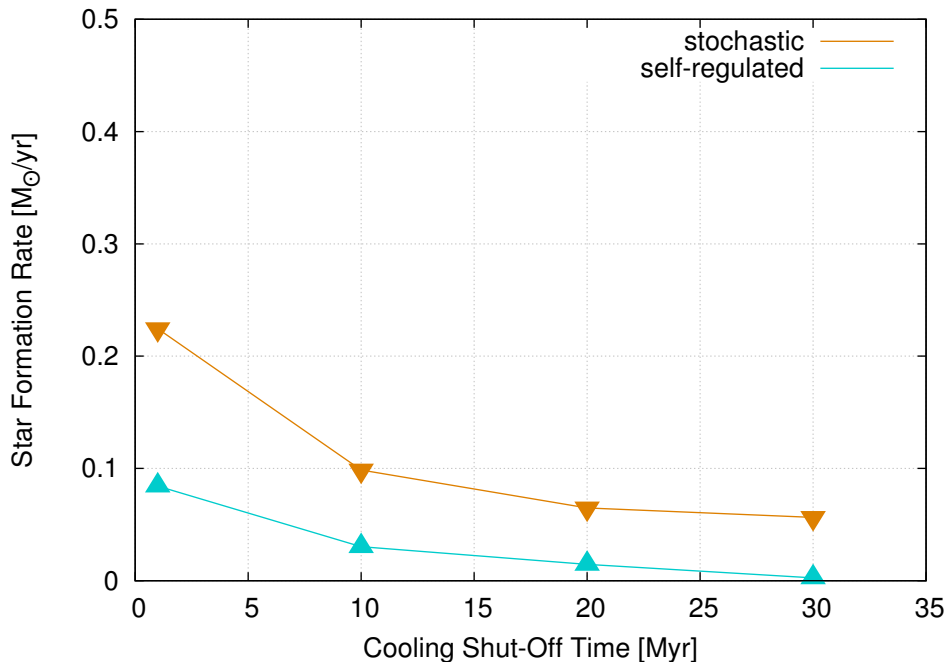


Figure 12.1: Average SFR between the first 0.5 and 3 Gyr as a function of the cooling shut-off time. Orange inverted triangles show results of the stochastic SF recipe and turquoise triangles for the self-regulated recipe.

SF recipe leads to a much higher SFR compared to the self-regulated case. In fact, the differences between the two recipes are increased by a factor 8.5 if τ_{CSO} is reduced from 30 to 1 Myr. One of the reasons for this might be, that the self-regulated SF recipe is able to form stars at radii $r > 2$ kpc. Although this happens at a very low rate, it leads to $(15.3 \pm 1)\%$ more gas particles with disabled cooling.

An interesting result was found concerning the dependence of the average SFR with the length of the gravitational softening. Because of the higher density which can be reached due to gravitational collapses of gas, it is clear that low values for ϵ lead to higher SFR. This assumption was confirmed, as can be seen in fig. 12.2. Both recipes show a very comparable increase of the SFR from the standard value of $\epsilon = 0.2$ kpc to $\epsilon = 0.1$ kpc. Nevertheless, if the initial starburst would be considered for the average values of the SFRs, for longer softening lengths the behaviour would be rather different because the volume of the star formation region is taken to be the smoothing length h . If h reaches abnormal large values, the mass of the potentially spawned star particle can reach the lower mass limit of $1000 M_{\odot}$ also for low densities. Normally, the gravitational softening does not differ too much from the typical smoothing length, and therefore, this issue should

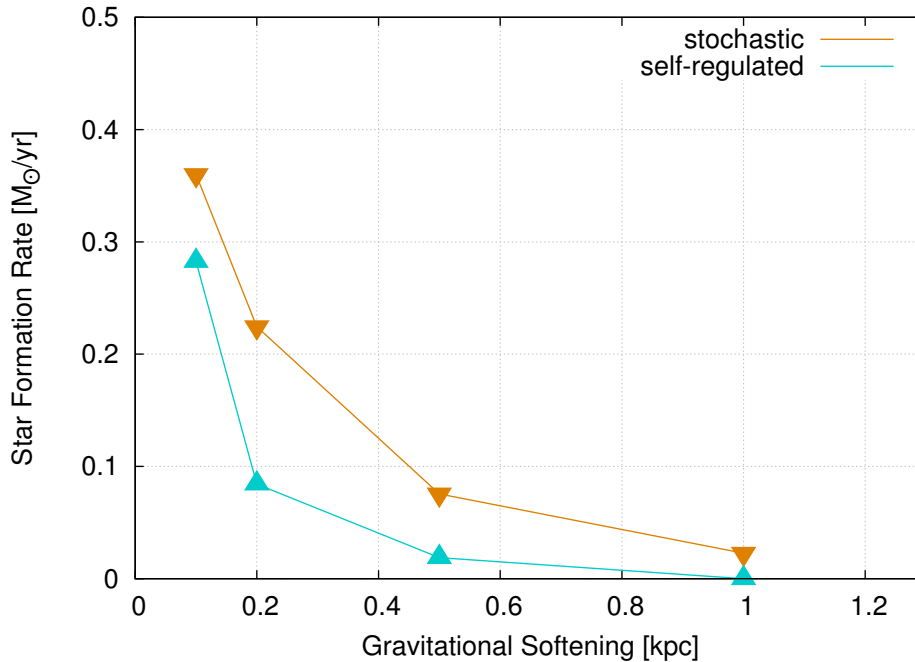


Figure 12.2: Same as fig. 12.1, but for the average SFR as a function of the gravitational softening.

not be a problem for reasonable simulation settings.

The supernova efficiency regulates how much energy is injected into gas surrounding stellar particles. The self-regulation process due to star formation should therefore be higher leading to a lower SFR. This was not confirmed in case of the stochastic SF recipe. Although we were not able to find the exact reason for this phenomenon, we believe the lack of strong turbulences in the first few 100 Myr of the simulation caused by the initial star burst leads to a different evolution of the system which, in case of $SN_{eff} = 10\%$ ends up with a higher average SFR.

The comparisons with a multi-phase description for the ISM shows that the mixing seems to be not as efficient as in the multi-phase description. This can be seen in metallicity gradients, which are e.g. for O slowly increasing with r , whereas in the single-phase case just the opposite was observed. The reasons for this are, that the hot/warm particles can more easily travel outwards, because they are not blocked by cold particles. The single phase code seems to form an envelope of cooler SPH particles, which manage to hold the hot gas particles in the central region. The multi-phase description treats cold clouds as N-body particles and therefore do not contribute to hydro forces and are only indirectly interacting with the hot/warm phase. Another finding is the great discrepancy between the stellar and the gas component considering their metallicity. This is also caused by the decoupled

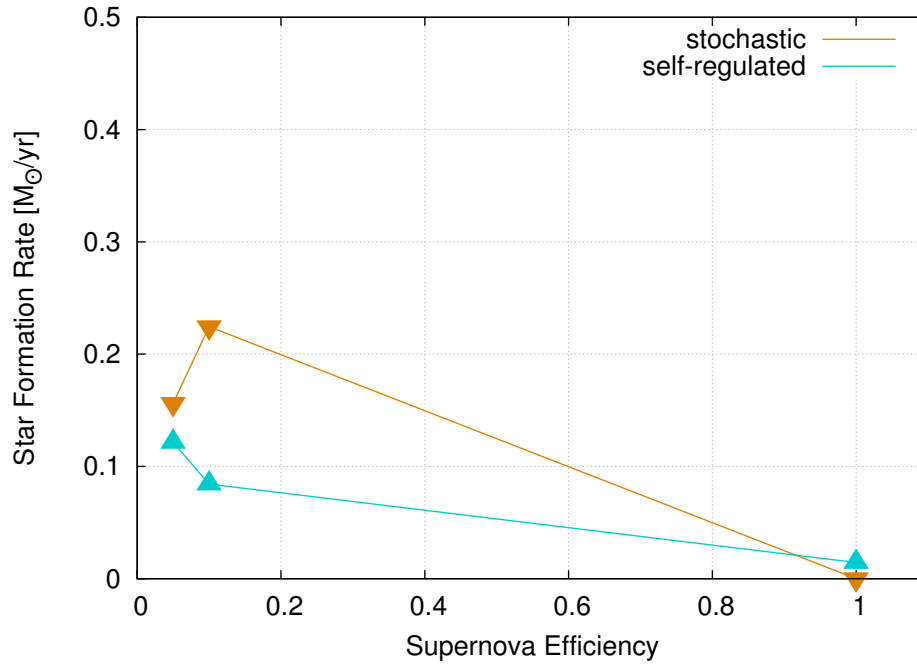


Figure 12.3: Same as fig. 12.2, but for the average SFR as a function of the SN efficiency.

treatment of the two different gas phases, especially when it comes to feedback as explained in chapter 11. Results for the single-phase description show only a minor difference in metallicity between stellar component and gas, but they seem to produce element abundances which are lower for the gas component compared to the hot/warm phase and higher abundances of the stellar component compared to the one of the multi-phase description. Similar results were also found by Liu et al. (2015).

Acknowledgements

I want to express my gratitude to all people who supported me during the emergence of this thesis, especially to my supervisor Prof. Gerhard Hensler for his guidance and the encouragement throughout my entire studies in Vienna. I also want to thank in particular Simone Recchi for being an inspiring example, Sylvia Plöckinger for many useful discussions and of course Lei Liu, who travelled to Vienna for introducing me to his work. Special thanks are also given to my colleague Patrick Steyrleithner, with whom a valuable friendship emerged during the work on both our master theses. Big thanks also to Elisabeth Fahrngruber and Patricia Trinkl for all their collaboration and the beautiful time we had together in the last few years during our studies. I'm also thankful to Volker Springel, for making *Gadget-2* publicly available. The computational results presented have been achieved (in part) using the Vienna Scientific Cluster (VSC).

At the last I want to point out that this work would never have been possible without the support and aid of my parents, which is one among many reasons, why I owe a great debt of gratitude to them.

Matthias Kühtreiber
Vienna, May 23rd 2015

Abstract English

The implementation of star formation in numerical simulations on galaxy scales and cosmological structures is still a matter of much debate and multiple indispensable experiments. The reason for this are the irresolvable physical processes on sub-grid scales. A large variety of different methods have been developed and applied over the last decades. Nevertheless, we are still in the test phase in which way the choice of parameter sets are affecting the simulation results. In order to examine this issue further, we present N-body/SPH simulations of isolated dwarf galaxies for two different star-formation recipes, one with the commonly used star-formation threshold parameters and one derived under the assumption of self-regulation equations. Further emphasis has been put on possible choices of free parameters and the smoothing length of SPH particles. For these studies we use the public version of Gadget-2 with self-implemented sub-resolution physics as a single-phase gas description. Moreover, we directly compare these results with a multi-phase Nbody/SPH code "cdSPH", developed in our group, where the same sub-resolution physics as e.g. gas cooling and stellar feedback by energy and chemical yields, have been implemented, while the interstellar medium is divided into the two dominating gas phases. These are allowed to evolve dynamically and energetically separately, but are coupled by not freely parameterizable drag and mass exchange. Here we will discuss differences in star-formation rates, gas dynamics, and chemical evolution of the different components. Our results suggest that artificial parameters, like e.g. the cooling shutoff time, strongly influence the different star formation recipes with varying strengths. The system reacts very sensitively on the choice of the gravitational softening length, which can also influence star-formation recipes in different ways, depending on how the density and/or the star-formation volume is implemented. If the supernova efficiency is chosen too high, a dwarf galaxy system can easily get torn apart. Surprisingly, sudden starbursts are found in this isolated dwarf galaxy simulation, where large regions become unstable, collapse and produce 10^5 to $10^6 M_{\odot}$ stellar mass, within just a few Myr. This occurs only for short cooling shutoff times. Comparisons

between the single- and multi-phase descriptions show a strong impact on the star-formation rate. Additionally, in the single-phase model, the amount of ejected gas from the central region is clearly lower due to the inherent mixing compared to the multi-phase simulations, which also affects the chemical enrichment of the system.

Abstract Deutsch

Die Implementierung von Sternentstehung in numerischen Simulationen auf galaktischen Skalen und kosmologischen Strukturen ist nach wie vor sehr problematisch und Experimente diesbezüglich sind notwendig. Der Grund dafür sind physikalische Prozesse, die wegen der limitierten Genauigkeit und Rechenleistung nicht aufgelöst werden können. In den letzten Jahrzehnten wurden viele verschiedene Methoden entwickelt und erfolgreich angewendet. Nichtsdestoweniger sind wir immer noch in der Testphase, vor Allem was die Wahl von Parametern angeht, die Simulationen beeinflussen. Um dieses Problem näher behandeln zu können, präsentieren wir N-körper/SPH Simulationen von isolierten Zwerggalaxien für zwei verschiedene Sternentstehungsrezepte, eines mit den weit verbreiteten Schwellwerten zur Sternentstehung und ein weiteres, abgeleitet aus Gleichungen zur Selbstregulierung. Mögliche Werte für freie Parameter und der Glättungslänge von SPH-Teilchen wurden genauer betrachtet. Für diese Untersuchungen wurde die öffentlich verfügbare Version von Gadget-2 verwendet, mit selbst implementierter Physik und einphasen Gasdynamik. Außerdem wurden die Ergebnisse mit einem mehrphasen N-körper/SPH Code "cdSPH" verglichen, der in unserer Gruppe entwickelt wurde, mit gleicher Kühlung und stellarem Feedback, wohingegen das interstellare Medium getrennt ist in die beiden dominierenden Gasphasen. Diese können sich unabhängig voneinander dynamisch und energetisch entwickeln, sind aber dennoch über nicht frei parametrisierbare Widerstandskräfte und Masseaustausch aneinander gekoppelt. Es werden Unterschiede in den Sternentstehungsraten, der Gasdynamik und der chemischen Entwicklung der einzelnen Komponenten diskutiert. Die Ergebnisse lassen vermuten, dass freie Parameter wie beispielsweise die Kühlungs-Abschaltzeit, starken Einfluss auf die verschiedenen Sternentstehungsrezepte haben, mit zum Teil unterschiedlichen Stärken. Das System reagiert sehr sensibel auf die Wahl der gravitativen Dämpfungslänge, was auch Sternentstehungsrezepte verschieden beeinflussen kann, je nachdem wie die Dichte und/oder das Volumen des Sternentstehungsgebiets einget. Wenn die Supernovaenergie zu hoch gewählt wird, kann ein solches Zwerggalaxiensystem mit

Leichtigkeit auseinander gerissen werden. Überraschenderweise treten plötzliche Starbursts in dieser isolierten Zwerggalaxie auf. Größere Gebiete werden instabil und kollabieren, wodurch 10^5 bis $10^6 M_{\odot}$ Sternmasse innerhalb nur weniger Myr erzeugt werden. Dies ist nur zu beobachten, wenn die Kühlungs-Abschaltzeit klein gewählt wird. Vergleiche zwischen der Ein- und Mehrphasenbeschreibung zeigen starken Einfluss auf die Sternentstehungsrate. Außerdem ist in der Einphasenbeschreibung die Menge an hinausgetriebenem Material von der Zentralregion eindeutig geringer im Vergleich zur Mehrphasenbeschreibung, was ebenfalls die chemische Entwicklung beeinflusst.

Bibliography

- Asplund, M. (2005). New Light on Stellar Abundance Analyses: Departures from LTE and Homogeneity. *ARA&A*, 43:481–530.
- Barnes, J. and Hut, P. (1986). A hierarchical $O(N \log N)$ force-calculation algorithm. *NAT*, 324:446–449.
- Bate, M. R. and Burkert, A. (1997). Resolution requirements for smoothed particle hydrodynamics calculations with self-gravity. *MNRAS*, 288:1060–1072.
- Bekki, K. (2008). Formation of blue compact dwarf galaxies from merging and interacting gas-rich dwarfs. *MNRAS*, 388:L10–L14.
- Berczik, P. P. and Petrov, N. I. (2003). Calculation of the SSP chemical evolution. *Kinematika i Fizika Nebesnykh Tel*, 19:36–49.
- Boehringer, H. and Hensler, G. (1989). Metallicity-dependence of radiative cooling in optically thin, hot plasmas. *A&A*, 215:147–149.
- Briggs, J. (2012). Modelling Star Formation and Feedback in Smoothed Particle Hydrodynamics using Gadget-2. Master’s thesis, University of Edinburgh.
- Bruzese, S. M., Meurer, G. R., Lagos, C. D. P., Elson, E. C., Werk, J. K., Blakeslee, J. P., and Ford, H. (2015). The initial mass function and star formation law in the outer disc of NGC 2915. *MNRAS*, 447:618–635.
- Burkert, A. and Ruiz-Lapuente, P. (1997). Dormant Dwarf Spheroidal Galaxies, Deactivated by Type Ia Supernovae. *A&A*, 480:297–302.
- Caffau, E., Maiorca, E., Bonifacio, P., Faraggiana, R., Steffen, M., Ludwig, H.-G., Kamp, I., and Busso, M. (2009). The solar photospheric nitrogen abundance. Analysis of atomic transitions with 3D and 1D model atmospheres. *A&A*, 498:877–884.

-
- Chiosi, C. and Carraro, G. (2002). Formation and evolution of elliptical galaxies. *MNRAS*, 335:335–357.
- Dalgarno, A. and McCray, R. A. (1972). Heating and Ionization of HI Regions. *ARA&A*, 10:375.
- Dekel, A. and Silk, J. (1986). The origin of dwarf galaxies, cold dark matter, and biased galaxy formation. *A&A*, 303:39–55.
- Eckart, C. (1960). Variation Principles of Hydrodynamics. *Physics of Fluids*, 3:421–427.
- Elson, E. C., de Blok, W. J. G., and Kraan-Korteweg, R. C. (2010). The dark matter content of the blue compact dwarf NGC 2915. *MNRAS*, 404:2061–2076.
- Elson, E. C., de Blok, W. J. G., and Kraan-Korteweg, R. C. (2011). Three-dimensional modelling of the H I kinematics of NGC 2915. *MNRAS*, 415:323–332.
- Ferrara, A. and Tolstoy, E. (2000). The role of stellar feedback and dark matter in the evolution of dwarf galaxies. *MNRAS*, 313:291–309.
- Freyer, T., Hensler, G., and Yorke, H. W. (2003). Massive Stars and the Energy Balance of the Interstellar Medium. I. The Impact of an Isolated 60 M_{Solar} Star. *ApJ*, 594:888–910.
- Freyer, T., Hensler, G., and Yorke, H. W. (2006). Massive Stars and the Energy Balance of the Interstellar Medium. II. The 35 M_{Solar} Star and a Solution to the “Missing Wind Problem”. *ApJ*, 638:262–280.
- Gerritsen, J. P. E. and Icke, V. (1997). Star formation in N-body simulations. I. The impact of the stellar ultraviolet radiation on star formation. *A&A*, 325:972–986.
- Gingold, R. A. and Monaghan, J. J. (1977). Smoothed particle hydrodynamics - Theory and application to non-spherical stars. *MNRAS*, 181:375–389.
- Grebel, E. K. (2001). Star Formation Histories of Nearby Dwarf Galaxies. *Astrophysics and Space Science Supplement*, 277:231–239.
- Gunn, J. E. and Gott, III, J. R. (1972). On the Infall of Matter Into Clusters of Galaxies and Some Effects on Their Evolution. *A&A*, 176:1.

-
- Harfst, S., Theis, C., and Hensler, G. (2006). Modelling galaxies with a 3d multi-phase ISM. *A&A*, 449:509–518.
- Hensler, G. (1987). Galactic Evolution - Some Aspects towards a Consistent Understanding. *Mitteilungen der Astronomischen Gesellschaft Hamburg*, 70:141.
- Hensler, G. (2010). Accretion-regulated Star Formation in Galaxies. In *From Stars to Galaxies: Connecting our Understanding of Star and Galaxy Formation*, page 164.
- Hensler, G. (2011). The Morphological Origin of Dwarf Galaxies. In Koleva, M., Prugniel, P., and Vauglin, I., editors, *EAS Publications Series*, volume 48 of *EAS Publications Series*, pages 383–395.
- Hensler, G. and Rieschick, A. (2002). Star Formation in Dwarf Irregular Galaxies: From Self-regulation to Starbursts (Invited). In Grebel, E. K. and Brandner, W., editors, *Modes of Star Formation and the Origin of Field Populations*, volume 285 of *Astronomical Society of the Pacific Conference Series*, page 341.
- Hensler, G., Theis, C., and Gallagher, III., J. S. (2004). Evolution of dwarf-elliptical galaxies. *A&A*, 426:25–36.
- Hodge, P. W. (1971). Dwarf Galaxies. *ARA&A*, 9:35.
- Hollenbach, D. and McKee, C. F. (1979). Molecule formation and infrared emission in fast interstellar shocks. I Physical processes. *A&AS*, 41:555–592.
- Israelian, G., Ecuivillon, A., Rebolo, R., García-López, R., Bonifacio, P., and Molaro, P. (2004). Galactic evolution of nitrogen. *A&A*, 421:649–658.
- Katz, N. (1992). Dissipational galaxy formation. II - Effects of star formation. *A&A*, 391:502–517.
- Kawata, D. and Hanami, H. (1998). Fragmentation of Collapsing Gas Disks in External Potentials. *PASJ*, 50:547–558.
- Kennicutt, J. R. C. (1998a). The Global Schmidt Law in Star-forming Galaxies. *ApJ*, 498:541–552.
- Kennicutt, Jr., R. C. (1998b). Star Formation in Galaxies Along the Hubble Sequence. *ARA&A*, 36:189–232.
- Koeppen, J., Theis, C., and Hensler, G. (1995). Self-regulated star-formation in chemodynamical models of galaxies. *A&A*, 296:99.

-
- Kormendy, J. and Kennicutt, Jr., R. C. (2004). Secular Evolution and the Formation of Pseudobulges in Disk Galaxies. *ARA&A*, 42:603–683.
- Kroupa, P., Tout, C. A., and Gilmore, G. (1993). The distribution of low-mass stars in the Galactic disc. *MNRAS*, 262:545–587.
- Kudritzki, R. P., Pauldrach, A., and Puls, J. (1987). Radiation driven winds of hot luminous stars. II - Wind models for O-stars in the Magellanic Clouds. *A&A*, 173:293–298.
- Kuehntreiber, M. (2010). Starburst dwarf galaxies.
- Larson, R. B. (1969). The emitted spectrum of a proto-star. *MNRAS*, 145:297.
- Lelli, F., Verheijen, M., and Fraternali, F. (2014). The triggering of starbursts in low-mass galaxies. *MNRAS*, 445:1694–1712.
- Lipovka, A., Núñez-López, R., and Avila-Reese, V. (2005). The cooling function of HD molecule revisited. *MNRAS*, 361:850–854.
- Lisker, T., Brunngräber, R., and Grebel, E. K. (2009). Early-type dwarf galaxies with spiral structure. *Astronomische Nachrichten*, 330:966.
- Lisker, T., Grebel, E. K., and Binggeli, B. (2006). Virgo Cluster Early-Type Dwarf Galaxies with the Sloan Digital Sky Survey. I. On the Possible Disk Nature of Bright Early-Type Dwarfs. *AJ*, 132:497–513.
- Liu, G. R. and Liu, M. B. (2003). *Smoothed ParticleHydrodynamics - a meshfree particle method*. World Scientific Publishing Co. Pte. Ltd.
- Liu, L. (2013). *A Multi-Phase Chemodynamic Galaxy Formation Model*. PhD thesis, Ruperto-Carola-University of Heidelberg.
- Liu, L., Petrov, M., Berczik, P. P., Spurzem, R., and Hensler, G. (2015). A Multi-phase Chemodynamical Particle-based Code of Galaxy Evolution. *A&A*, (submitted).
- Lucy, L. B. (1977). A numerical approach to the testing of the fission hypothesis. *AJ*, 82:1013–1024.
- Mac Low, M.-M. and Ferrara, A. (1999). Starburst-driven Mass Loss from Dwarf Galaxies: Efficiency and Metal Ejection. *ApJ*, 513:142–155.
- Mashchenko, S., Wadsley, J., and Couchman, H. M. P. (2008). Stellar Feedback in Dwarf Galaxy Formation. *Science*, 319:174–.

-
- Mayer, L., Governato, F., Colpi, M., Moore, B., Quinn, T., Wadsley, J., Stadel, J., and Lake, G. (2001). The Metamorphosis of Tidally Stirred Dwarf Galaxies. *A&A*, 559:754–784.
- McQuinn, K. B. W., Lelli, F., Skillman, E. D., Dolphin, A. E., McGaugh, S. S., and Williams, B. F. (2015). The link between mass distribution and starbursts in dwarf galaxies. *ArXiv e-prints*.
- Meurer, G., Bruzzone, S., Lagos, C., Elson, E. C., Werk, J., Blakeslee, J., and Ford, H. (2015). The Initial Mass Function and Star Formation Law in The Outer Disk of NGC2915. In *American Astronomical Society Meeting Abstracts*, volume 225 of *American Astronomical Society Meeting Abstracts*, page 248.01.
- Monaghan, J. J. (1997). SPH and Riemann Solvers. *Journal of Computational Physics*, 136:298–307.
- Moore, B., Katz, N., Lake, G., Dressler, A., and Oemler, A. (1996). Galaxy harassment and the evolution of clusters of galaxies. *NAT*, 379:613–616.
- Murante, G., Monaco, P., Giovalli, M., Borgani, S., and Diaferio, A. (2010). A subresolution multiphase interstellar medium model of star formation and supernova energy feedback. *MNRAS*, 405:1491–1512.
- Nagashima, M., Yahagi, H., Enoki, M., Yoshii, Y., and Gouda, N. (2005). Numerical Galaxy Catalog. I. A Semianalytic Model of Galaxy Formation with N-Body Simulations. *A&A*, 634:26–50.
- Nagashima, M. and Yoshii, Y. (2004). Hierarchical Formation of Galaxies with Dynamical Response to Supernova-Induced Gas Removal. *A&A*, 610:23–44.
- Noguchi, M. (1988). Amorphous galaxies as the end product of tidal interaction. *A&A*, 201:37–43.
- Papaderos, P., Recchi, S., and Hensler, G. (2012). *Dwarf Galaxies: Keys to Galaxy Formation and Evolution*. Springer.
- Ploekinger, S. (2014). *On the Formation and Evolution of Tidal Dwarf Galaxies*. PhD thesis, University of Vienna.
- Price, D. J. (2007). splash: An Interactive Visualisation Tool for Smoothed Particle Hydrodynamics Simulations. *pasa*, 24:159–173.

-
- Raiteri, C. M., Villata, M., and Navarro, J. F. (1996). Simulations of Galactic chemical evolution. I. O and Fe abundances in a simple collapse model. *A&A*, 315:105–115.
- Recchi, S. (2014). Chemodynamical Simulations of Dwarf Galaxy Evolution. *Advances in Astronomy*, 2014:4.
- Recchi, S. and Hensler, G. (2007). The effect of clouds in a galactic wind on the evolution of gas-rich dwarf galaxies. *A&A*, 476:841–852.
- Recchi, S. and Hensler, G. (2013). The fate of heavy elements in dwarf galaxies - the role of mass and geometry. *A&A*, 551:A41.
- Recchi, S., Hensler, G., and Anelli, D. (2009). Galactic outflows and the chemical evolution of dwarf galaxies. *ArXiv e-prints*.
- Recchi, S., Theis, C., Kroupa, P., and Hensler, G. (2007). The early evolution of tidal dwarf galaxies. *A&A*, 470:L5–L8.
- Salpeter, E. E. (1955). The Luminosity Function and Stellar Evolution. *A&A*, 121:161.
- Sawala, T., Scannapieco, C., Maio, U., and White, S. (2010). Formation of isolated dwarf galaxies with feedback. *MNRAS*, 402:1599–1613.
- Scannapieco, C., Tissera, P. B., White, S. D. M., and Springel, V. (2006). Feedback and metal enrichment in cosmological SPH simulations - II. A multiphase model with supernova energy feedback. *MNRAS*, 371:1125–1139.
- Schmidt, M. (1959). The Rate of Star Formation. *ApJ*, 129:243.
- Schombert, J. M., Pildis, R. A., Eder, J. A., and Oemler, J. A. (1995). Dwarf Spirals. *AJ*, 110:2067.
- Schroyen, J., De Rijcke, S., Koleva, M., Cloet-Osselaer, A., and Vandenbroucke, B. (2013). Stellar orbits and the survival of metallicity gradients in simulated dwarf galaxies. *MNRAS*, 434:888–905.
- Schroyen, J., de Rijcke, S., Valcke, S., Cloet-Osselaer, A., and Dejonghe, H. (2011). Simulations of the formation and evolution of isolated dwarf galaxies - II. Angular momentum as a second parameter. *MNRAS*, 416:601–617.
- Semelin, B. and Combes, F. (2002). Formation and evolution of galactic disks with a multiphase numerical model. *A&A*, 388:826–841.

-
- Silk, J., Wyse, R. F. G., and Shields, G. A. (1987). On the origin of dwarf galaxies. *A&AL*, 322:L59–L65.
- Spite, M., Cayrel, R., Plez, B., Hill, V., Spite, F., Depagne, E., François, P., Bonifacio, P., Barbuy, B., Beers, T., Andersen, J., Molaro, P., Nordström, B., and Primas, F. (2005). First stars VI - Abundances of C, N, O, Li, and mixing in extremely metal-poor giants. Galactic evolution of the light elements. *A&A*, 430:655–668.
- Springel, V. (2005). The cosmological simulation code GADGET-2. *MNRAS*, 364:1105–1134.
- Springel, V. (2010). Smoothed Particle Hydrodynamics in Astrophysics. *ARA&A*, 48:391–430.
- Springel, V. (2014). High performance computing and numerical modelling. *ArXiv e-prints*.
- Springel, V. and Hernquist, L. (2003). Cosmological smoothed particle hydrodynamics simulations: a hybrid multiphase model for star formation. *MNRAS*, 339:289–311.
- Springel, V., Yoshida, N., and White, S. D. M. (2001). GADGET: a code for collisionless and gasdynamical cosmological simulations. *NA*, 6:79–117.
- Stinson, G., Seth, A., Katz, N., Wadsley, J., Governato, F., and Quinn, T. (2006). Star formation and feedback in smoothed particle hydrodynamic simulations - I. Isolated galaxies. *MNRAS*, 373:1074–1090.
- Stinson, G. S., Dalcanton, J. J., Quinn, T., Kaufmann, T., and Wadsley, J. (2007). Breathing in Low-Mass Galaxies: A Study of Episodic Star Formation. *A&A*, 667:170–175.
- Tammann, G. A. (1994). *Dwarf Galaxies*. Eur. South. Obs. Astrophys. Symp., 49:3-9.
- Theis, C., Burkert, A., and Hensler, G. (1992). Chemo-dynamical evolution of massive spherical galaxies. *A&A*, 265:465–477.
- Theis, C. and Hensler, G. (1993). Dynamical evolution of dissipative cloud systems. *A&A*, 280:85–104.

-
- Thornton, K., Gaudlitz, M., Janka, H.-T., and Steinmetz, M. (1998). Energy Input and Mass Redistribution by Supernovae in the Interstellar Medium. *A&A*, 500:95–119.
- Valcke, S., de Rijcke, S., and Dejonghe, H. (2008). Simulations of the formation and evolution of isolated dwarf galaxies. *MNRAS*, 389:1111–1126.
- van Zee, L., Haynes, M. P., and Salzer, J. J. (1997). Optical Colors and the Metallicities of Gas-Rich Quiescent Dwarf Galaxies. *AJ*, 114:2479.
- Xu, G. (1995). A New Parallel N-Body Gravity Solver: TPM. *A&AS*, 98:355.
- Yoshii, Y. and Arimoto, N. (1987). Spheroidal systems as a one-parameter family of mass at their birth. *A&A*, 188:13–23.

List of Figures

2.1	Cubic Spline function	17
2.2	Illustration of the smoothing length h	19
3.1	Illustration of the tree construction	25
4.1	Cooling function	33
4.2	Cumulative number of SNe and PNe events	44
4.3	Cumulative feedback mass for stellar wind, SNe and PNe	45
5.1	Cooling tests	48
5.2	Rendered image showing 6 snapshots of the feedback test	50
5.3	Comparison of the feedback tables with the FB-test run (Mass)	51
5.4	Comparison of the feedback tables with the FB-test run (Number of events)	51
5.5	Total feedback energy from the FB-test within the first Gyr	52
5.6	Error between produced FB and received FB by gas particles	53
6.1	Miyamoto-Nagai profile - ρ distribution	56
6.2	Burkert profile - ρ distribution	56
6.3	Displacement of the center of mass	59
6.4	Displacement of the center of mass	60
6.5	Motions of the center of mass during 1 Gyr	60
7.1	Mass evolution of the reference runs	63
7.2	SFRs of the reference runs	64
7.3	Density distributions of the reference runs	65
7.4	Temperature distributions of the reference runs	66
7.5	Phase-space diagrams of the reference runs	67
7.6	Energy evolution of the reference runs	69
7.7	Angular momentum evolution of the reference runs	70

7.8	Rotation curve of the reference runs	70
7.9	Face on view on the modelled dwarf galaxy at 20, 50 and 100 Myr	71
7.10	Edge on view on the simulated dwarf galaxy at 20, 50 and 100 Myr simulation time	71
7.11	Face on view on the simulated dwarf galaxy at 120, 150 and 200 Myr simulation time	72
7.12	Edge on view on the simulated dwarf galaxy at 120, 150 and 200 Myr simulation time	72
7.13	Face on view on the simulated dwarf galaxy at 500, 1000 and 1500 Myr simulation time	73
7.14	Edge on view on the simulated dwarf galaxy at 500, 1000 and 1500 Myr simulation time	73
7.15	Face on view on the simulated dwarf galaxy at 2000, 2500 and 3000 Myr simulation time	74
7.16	Edge on view on the simulated dwarf galaxy at 2000, 2500 and 3000 Myr simulation time	74
7.17	Frequency spectrum of the SFR for the stochastic SF recipe	76
7.18	Frequency spectrum of the SFR for the self-regulated SF recipe	77
7.19	SFRs for 6 starburst regions of the stochastic SF recipe	78
7.20	SFRs for 6 starburst regions of the self-regulated SF recipe	79
7.21	Time evolution of density and temperature for the stochastic SF recipe	81
7.22	Time evolution of density and temperature for the self-regulated SF recipe	82
7.23	Initial starburst of the self-regulated SF recipe	83
7.24	Evolution of the chemical abundances for 9 different elements (stochas- tic SF recipe)	84
7.25	Evolution of the chemical abundances for 9 different elements (self- regulated SF recipe)	85
7.26	Distributions of O and N for the reference simulations	86
7.27	[Fe/H] vs. [O/Fe] and log(N/O) vs. 12+log(O/H) for the reference simulations	87
8.1	SFRs for 4 different cooling shut-off times (stochastic SF recipe)	90
8.2	SFRs for 4 different cooling shut-off times (self-regulated SF recipe)	91
8.3	Mass evolution for different cooling shut-off times (stochastic SF recipe)	93

8.4	Mass evolution for different cooling shut-off times (self-regulated SF recipe)	93
8.5	[Fe/H] vs. [O/Fe] and log(N/O) vs. $12+\log(\text{O}/\text{H})$ for different τ_{CSO} (stochastic SF recipe)	94
8.6	[Fe/H] vs. [O/Fe] and log(N/O) vs. $12+\log(\text{O}/\text{H})$ for different τ_{CSO} (self-regulated SF recipe)	94
9.1	SFR for 4 different gravitational softenings (stochastic SF recipe) .	96
9.2	SFR for 4 different gravitational softenings (self-regulated SF recipe)	97
9.3	Mass evolution for different gravitational softenings (stochastic SF recipe)	99
9.4	Mass evolution for different gravitational softenings (self-regulated SF recipe)	100
9.5	[Fe/H] vs. [O/Fe] and log(N/O) vs. $12+\log(\text{O}/\text{H})$ for different ϵ (stochastic SF recipe)	100
9.6	[Fe/H] vs. [O/Fe] and log(N/O) vs. $12+\log(\text{O}/\text{H})$ for different ϵ (self-regulated SF recipe)	101
10.1	SFRs for 3 different SN efficiencies (stochastic SF recipe)	104
10.2	SFRs for 3 different SN efficiencies (self-regulated SF recipe) . . .	105
10.3	Mass evolution for different SN efficiencies (stochastic SF recipe) .	106
10.4	Mass evolution for different SN efficiencies (self-regulated SF recipe)	106
10.5	[Fe/H] vs. [O/Fe] and log(N/O) vs. $12+\log(\text{O}/\text{H})$ for different SN_{eff} (stochastic SF recipe)	107
10.6	[Fe/H] vs. [O/Fe] and log(N/O) vs. $12+\log(\text{O}/\text{H})$ for different SN_{eff} (self-regulated SF recipe)	107
11.1	SFRs - comparison with the multi-phase model	112
11.2	Energy evolution - comparison with the multi-phase model	113
11.3	Mass evolution - comparison with the multi-phase model	114
11.4	O abundances - comparison with the multi-phase model	115
11.5	[Fe/H] vs. [O/Fe] - comparison with the multi-phase model	116
11.6	log(N/O) vs. $12+\log(\text{O}/\text{H})$ - comparison with the multi-phase model	117
12.1	Average SFR between the first 0.5 and 3 Gyr as a function of the cooling shut-off time. Orange inverted triangles show results of the stochastic SF recipe and turquoise triangles for the self-regulated recipe.	120
12.2	Same as fig. 12.1, but for the average SFR as a function of the gravitational softening.	121

12.3 Same as fig. 12.2, but for the average SFR as a function of the SN efficiency. 122

List of Tables

5.1	Calculated cooling times τ_c for different metallicities and gas densities. . .	49
6.1	Summary of the initial conditions	57
6.2	Parameter settings for the low- and high-accuracy simulation . . .	59
7.1	Calculated models and their most important specific simulation parameters.	62
7.2	specifications of 6 different starburst regions (stochastic SF recipe)	80
7.3	specifications of 6 different starburst regions (SF recipe)	80
8.1	Comparisons of runs with different τ_{CSO}	92
9.1	Comparisons of runs with different ϵ	98
10.1	Comparisons of runs with different SN_{eff}	105
11.1	Initial conditions of the multi- and single-phase simulation	110

Curriculum Vitæ

Matthias Kühtreiber, Bakk. rer. nat.

E-Mail Address: a0749244@unet.univie.ac.at

Education and Studies

- 2012 - 2015 Academic study of Astronomy at the University of Vienna
(Master of Science)
Thesis title: "The Chemo-Dynamical Evolution of Dwarf-Galaxy Discs"
Supervisor: Univ.-Prof. Dipl.-Phys. Dr. Gerhard Hensler
- 2008 - 2012 Academic study of Astronomy at the University of Vienna
(Bakk. rer. nat.)
Thesis title: "Starburst Dwarf Galaxies"
Supervisor: Univ.-Prof. Dipl.-Phys. Dr. Gerhard Hensler
- 1999 - 2007 Grammar school Bundesrealgymnasium Waidhofen/Thaya
Compartment work: "Der Dopplereffekt in der Astronomie"

Scientific Work

Workshop "Extraterrestrial Life - Beyond our Expectations":
Collaboration at the local organizing committee May 21st -
22nd 2012

Collaboration at the Shanghai Astronomical Observatory
(SHAO) with Prof. Lin Weipeng from September 21st - 30th
2013. Financed by the ÖAD (Austrian agency for interna-
tional mobility and cooperation in education, science and
research).

Participation at the European Week of Astronomy and Space

Science (EWASS2015) in Tenerife with oral presentation,
from June 22nd - 26th 2015

Vienna, July 16, 2015

Would you like to see videos of the reference simulations?



run "sto01" face on



run "sto01" edge on



run "sr01" face on



run "sr01" edge on

Simply scan the QR codes above with your mobile device. Or visit the author's youtube channel:

<https://www.youtube.com/channel/UC-5jFo7dTONxtQr2uDqgM6Q>